UNIVERSITY
OF OSLO

Master's thesis

Searching for stellar emission in the sub-THz bands

Mats Kirkaune

60 ECTS study points

Institute of Theoretical Astrophysics
Faculty of Mathematics and Natural Sciences

Spring 2023

Mats Kirkaune

Searching for stellar emission in the sub-THz bands

Supervisors:
Sven Wedemeyer
Atul Mohan

Abstract

Detecting radio emission from stars has received increasing attention, be it for better understanding the structure and dynamics of our own Sun's outer atmosphere or in the search for life on habitable extrasolar planets. There have been many targeted studies of radio emission from red M-type dwarf stars, as many exoplanets have been discovered orbiting them, while larger and hotter stars have often been completely neglected in radio studies. The aim of this study is therefore to search for stellar emission in several radio surveys, thereby ridding us of the common bias towards M dwarf stars and known flare stars. Finding evidence of quiescent and flaring radio emission from hotter, and larger stars of spectral type G, F or A could lead to important insight into the activity and structure of the outer atmospheres of these stars. We here search archival observations from the six radio surveys GLEAM, LoTSS, TGSS, RACS, VLA FIRST and VLASS, with frequencies spanning from 72 MHz to 4 GHz, for stellar emission associated with known stars as registered in the Gaia DR3 stellar catalogue. The detected stars are filtered into fitting categories based on their position in the Hertzsprung-Russel diagram and their SIMBAD object types with single main sequence stars being the main focus of this project. Our search for stellar emission has lead to many radio detections of single main sequence stars across all surveys except GLEAM. Many of the detections are not found to be previously reported. By relating the measured brightness temperature and/or radio luminosity to different stellar parameters and activity indicators, we find very similar relations across frequencies from 144 MHz to 3 GHz. The catalogues of detected stars in each of the surveys are very valuable as a basis for future observation time proposals, for which the measured fluxes and positions could be utilised. We also present many outlier stars, that show unusually high radio luminosities compared to similar stars, many of which would be interesting targets for future observations.

Acknowledgments

First and foremost, I want to thank my supervisor and co-supervisor Sven Wedemeyer and Atul Mohan. Thank you for your patience, your guidance and for giving invaluable input on my work. I have learnt a lot during our meetings. Thank you for including me in the excellent research environment at ITA, RoCS and the solar/stellar group. I have learnt a lot during the meetings in the solar/stellar group, and being allowed to be a part of a serious research environment has motivated my greatly in my work.

I also want to extend my gratitude to my family, to my parents and sister for their endless support during these years, and for helping me move to Oslo to pursue a degree in astronomy. I also want to thank my grandmothers for their support during these years, and for showing interest in my work. Additionally, I want to thank my grandfathers for sparking my interest in the natural sciences, none of which got to see me finish this thesis. Finally, I want to thank my maternal grandfather for the daily conversations during these years, your encouragement and curiosity.

This work has made use of data from the European Space Agency (ESA) mission *Gaia* (https://www.cosmos.esa.int/gaia), processed by the *Gaia* Data Processing and Analysis Consortium (DPAC, https://www.cosmos.esa.int/web/gaia/dpac/consortium). Funding for the DPAC has been provided by national institutions, in particular the institutions participating in the *Gaia* Multilateral Agreement.

LOFAR data products were provided by the LOFAR Surveys Key Science project (LSKSP; https://lofar-surveys.org/) and were derived from observations with the International LOFAR Telescope (ILT). LOFAR (van Haarlem et al. 2013) is the Low Frequency Array designed and constructed by ASTRON. It has observing, data processing, and data storage facilities in several countries, which are owned by various parties (each with their own funding sources), and which are collectively operated by the ILT foundation under a joint scientific policy. The efforts of the LSKSP have benefited from funding from the European Research Council, NOVA, NWO, CNRS-INSU, the SURF Co-operative, the UK Science and Technology Funding Council and the Jülich Supercomputing Centre.

This research has made use of the CIRADA cutout service at cutouts.cirada.ca, operated by the Canadian Initiative for Radio Astronomy Data Analysis (CIRADA). CIRADA is funded by a grant from the Canada Foundation for Innovation 2017

Innovation Fund (Project 35999), as well as by the Provinces of Ontario, British Columbia, Alberta, Manitoba and Quebec, in collaboration with the National Research Council of Canada, the US National Radio Astronomy Observatory and Australia's Commonwealth Scientific and Industrial Research Organisation.

Contents

List of Figures

Chapter 1

Introduction

Electromagnetic waves are the source of almost everything we know about our universe, our galaxy and the billions of stars within it. Historically, everything from the spatial distribution of stars, their motion through space to their chemical compositions we have owed to the electromagnetic radiation we receive and are able to detect from these distant objects, more recently also supplemented by gravitational wave and neutrino astronomy. The electromagnetic radiation we receive from stars can span the entire electromagnetic spectrum, although different frequencies have been found to probe different heights in stellar atmospheres as well as originate in different physical phenomena attributed to stellar activity. Stellar activity is a collective term for the different variability phenomena in the upper atmospheres of stars, all understood to originate in the structured magnetic fields emerging from their upper convective zones (Pagano 2013). The moving plasma in a stellar atmosphere shuffle and twist the emerging magnetic flux tubes, creating highly complex and energetic magnetic structures. To reach a lower energy state the magnetic field lines reconfigure into more stable configurations, releasing energy into the ambient plasma across atmospheric layers, often observed as flares across the electromagnetic spectrum. This release of energy is understood to drive most of the variability phenomena encompassed by the stellar activity term, and it is because of this that stellar activity has been so closely linked to dwarf stars with sufficiently deep surface convection zones (spectral type F5 and later, see Pedersen et al. 2016).

The atmospheres of dwarf stars on the main sequence are generally divided into three layers, although these layers should not be seen as static layers, but rather as dynamically coupled domains (Wedemeyer-Böhm et al. 2009). The lowest and coldest of the layers is the photosphere, stretching from the stellar "surface" upwards till the temperature starts to increase again. The second and slightly hotter layer is called the chromosphere, which stretches up to the so-called transition region which marks the dramatic temperature increase to the millions of degrees Kelvin in the corona – the outermost layer of the Sun. The causes of the dramatic increase in temperature in the transition region is not yet fully understood, and is one of the most actively researched subjects in solar physics (Aschwanden 2005). The corona, is the hottest atmospheric layer by far, the solar corona having temperatures one the order of a million Kelvin. The corona is also the source of much of the radio waves we observe in the Sun or other stars. This emission is often found to be too bright to be explained by thermal processes, therefore being non-thermal in nature. Plasma emission and gyromagnetic emission are two mechanisms for non-thermal radio emission in the Sun. The idea behind plasma emission is that energy release events in the corona accelerate beams of electrons which trigger a two-stream instability in the ambient plasma, thus generating coherent plasma emission through resonant wave-particle and wave-wave interactions at the local plasma frequency and its harmonics (Melrose 2009). This theory was first described by Ginzburg & Zhelezniakov (1958). That the emission is coherent means that all particles are emitting in-phase under a resonance interaction leading to an intense radiation, similar to a free-electron maser scenario. Plasma emission happens at the local plasma frequency ω_p or its harmonic, which is a function of height in the atmosphere. In the lower corona, the local plasma frequency is in the sub-THz range and corresponds to wavelengths on the order of centimetres to metres, briefly referred to as the radio regime. This makes radio observations a very convenient way to detect and explore the cross coronal evolution of even weak particle acceleration events, often undetectable in other wavebands.

Due to their high sensitivity towards accelerated particle/flaring activity, radio surveys have become very important in the study of stellar activity, which has turned out to be very important in the search of exoplanets that could sustain life. Radio monitoring could also be utilised in the search of exoplanets, as Vedantham et al. (2020) has shown periodic radio emission from the star GJ 1151 coinciding with the theorised orbital period of an orbiting satellite. The interaction between an orbiting close-in planet and the stellar magnetic field often produces periodic intense coherent radio emission at the rotation period of the planet, similar to the observed Jovian radio bursts triggered by Io. A recent study of the YZ CMi system claim to detect Auroral radio emission from the close-in planet, and using theoretical models they computed a magnetic field for the planet (Trigilio et al. 2023). In this search for exoplanets that could sustain life, M-dwarfs have been the prime targets because of their relatively long lifetimes, their number and the sheer number of exoplanets that have already been detected orbiting M dwarfs (Bashi et al. 2020; Childs et al. 2022). However, the heightened stellar activity observed for M dwarfs, could be very problematic in the formation of life on any Earth-like planet, as violent winds, frequent stellar storms and superflares might hinder a planet from having an atmosphere that could sustain life as we know it (e.g. Lammer et al. 2007; Zendejas et al. 2010; Vidotto et al. 2013). The high activity of M-dwarfs has made them attractive to numerous targeted radio band studies, while other stellar types have been neglected in comparison. Studies based on large volumes of data from surveys like Kepler, Gaia etc., have shown that the cool stars, primarily spectral types F - M, collectively host a large number of exoplanets in their habitable zones (Bashi et al. 2020, e.g.), making cool stellar types other than M-dwarfs also interesting candidates to explore activity. Hence, we wish to perform a blind search for stellar emission across a wide variety of radio surveys spanning the frequency range from MHz to GHz to identify active stars in the nearby radio detectable sky volume.

The sensitivities of sub-THz surveys are usually insufficient for quiescent flux detection from stars, but the flaring fluxes of nearby stars have been found to be 2-6 orders of magnitude higher than the quiescent flux, owing to their non-thermal/coherent emission nature, suddenly making sub-THz detections possible. As sub-THz surveys are only able to detect flaring stars, these surveys are blind and unbiased all sky searches for flare stars, as opposed to the more common targeted studies which are often biased towards X-ray, UV bright or known flaring nearby stars. This blind and unbiased search for flaring stars in sub-THz surveys also rids us of the common bias towards M dwarfs in targeted studies, allowing us to better understand if other stellar types also produce bright sub-THz flares. Our goal was therefore to find evidence of stellar emission at mm/radio wavelengths in publicly available archival observations, that have not yet been reported, not only focusing on the commonly targeted M dwarfs, but also looking for emission from K-, G-, F- and A dwarfs to provide important insights into the properties and activity of the outer atmospheres of stars for a large range of different stellar types. Though we focused on single, main sequence stars, the method developed to search across archival observations for stellar emission has been shown to work for every stellar class and for associations of stars. Secondary samples of detected stars/stellar associations as by-products of our search are also presented but not analysed further. To achieve our goal we have searched archival observations for stellar emission from six surveys, ranging from the Galactic and Extra-Galactic All-Sky MWA survey (GLEAM), its lowest achievable frequency being 72 MHz (4 m), to the VLA Sky Survey (VLASS) with its highest achievable frequency being 4 GHz (75 mm). However, no clear evidence of stellar emission was found in the GLEAM survey, although several detections were found in each of the remaining surveys, yielding a great sample of detected stars from the LOFAR Two-metre Sky Survey's (LoTSS) 144 MHz to VLASS' mean frequency of 3 GHz that we were able to use to give better insights into their activity. We report several stars not previously reported in the considered surveys, some of which are promising targets for future radio observations.

In Chapter 2 we present this projects' theoretical background, going over topics ranging from the fundamental structures of stars to the different phenomena thought to produce the observed radio emission in stars. Chapter 3 introduces the data in greater detail, as well as describing the various methods and scripts we have either utilised from other groups or developed ourselves. In Chapter 4 the results of our project are presented on a per-survey basis, before more general cross-survey results are presented. In Chapter 5 we discuss our results, their implications and how one could use them in further studies. Finally, in Chapter 6 we present the final conclusions of this project.

Chapter 2

Theory

2.1 Stellar Classification

The first recorded case of classifying stars according to their magnitudes was performed by the Greek astronomer Hipparchos in the second century BC. Hipparchos classified stars according to how bright they appeared to the naked eye, and assigned them a class of 1 to 6, the 1st class being the brightest and the 6th the dimmest (Ptolemy & Toomer 1984). Today, stars are classified using a modified version of the Harvard spectral classification scheme, developed at the end of the 19th century at the Harvard college observatory. Originally stars were assigned to a type A to Q based on the strength of the hydrogen lines in their spectra (Cannon & Pickering 1912). This system was modified in the 20th century to assign stars to types O, B, A, F, G, K and M according to the stars' effective temperatures, O types being the hottest and M types the coolest. In addition, each of the stellar types are divided into numerical sub-divisions from 0 to 9, with 0 being the hottest and 9 the coolest. The stellar type and the sub-class makes up what is often called the star's spectral class.

Spectral types alone are not sufficient to completely encapsulate stellar characteristics, since stars with very similar effective temperature can have vastly different luminosities. The Morgan-Keene luminosity classification scheme was introduced to correct for this flaw. The scheme originally designated a luminosity class to each star, from the roman numeral I for supergiant stars to V for main sequence stars. Today, the supergiant class is usually sub-divided further, and two new luminosity classes have been appended to the scheme, VI for sub-dwarfs and D for white dwarf stars. This luminosity class is appended to a star's spectral class to better describe the star and its features. For example, the Sun is a main sequence star with the spectral class G2, meaning its full stellar class is G2V.

2.2 The Hertzsprung-Russell Diagram

The Hertzsprung-Russel diagram, also abbreviated as the HR diagram, is an inherently useful way of showing the relationship between stars' absolute magnitudes or luminosities and their stellar types or effective temperatures. The diagram was independently developed by the Danish and American astronomers Ejnar Hertzsprung and Henry Norris Russel at the start of the 20th century. An HR diagram showing 22,000 stars from the Hipparcos catalogue (Perryman et al. 1997) is shown in Fig. 2.1, revealing the peculiar relationship discovered between stars' luminosities and effective temperatures. The continuous band of stars found to span almost the entire HR

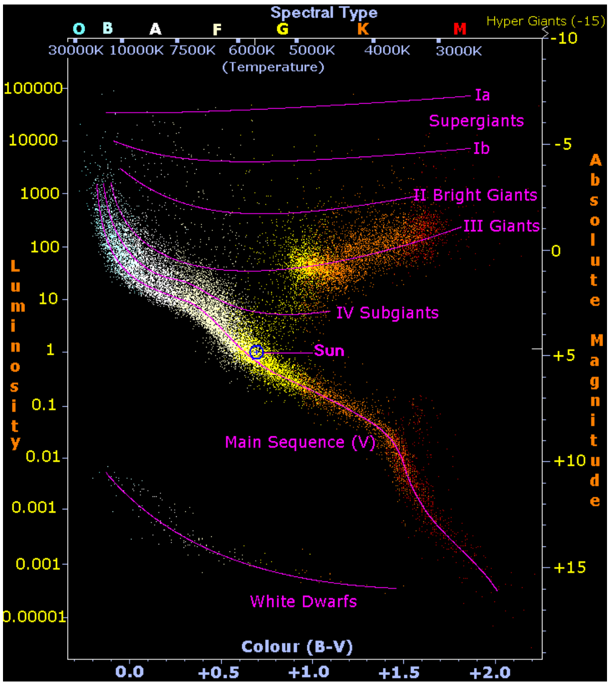

Figure 2.1: Hertzsprung-Russel diagram created by Richard Powell containing 20,000 stars from the Hipparcos catalogue (Perryman et al. 1997). Purple lines are used to indicate the different luminosity classes' positions in the HR diagram. Licensed under CC-BY-SA-2.5

diagram is the main sequence, containing stars at the stage in their lives where their energy generation is dominated by the fusion of hydrogen into helium in their cores. As stated in Sect. 2.1, the main sequence is defined as luminosity class V. A star's position on the main sequence is determined by the star's properties, such as its mass, radius, effective temperature, age and composition. As effective temperature is usually used as the x-axis of the HR-diagram, and most commonly running from right to left, the cooler stars are found at the right-most side of the HR-diagram. Higher temperature stars are therefore found towards the middle and left-hand side of the HR-diagram. The HR diagram is also an effective tool for distinguishing giant stars from dwarf stars, as giants are found to lie on the so-called giant branches which are represented by the purple lines showing the luminosity classes from IV to I in Fig. 2.1. White dwarf stars are also easy to discern in the HR diagram because of their position low in the HR diagram, a consequence of their low luminosity having exhausted their nuclear fuel. White dwarfs are stellar cores, and remnants of stars that have through of their outer layers. As they have exhausted their nuclear fuel, they are initially hot and cools slowly over time. Their position is also shown as a purple line, but not indicated as luminosity class VII, as this is not common practice. The last luminosity class, sub-dwarfs is not immediately obvious in Fig. 2.1, and also not shown as a purple line, caused by their rarity and the difficulty of discerning them from the lower part of the main sequence.

2.3 Stellar atmospheres

Roughly, one can divide the structure of any main sequence star into the stellar interior and the stellar atmosphere. The structure of the stellar interior varies widely by stellar type, the only common factor being the presence of a core where the thermonuclear

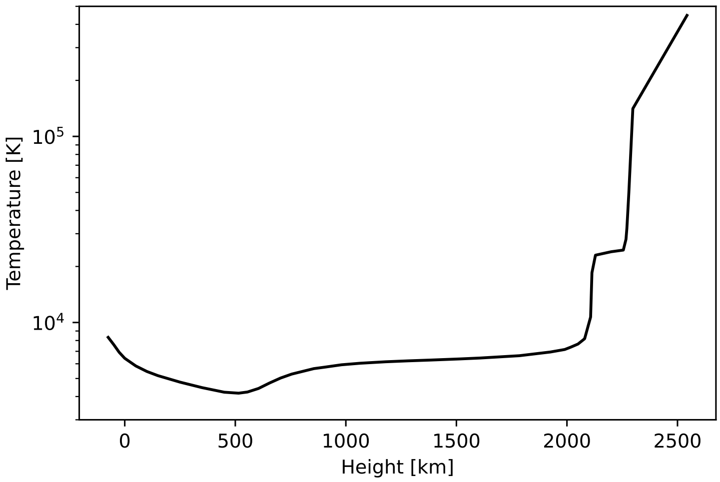

Figure 2.2: Temperature as a function of height in the solar atmosphere model VAL C, which was created by Vernazza et al. (1981).

fusion happens. The core is where the fusion of hydrogen into helium happens for stars on the main sequence. Outside of the core one can have one large convective zone that stretches up to the stellar surface, which is the case for cool, fully convective stars. One could also have an inner radiative zone, where the most efficient method of energy transport is radiation, with an additional outer convective zone, which is the case for the Sun and Sun-like stars. Finally, one could have an inner convective zone and an outer radiative zone, which is the case for more massive main sequence stars than the Sun.

Stellar atmospheres are also generally divided into three possible parts, namely the photosphere, chromosphere and corona, although not all stars show signs of having all three layers. The photosphere is the innermost layer, and is both the coolest and most dense atmospheric layer, in the Sun having a temperature around 5770 K. As the visible light originates in the photosphere, it is therefore this layer that we see when observing the Sun in optical wavelengths/frequencies. As one moves outwards in the photosphere the temperature increases as one approaches the second layer of the atmosphere, the chromosphere (see Fig. 2.2). Although hotter, the chromosphere is much less dense, and not visible in optical wavelengths other than as a thin red layer during solar eclipses. Moving outwards from the chromosphere one encounters the transition region, being the boundary between the chromosphere and the corona. In the Sun the transition region is a $\sim$ 100 km thick layer where the temperature increases dramatically from tens of thousands of degrees to millions. This sudden increase in temperature, making the corona unfathomably hot is not yet fully understood, and is currently one of the most actively researched problems in Solar physics (see Aschwanden 2005, for an overview). The average temperature as a function of height in the solar atmosphere is shown in Fig. 2.2, clearly exhibiting a drastic increase in the transition region. Images of the solar photosphere, chromosphere and corona are presented in Fig. 2.3.

Vaiana et al. (1981) showed that main sequence stars (see Section 2.2) of type M, K, G and F all have chromospheres, and that most of them have coronae, meaning that activity phenomena attributed to either the chromosphere or corona could be present on these types of stars. However, some stars of type A are thought to not have outer

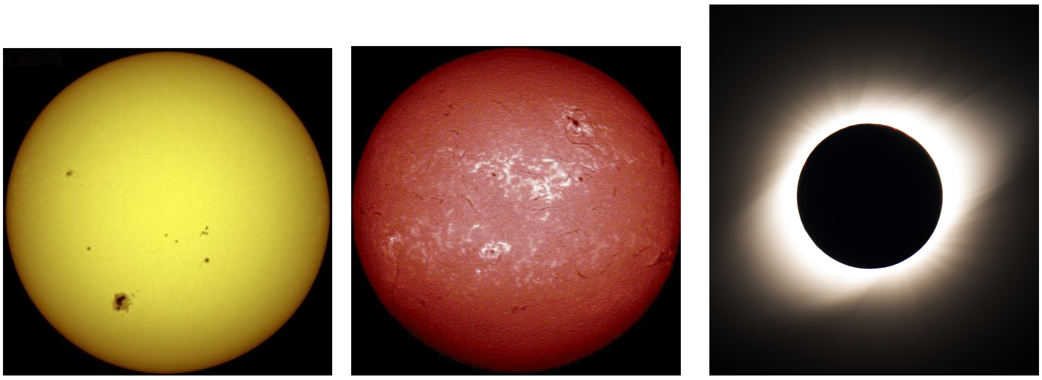

Figure 2.3: Left: The solar photosphere, also called its surface. This layer emits the most visible light, and is therefore what we would see from Earth with our eyes. This image is part of the public domain because it was created by NASA (http://solarscience.msfc.nasa.gov/surface.shtml)
Middle: The solar chromosphere as seen in H-alpha light. The chromosphere is the atmospheric layer above the photosphere. This image is part of the public domain because it was created by NASA (http://solarscience.msfc.nasa.gov/surface.shtml)
Right: The solar corona as seen during a total solar eclipse in Chile in 2019. Because of the relative dimness of the corona in visible light compared to the other atmospheric layers it is only observable in visible light during solar eclipses, where most of the light from the Sun itself is blocked by the Moon. The photo is taken by Luis Rojas and licensed under CC-BY-SA-4.0.

convective layers, and are not observed to emit at UV and X-ray wavelengths, and are therefore thought to not have either chromospheres or coronae. This is due to the importance of a surface convection zone on the global dynamo, as the convective motion in the outer parts of a star is thought to be essential in magnetic field generation. This means that the absence of a surface convective zone also results in an absence of an active atmosphere, thus no chromospheres or coronae are formed. However, some A type stars have been found to support both chromospheres and coronae, leading to the hypothesis that some lower temperature fraction of A types can support other atmospheres, while the hotter fraction cannot (Švanda & Karlický 2016). Studying radio emission from A type stars might help to constrain the effective temperatures beyond which main sequence stars tend to not exhibit a chromosphere and corona.

2.4 Stellar Activity

Stellar activity is a collective term referring to all phenomena in stellar atmospheres that either lead to variability of the emitted radiation or heating of the outer atmospheres, mainly due to the highly structured magnetic fields emerging from their convective zones (Pagano 2013). As the Sun is the only star whose magnetic activity phenomena can be observed and studied in great detail, it has become customary to describe stellar activity through the solar-stellar connection, meaning that activity observed in stellar atmospheres is related to similar phenomena observed in the Sun. Pagano (2013) state that this approach is very successful, both as a way of highlighting the real analogies in the Sun, but also highlighting the differences, being the cases where the observed stellar activity has no counterpart in the solar case.

Because of the close connection between stellar activity and surface convection, mostly stars thought to possess surface convection zones have been found to host phenomena associated with stellar activity. Only cool main sequence stars with temperatures in the range $\sim 3000 - 8000\,K$ are known to have outer convection zones, as stars have been found to lose their outer convection zone in favour of an outer radiative zone if they have effective temperatures above 8250 K, which correlates to masses above $M > 1.5M_{\odot}$ (Simon et al. 2002). According to Pagano (2013) stellar activity is produced by a physical mechanism known as a dynamo, related to the coexistence of a convective zone under the stellar surface and a differential rotation regime. Parker (1977) showed that the coupling between the Sun's turbulent convection and its differential rotation regime leads to an intensification of the magnetic field, but also a period inversion. This period inversion is now known as the 11-year solar cycle, in which the Sun goes from a quiet state to a more active state, before returning to a quiet state, although with an inverted magnetic field.

Pagano (2013) state that the dynamo in the Sun and other stars generates magnetic flux tubes that rise through the convective zone before breaking the stellar surface. These magnetic flux tubes carry hot plasma along to the surface because of the plasma being a charged fluid, therefore following the magnetic field. The rising magnetic flux tubes become braided and twisted by the velocity fields in the stellar atmosphere, and this twisting sometimes leads to cases where the magnetic fields reconnect to reach a lower energy state, thus releasing magnetic free energy. This release of magnetic energy is the main driver of a variety of activity phenomena ranging from weak nanoflares ($\sim 10^{23}$ erg) to strong flares ($\sim 10^{32}$ erg) that can even drive large scale eruptions like the coronal mass ejections (CMEs) (Aschwanden et al. 2000).

2.4.1 Radio Emission from Stellar Coronae

Pagano (2013) state that all magnetically active stars show evidence of both quiescent and flaring radio emission, where the quiescent flux has been found to have brightness temperatures $10^8 - 10^{10}K$, several orders of magnitude hotter than the coronal temperatures usually measured in X-rays. This is because of the quiescent radio emission being non-thermal, meaning that it does not originate in thermal processes, and therefore speaking of temperatures becomes a bit counter-intuitive. The quiescent, non-thermal radio emission has its origins in gyrosynchrotron radiation, a phenomena nearly identical to synchrotron radiation, with the exception being that the electrons are mildly relativistic in gyrosynchrotron radiation. In the creation of gyrosynchrotron radiation mildly relativistic electrons follow spiralling trajectories along the stellar magnetic field. The resulting spectrum depends on the local electron velocity distribution function and magnetic field orientation with respect to the line of sight (Dulk & Marsh 1982; Rybicki & Lightman 1986). The emission peaks within a few multiples of the gyrofrequency,

$$\omega_g = \frac{|e|B}{mc}, \tag{2.1}$$

in cgs units. $|e|$ is here the absolute value of the electron charge, B is the magnetic field strength, m is the electron mass and c is the speed of light (PECSELI 2021). Inserting the values of the electron charge, mass and the speed of light yields that $\omega_g \sim [3 \times B_{Gauss}]\,MHz$, where B_{Gauss} is the magnetic field in Gauss. Meanwhile, in F-K dwarfs quiescent thermal bremsstrahlung is expected at $\sim 10^6$ K, in metrewavebands

(<300 MHz) based on solar observations. This is because the gyrosynchrotron emission contribution drops off even in active regions for these wavelengths. However, the expected thermal flux in metrewavebands for even the nearest star assuming a 1 MK corona is below the detection threshold of existing large surveys.

In addition to quiescent emission, flaring emission has also been detected in the radio regime, closely associated with energy being released in the stellar atmosphere. These energy release events in the corona can accelerate beams of electrons which trigger a two-stream instability in the ambient plasma, thus generating coherent plasma emission through resonant wave-particle and wave-wave interactions at the local plasma frequency and its harmonics (Melrose 2009). This coherent emission is usually observed in metre-wavebands.

White (2007) state that solar radio bursts were some of the first phenomena identified in radio astronomy. These bursts at frequencies below a few hundred MHz were classified into five types by Wild et al. (1963), type I to V. White (2007) state that Type I bursts are non-flare-related phenomena with both a continuum and burst component. They state that their continuum components typically cover the frequency range 100-400 MHz with variations on hour timescales. They state that due to the long duration of this emission it is believed that it is due to trapped energetic electrons in closed coronal magnetic field lines. White (2007) explain that the burst component of Type I bursts are on second timescales, and usually occur on drifting chains of 10-20 MHz bandwidth. Contrary to Type I bursts, Type II bursts are associated with solar flares, and White (2007) state that Type II bursts typically occur at around the time of the soft X-ray peak in a solar flare. It is also stated that Type II bursts are identified by a slow drift to lower frequencies with time in dynamic spectra. White (2007) state that the emission mechanism behind Type II bursts is assumed to be plasma emission at the plasma frequency and its harmonic. It is stated in White (2007) that Type III bursts are brief radio bursts that have a characteristically rapid drift in frequency versus time. They state that Type III bursts are commonly seen in the impulsive phases of solar flares, making them important in understanding field line connectivity. The associated emission mechanism is at the plasma frequency and its harmonic, and the bursts persist on minute to tens of minutes timescales. White (2007) state that Type IV bursts are broadband quasi-continuum features that are associated with the decay phase of solar flares. Their emission is attributed to electrons trapped in closed magnetic field lines in the post-flare loops (or arcades) produced by solar flares. The last of the types of metre-wavelength radio bursts are Type V bursts, which White (2007) state is a relatively rare phenomenon. They state that Type V bursts are closely associated with Type III bursts, as the defining characteristic of Type V bursts is that it is an extended phase following Type III bursts at low frequencies. These extended phases can last up to a minute.

In the GHz bands, the observed radiation usually has one of three origins. Gyrosynchrotron emission is emission from flare accelerated particles trapped in flaring loops (Dulk & Marsh 1982), where the particles gyrate around the magnetic field lines. Gyroresonance emission is very similar to gyrosynchrotron, but the particles' energies are here lower. Finally we have the electron maser emission, caused by an instability in the electron velocity distribution inside a post-flare magnetic flux tube leading to wave-particle resonance interaction at the local plasma frequency, ω_B, and its harmonics. This produces highly polarised and intense coherent radiation (Melrose & Dulk 1982).

Typical magnetic fields on stellar coronae in active regions have strengths in the range ∼ 10 - 1000 G, meaning that the plasma frequency here can range from ∼3 MHz to ∼300 GHz.

2.5 The Radio Window

The Earth's atmosphere, being the layer of gases retained by the gravitational field of the Earth creates a lot of problems when it comes to performing observations in many frequency bands from the Earth's surface. The atmosphere mostly consisting of nitrogen, oxygen and argon, but also a plethora of other less common gases as well as water vapour, absorbs much of the incoming radiation from distant sources. However, the degree of absorption is strongly frequency dependent, stemming from the various energy states of the particles making up the Earth's atmosphere. It has been found that the atmosphere is more or less completely transparent in two frequency bands. The first of these bands is the so-called optical window, the existence of which is the only reason we are able to see the stars in the night sky with our eyes (Dwivedi 2017). However, more importantly the atmosphere is completely transparent to a relatively large range of radio frequencies. The radio window extends from the lower frequency limit of 15 MHz to the high frequency cut-off at approximately 1.5 THz (Wilson et al. 2009). The low frequency cut off mainly comes from plasma frequency cut off of the ionosphere. The opacity of the Earth's atmosphere as a function of frequency is shown in Fig. 2.4, clearly showing the two previously discussed "windows", the optical window indicated by a vertical optical spectrum, and the radio window indicated by a radio telescope dish. The basics of radio telescopes is covered in section 2.6.

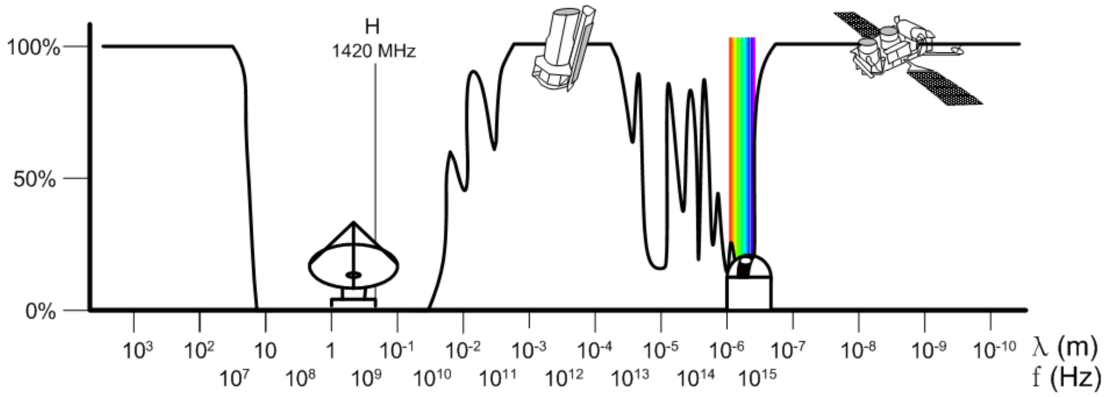

Figure 2.4: Opacity of Earth's atmosphere by Haade, licensed under GFDL. The optical window is here indicated by a vertical optical spectrum from a classical, optical observatory, while the radio window is indicated by a single dish radio telescope.

2.6 Radio Telescopes

Radio telescopes are as the name suggests telescopes that operate in radio frequencies, as these frequencies are easily observable from the Earth's surface because of the radio window as described in Section 2.5. Radio telescopes are usually large dish-type antennas, usually called reflectors. Instead of focusing the light to a point using a lens, a usually parabolically shaped dish or antenna is used to focus the radiation to a focal point (Léna et al. 2012).

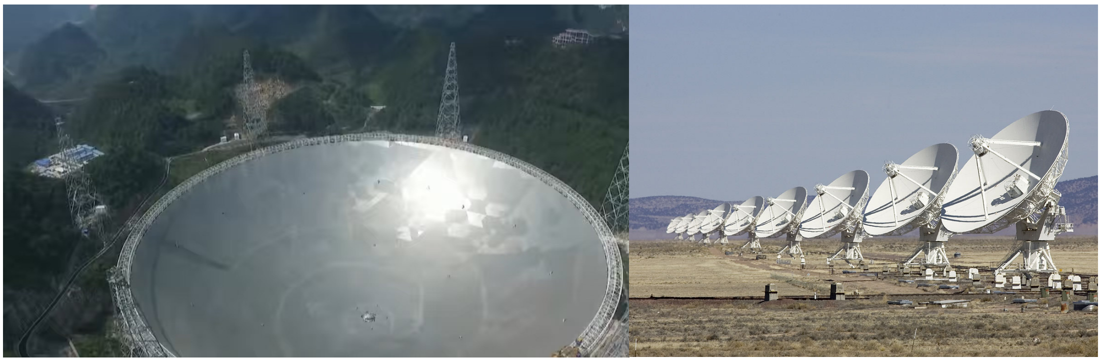

Figure 2.5: Left: Image of the Five Hundred Aperture Spherical Radio Telescope (FAST) in Pingtang in the People's Republic of China. Licensed under CC-BY-3.0. Right: Nine of the 27 dishes making up the Karl G. Jansky Very Large Array in New Mexico, USA. Picture is taken by Tom O'Neil and licensed under CC-BY-SA-4.0.

Due to the relatively long wavelengths of radio waves compared to visible light, for the same aperture as an optical telescope, which is equivalently the diameter of the radio dish, we would have much a poorer angular resolution in the radio case. The diffraction limit defines the theoretical maximum resolving power of the telescope, which is the angular scale of the Airy disk pattern obtained when a monochromatic plane wave passes through a circular aperture (Airy 1835). The diffraction limit thus determines the lowest detectable separation between two point sources in the sky before their Airy disks merge and become indistinguishable. Based on this principle, the Rayleigh criterion states that two point sources are just resolvable with a telescope with an aperture of D (in units of wavelengths) at a wavelength of λ if they are separated by the angle θ (Urone & Hinrichs 2012):

$$\theta = 1.22\frac{\lambda}{D}. \tag{2.2}$$

As modern optical telescopes can reach angular resolutions less than 0.1", we compare the required aperture of a radio telescope with the angular resolution of 0.1" observing at the radio frequency of 3 GHz. For an optical wavelength $\sim 5 \times 10^{-5}$ cm range this is achievable with a $\sim$ 1 m class telescope, while at 3 GHz (λ ~10 cm), the aperture size required is about 21 km - practically impossible to construct and rotate to point at sources of interest.

Optical telescopes very rarely reach their diffraction limits because of the degradation of the image because of turbulence in the atmosphere and other atmospheric effects. In the radio regime some of these atmospheric effects are negligible, but we are still affected by refraction, which various calibration techniques are used to solve. Because of this the diffraction limit is often reached in the radio regime, and the aperture of the telescope then becomes the only factor deciding the maximum angular resolution of our radio image.

The current largest single dish radio telescope is the the Five-Hundred Aperture Spherical Radio Telescope (FAST) with an aperture of 500 metres (Nan et al. 2011) pictured in Fig. 2.5. The FAST telescope even though it has a very large aperture is only able to achieve an angular resolution of $\sim$ 2.9' at 21 centimetres (Goldstein et al. 2022). Other ways of creating an artificially large aperture have been developed, namely astronomical interferometers also called telescope arrays. These are sets of either full-functioning radio telescopes, or antennas spread over a large area. Each pair of antennas is sensitive to a spatial scale and orientation in the sky and measures a spatial Fourier component. With enough unique antenna pairs, or baselines, one can reconstruct the source image from the Fourier space measurements. Thus they can combined provide much higher resolution images, as the resolution is now set by the maximum baseline in the array. However the trade-off is a loss of sensitivity compared to a filled aperture dish of similar size. The sensitivity of a telescope is related to the area of its dish, but even though interferometers may have huge synthetic apertures, only small parts of the aperture is actually covered by dishes/antennae, so the ability to collect light is much worse than an actually filled aperture of the same size. The size of the new, artificial aperture is now fully defined by the the greatest separation between two of the antennas, also called the maximum baseline. Astronomical interferometers have the great advantage that they can be spread all over the globe and in space, creating an unfathomably large aperture compared to their single dish counterparts. This is called Very Long Baseline Interferometry (VLBI), and requires a lot of effort, as it is much easier to have all antennae localised in one area. The Karl G. Jansky Very Large Array (VLA) and the Low Frequency ARray (LOFAR) are examples of astronomical interferometers. VLA consists of 27 antennas, each with an aperture of 25 metres arranged on a three-armed array in a Y-shape in the deserts of New Mexico, USA (Thompson et al. 1980). The antennas' positions in the array are changed every six months, with the largest possible baseline being 36 kilometres, an aperture that would be completely unfeasible for a single dish telescope [1]. One of the arms of the VLA's three armed array is shown in Fig. 2.5. The Low Frequency Array (LOFAR) consists of a total of 40 antenna stations in the Netherlands and one in each of France, the United Kingdom, Germany and Sweden (van Haarlem et al. 2013). With stations spread across several countries, LOFAR has a huge possible maximum baseline of 1000 km, although other difficulties are encountered at such a large baseline, such as the dynamic nature of the ionosphere, which has to be accounted for (van Haarlem et al. 2013).

2.7 Brightness temperatures

One of the most important observational parameters is brightness temperature (T_B), being the temperature a hypothetical black body with the same specific intensity or brightness would have (B_ν) at the observed frequency (ν) (Rybicki & Lightman 1985). Brightness temperature is related to specific intensity and frequency through Planck's law, here written in per unit frequency:

$$B_\nu = \frac{2h\nu^3/c^2}{\exp(\mathrm{h}\nu/\mathrm{k_B T_B}) - 1}, \tag{2.3}$$

where B_ν is brightness, h is the Planck constant, ν is frequency, c is the speed of light, k_B is the Stefan-Boltzmann constant and T_B is brightness temperature (Rybicki & Lightman 1985). As we deal with low frequencies in radio astronomy, Planck's law reduces to:

$$B_\nu = \frac{2\nu^2 k_B T_B}{c^2}, \tag{2.4}$$

[1] Please refer to the following webpage for further details: https://astronomy.swin.edu.au/cosmos/V/Very+Large+Array

which is known as the Rayleigh-Jeans law(Rybicki & Lightman 1985). As we don't measure brightness in our surveys, but rather measure flux, we relate brightness to flux through the relation:

$$F_\nu = B_\nu \pi \left(\frac{R}{d}\right)^2, \tag{2.5}$$

where F_ν is flux per unit frequency, R is stellar radius and d is the distance to the star. Combining equations (2.4) and (2.5) yields an expression for brightness temperature as a function of flux:

$$F_\nu = \frac{2\pi\nu^2 k_B}{T_B}\left(\frac{R}{d}\right)^2 \tag{2.6}$$

$$\Rightarrow T_B = \frac{F_\nu}{2\pi\nu^2 k_B}\left(\frac{d}{R}\right)^2. \tag{2.7}$$

2.8 The Rossby number

The Rossby number is a measure of the importance of the Coriolis force in comparison with inertial forces, and is defined accordingly as the ratio of inertial force to Coriolis force

$$R_O = \frac{U}{fL}, \tag{2.8}$$

where U is a characteristic velocity scale and L is the characteristic length scale of a dynamic feature affected by Coriolis force (Mason et al. 2023), and f is the Coriolis parameter. The Coriolis parameter is a function of rotation rate Ω and latitude φ and can be expressed as

$$f = 2\Omega \sin\varphi. \tag{2.9}$$

In astrophysics, the Rossby number is more commonly thought of as the rotation period divided by the local convective turnover scale computed at a factor of scale height (Rucinski & Vandenberg 1986);

$$R_O = \frac{P_\mathrm{rot}}{\tau_c}. \tag{2.10}$$

Noraz et al. (2022) have derived the empirical relation between a star's Rossby number and its rotation, effective temperature and metallicity to be:

$$\frac{R_{O_f}}{R_{O_{f,\odot}}} = \left(\frac{P_{\mathrm{rot},*}}{P_{\mathrm{rot},\odot}}\right) \times \left(\frac{T_\mathrm{eff}}{T_{\mathrm{eff},\odot}}\right)^{3.29} \times \left(\frac{[\mathrm{Fe/H}]+2}{2}\right)^{-0.31}. \tag{2.11}$$

This relation was derived for Sun-like stars, but we still use the relation for our entire sample of A- to M type stars. Since not all stars have reported metallicites, Noraz et al. (2022) also show the relation between a star's rossby number and its rotation period and effective temperature only. This relation is given as:

$$\frac{R_{O_f}}{R_{O_{f,\odot}}} = \left(\frac{P_{\mathrm{rot},*}}{P_{\mathrm{rot},\odot}}\right) \times \left(\frac{T_\mathrm{eff}}{T_{\mathrm{eff},\odot}}\right)^{3.29}. \tag{2.12}$$

For the values of the solar rotation period and effective temperature, Noraz et al. (2022) state that $T_{\mathrm{eff},\odot} = 5772$ K and $P_{\mathrm{rot},\odot} = 27.3$ days should be used.

Chapter 3

Data and Methods

3.1 Radio Surveys

We work with sky cutouts from six radio surveys in this project, covering the frequency range from 72 MHz to 3 GHz. All of these radio surveys have publicly available data, so no specific observation requests were made to any of the six surveys. Some of the surveys are not finished, and in these cases the latest data releases were used. As the six surveys don't all originate from the same groups, the sky cutouts were queried differently depending on the survey, and this process of querying sky cutouts is covered in Sect. 3.3. Brief descriptions of the six surveys are found below, arranged in order of lowest frequency to highest frequency.

3.1.1 The Galactic and Extra-Galactic All-Sky MWA Survey (GLEAM)

The Galactic and Extra-Galactic All-Sky MWA Survey (GLEAM) is a survey covering the entirety of the radio sky south of the declination $\delta = +25°$, made with the Murchison Widefield Array (MWA) in Western Australia (Wayth et al. 2015). GLEAM covers the frequency range between 72 and 231 MHz, divided into five bands. The image resolution and sensitivity depends on several factors, such as observing frequency and sky pointing, and the resolutions and sensitivities are therefore not consistent between the various survey images from GLEAM. Wayth et al. (2015) provide a function for estimating the spatial resolution of an image at 154 MHz in arcminutes as a function of only its declination:

$$\text{Resolution} = 2.5 \cdot 2.2\sec\left(\delta + 26.7°\right), \tag{3.1}$$

where δ is the image's mean declination. Wayth et al. (2015) state that the sensitivities of the images from GLEAM range between 6 to 10 mJy/beam, while the resolution lies at around 2', poorer than any of the other surveys we consider.

3.1.2 LOFAR Two-metre Sky Survey (LoTSS)

The LOFAR Two-metre Sky Survey (LoTSS) is a 120-168 MHz imaging survey meant to eventually cover the entire northern sky, with the ability to produce 5" resolution images with a sensitivity of 100 μJy/beam at most declinations (Shimwell et al. 2017). As the survey is still ongoing, we only use data from its second and newest data release. The second data release presents 6" resolution images with a median rms sensitivity of 83 μJy/beam covering 27% of the northern sky. The coverage is divided into two regions centred at approximately 12h45m +44°30' and 1h00m +28°00', spanning 4178 and 1457 square degrees respectively (Shimwell et al. 2022).

3.1.3 The GMRT 150 MHz all-Sky radio Survey alternative data release (TGSS ADR1)

National Centre for Radio Astrophysics - Tata Insitute of Fundamental Research (NCRA-TIFR) in Pune, India launched the TIFR GMRT Sky Survey (TGSS) project in 2010, where the Giant Metrewave Radio Telescope (GMRT) was used to observe nearly the entire sky at 150 MHz, and observations were made between April 2010 and March 2012.[1]. The data collected by the TGSS project remained largely unpublished until Intema et al. presented the first alternative data release from the TGSS project, which they called The GMRT 150 MHz all-sky radio survey (also TGSS)(Intema et al. 2017). Through the use of their automated data reduction pipeline Intema et al. (2017) were able to produce high quality images covering the sky between the declinations of -53° and 90°, corresponding to about 90 percent of the entire sky. The majority of their images have the approximate resolution of 25" and a noise level below 5 mJy/beam.

3.1.4 Rapid ASKAP Continuum Survey (RACS)

The Rapid ASKAP Continuum Survey (RACS) is the first large sky survey to be conducted using the Australian Square Kilometre Array Pathfinder (ASKAP) telescope, located in Western Australia (McConnell et al. 2020). The survey will eventually cover the entire sky visible from the ASKAP site, covering the full ASKAP band of 700-1800 MHz. Eventually RACS will produce radio images with 15" resolution with a sensitivity of 25". As RACS is not finished observing, we use data from its first and newest data release. RACS' first data release contains radio images at the central frequency of 887.5 MHz convolved to a common resolution of 25" covering the large and continuous region in the declination range $\delta = -80°$ to $+30°$ (Hale et al. 2021).

3.1.5 VLA Faint Images of the Radio Sky at Twenty-Centimeters (FIRST)

The Karl G. Jansky Very Large Array Faint Images of the Radio Sky at Twenty Centimetres (VLA FIRST) was a project designed to produce high resolution images at twenty centimetres (1.4 GHz) over two regions whose areas make up around 10,000 square degrees. Observations with the VLA for the survey were started in the VLA's B-configuration in the spring of 1993, and were finished in the spring of 2004. However, some additional data in the southern Galactic cap were acquired in the springs of 2009 and 2011.[2] The produced images have typical root mean square noise of 0.15 mJy and resolutions of 5", with 1.8" pixels.[3]

3.1.6 VLA Sky Survey (VLASS)

The VLA Sky Survey is a close to all-sky radio sky survey, observing the entire sky observable from the Karl G. Jansky Very Large Array (VLA), which relates to everything above a declination of $-40°$ (Lacy et al. 2020). The survey is meant to eventually use $\sim$ 5500 hours of observation time at the VLA, distributed over three

[1] http://www.ncra.tifr.res.in/ncra/outreach/press-releases/exciting-new-sky-survey-with-gmrt
[2] http://sundog.stsci.edu/first/obsstatus.html
[3] http://sundog.stsci.edu/

epochs, only two of which are finished and publicly available. The observations began in September 2017, the third and final epoch started observations in January 2023 and is set to finish by the end of 2024. https://science.nrao.edu/vlass) According to (Lacy et al. 2020) the VLA Sky Survey has the unique combination of high angular resolution of $\sim 2.5''$, a good sensitivity of $70\mu Jy/beam$, a wide bandwidth covering the frequency range of $2-4$ GHz, as well as the advantage of time domain coverage over the three epochs to better detect transient sources.

3.2 Constructing the star catalogues

3.2.1 Initial star catalogue from Gaia DR3

As an initial catalogue of sources we expect to observe in the various radio surveys we use the third and newest data release from the Gaia spacecraft operated by the European Space Agency (ESA), released to the public on 13 June 2022 [4]. The construction of the Gaia spacecraft was approved in 2006, but the craft was not launched before 19 December 2013, and reached its operating point, the second Lagrange point (L2) some weeks later (Gaia Collaboration et al. 2016). The L2 point is one of the points discovered by mathematician Joseph Louis Lagrange where the gravitational forces and the orbital motion of a body balance each other, and therefore allows the body to stay "in-line" with the Earth at all times, a huge advantage both when it comes to communication and blocking out the light from the Sun and the Earth [5]. The commissioning of the Gaia spacecraft and its payload was completed on 19 July 2014, and its initially five year mission commenced shortly after (Gaia Collaboration et al. 2016). However, the Gaia mission has been extended several times, and is still observing (as of April 2023), and is currently planned to continue observing up until December 2025. Gaia was launched as a part of an ambitious mission to create a precise three-dimensional map of stars in our galaxy and beyond [6]. The newest and third data release from Gaia was fully released to the public on 13 June 2022. This catalogue includes the full astrometric solution, meaning positions and proper motions of about 1.46 billion sources (Gaia Collaboration 2022). As the majority of these sources are too far away to be observed in radio frequencies and we want to keep the sizes of the stellar catalogues manageable a constraint is put on the distance, where we choose 100 pc to be a reasonable cut-off point. There are 574531 sources within this distance, making up our initial, complete and non-biased stellar sample.

3.2.2 Sorting the sample into fitting categories

Our initial star catalogue from Gaia DR3 contains every source observed by the Gaia spacecraft determined to be within 100 pc from the Earth, which turns out to be 574531 sources. The stars themselves span the entire HR diagram, not only the main sequence, and analysing them together would therefore not make sense. Because of this we also group together similar stars or stars that are at the same stage in their stellar evolution, the most important category being the main sequence which is the most common group of stars. This main-sequence sample is the main focus of this project. Every non-binary star belonging to a spectral type AFGKM is permitted to be main sequence if the luminosity class is either V or not mentioned by SIMBAD. In addition

[4] https://www.cosmos.esa.int/web/gaia/dr3
[5] https://www.esa.int/Science_Exploration/Space_Science/Herschel/L2_the_second_Lagrangian_Point
[6] https://www.esa.int/Science_Exploration/Space_Science/Gaia

to this main sequence sample we create six other samples of stars based on the initial catalogue, to compile binary stars, white dwarfs, sub-dwarf stars, young stellar objects (YSOs), evolved stars and other giant stars which for some reason don't have object types coinciding with the usual evolved star classification of SIMBAD. A table showing our different star categories and their coinciding object types is shown in Table 3.1. Note that the categories are based on those of SIMBAD [7]

Main sequence sample	
MS*	Main Sequence Star
Be*	Be Star
BS*	Blue Straggler
SX*	SX Phe Variable
gD*	gamma Dor Variable
dS*	delta ScT Variable
Pe*	Chemically Peculiar star
a2*	alpha2 CVn Variable
Ir*	Irregular Variable
Er* (-RC*, RS*, No*)	Eruptive Variable
Ro* (-El*, BY*)	Rotational Variable
Pu*	Pulsating Variable
LM* (-BD*)	Low Mass star (except Brown Dwarfs)
Evolved star sample	
EV*	Evolved Star
RG*	Red Giant Branch star
HS*	Hot Sub-dwarf
HB*	Horizontal Branch star
RR*	RR Lyrae Variable
WV*	Type II Cepheid Variable
Ce*	Cepheid Variable
cC*	Classical Cepheid Variable
C*	Carbon star
S*	S star
LP*	Long-Period Variable
AB*	Asymptotic Giant Branch Star
Mi*	Mira Variable
OH*	OH/IR Star
pA*	Post-AGB Star
RV*	RV Tauri Variable
PN*	Planetary Nebula
White dwarf sample	
WD*	White Dwarf
ZZ*	Pulsating White Dwarf
ELMWD	Extremely Low Mass White Dwarf
Young Stellar Object (YSO) sample	
Y*O	Young Stellar Object
Or*	Orion Variable
TT*	T Tauri star
Ae*	Herbig Ae/Be Star
out	Outflow
HH	Herbig-Haro Object
Binary systems sample	
**	Double or Multiple Star

[7] http://simbad.cds.unistra.fr/guide/otypes.htx

El*	Ellipsoidal Variable
Eb*	Eclipsing Binary
Al*	Eclipsing Binary of Algol type
bL*	Eclipsing Binary of beta Lyr type
WU*	Eclipsing Binary of W UMa type
SB*	Spectroscopic Binary
BY*	BY Dra Variable
RS*	RS CVn Variable
Sy*	Symbiotic Star
XB*	X-ray Binary
LXB	Low Mass X-ray Binary
HXB	High Mass X-ray Binary
CV*	Cataclysmic Binary
No*	Classical Nova
NL*	Nova-like Binary
DN*	Dwarf Nova
DQ*	CV of DQ Her type
AM*	CV of AM CVn type

Table 3.1: Our star categories and their associated object types. The categories are heavily based on those of SIMBAD. See http://simbad.cds.unistra.fr/guide/otypes.htx for more details.

3.2.3 Sorting Algorithm

To sort the initial Gaia DR3 catalogue of every source within a radius of 100 pc, a sorting script is written in Python. The script loops through the catalogue and sorts the sources into the previously described star categories using the sources' stellar- and object types. A flow chart showing the workings of the script is shown in Fig. 3.1. When looping through the catalogue each source is firstly checked to see if it is part of a known binary system. The reason this check is the first one to be applied is that main sequence stars can (and are commonly) part of binary or multiple star systems, but we only want solitary main sequence stars to be part of our main sample. The binaries are filtered out into their own catalogue. After the filtering out of the binaries, the stars' luminosity class is checked to determine their placement in the HR diagram. If the luminosity class is found to be V, the star is appended to the main sample, while if the luminosity class is I, II, III, or IV it is either a super-giant, giant or sub-giant and therefore appended to the giant catalogue. And if the star's luminosity class is VI or VII it is appended to the sub-dwarf or white dwarf catalogues respectively. However, in many cases the stars don't have luminosity class information in SIMBAD, and in these cases we have to be more thorough and check the stars' object types against the allowed object types in the previously described star categories, heavily based on those of SIMBAD.

If the star is a part of each of the star categories described in Sect. 3.2.2 is checked in turn, with the first check being to see if any of the star's object types are included in the white dwarf category. If this is found to be true, the star is a white dwarf and is moved to the white dwarf sample. If this is not the case, we check if any of the object types lie in the evolved star category, and if it is the case the star is moved to the evolved star category. The same check is done for the YSO category, where the star is assigned to the YSO sample if any of its object types are parts of the allowed

YSO object types. The final check is to see if the star is a main sequence star, which similarly to the other samples is done by checking that all of its object types are parts of the allowed main sequence object types. If this is found to be the case, the star is thought to be main sequence and moved to the corresponding sample, even though no luminosity class V is given in SIMBAD. If this check fails, the star is simply discarded, as it has no further use to us.

3.3 Querying sky cutouts

As the six surveys we work with in this project do not originate from the same groups, they are not all publicly available in one space, and we have therefore had to use or develop methods of querying the various surveys for sky cutouts in a reasonable way. The sky cutouts from LoTSS, TGSS and GLEAM were the easiest to query by far, as these surveys are publicly available from the Centre de Données astronomiques de Strasbourg (CDS) or the Strasbourg astronomical Data Centre.[8] Sky cutouts from these surveys could therefore easily be queried using the astropy package in Python, and the process of querying the cutouts using this package is covered in Section 3.3.1. As for the remaining three surveys not available in CDS we had to use other means to query sky cutouts, where we ended up using the already powerful Canadian Initiative for Radio Astronomy Data Analysis (CIRADA) cutout service [9], in addition to `get_VLASS_cutouts.py` as recommended by Dr. Biny Sebastian.

3.3.1 Querying cutouts available in CDS

Cutouts from surveys that are publicly available from the Centre de Données astronomiques de Strasbourg (CDS), being LoTSS, GLEAM and TGSS, are queried directly from a python script that utilises the `astroquery.hips2fits()` method of the well known `astroquery` module. One here specifies the expected positions of the sources we wish to query cutouts of, as well as specify the desired pixel resolution of the cutouts. Appropriate pixel resolutions are computed using the reported resolutions of each of the three surveys, so that sky cutouts of size 5×5 beams can be queried.

3.3.2 Querying cutouts using the CIRADA cutout service

The CIRADA cutout service is a service developed at the Canadian Initiative for Radio Astronomy (CIRADA) for querying sky cutouts from a collection of surveys. A browser version of the cutout service is available at http://cutouts.cirada.ca/, but as it is only possible to query 200 sources at a time using that version, we resorted to using their python version of the cutout service, available at https://github.com/CIRADA-Tools/cutout_provider_core. Using this python script one can query sky cutouts from the radio surveys VLASS, GLEAM, FIRST and NVSS, the infrared survey WISE and the optical surveys PanSTARRS and SDSS. Of these we only query cutouts of the FIRST and RACS surveys using this method, as other means were more practical at the time of this project. The script is still in a developing and testing phase, and at the time of querying cutouts, only querying FIRST images worked. However, Dr. Biny Sebastian kindly provided a newer version of the script, where we could query cutouts from RACS and VLASS as well. However, the cutouts from VLASS had already been queried by

[8] https://cdsweb.u-strasbg.fr/

[9] http://cutouts.cirada.ca/

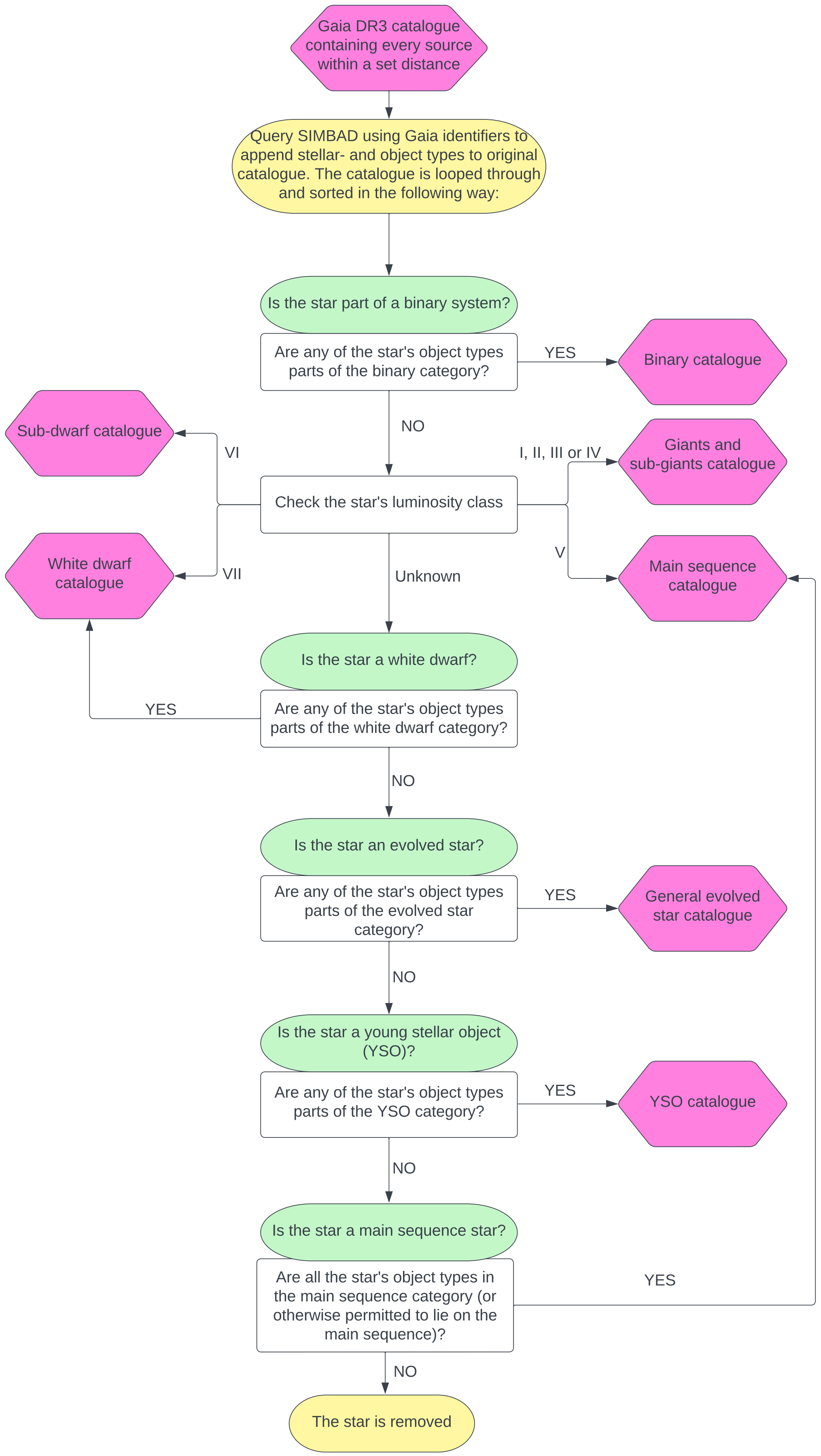

Figure 3.1: Flow chart showing how our stars are sorted into fitting categories based on their luminosity- and object types.

other means at that time. The CIRADA cutout service works by reading a given .txt file of expected positions of the sources we wish to query cutouts of. One can also specify what a radius around the source to set the size of the cutout, however the minimum radius is one arcminute.

3.3.3 Querying VLASS cutouts

As querying sky cutouts from the VLA Sky Survey (VLASS) was not available using the CIRADA cutout at the time, another method was utilised. By the recommendation of Dr. Biny Sebastian at CIRADA, the python script `get_VLASS_cutouts.py` available at https://github.com/ygordon/VLASS_cutouts was used. It is a script for querying for VLASS images centred on a specified position from the Canadian Astronomy Data Centre (CADC), and was written and uploaded to Github by Yjan Gordon. Similarly to the CIRADA cutout service, `get_VLASS_cutouts.py` works by reading an input file of the expected positions of each of the sources cutouts are desired, as well as a requested cutout radius. However, we are here able to request cutouts with smaller radii than one arcminute, something that we were not able to do using the CIRADA cutout service.

3.4 Priority sorting

Before sorting our queried cutouts into suitable categories based on the quality of the detections, we need to determine a suitable significance level. This is done in such a way that the probability of any of the pixels within the cutouts having fluxes greater than the set significance level entirely due to noise is less than 1, as explained in more detail in the following section.

3.4.1 Significance level

The significance level N is set so as to make the expected number of pixels with fluxes outside of N standard deviations of the mean entirely due to noise in our cutouts less than one. For example the probability that a single flux measurement X lies outside of 3 standard deviations of the mean (3σ) is:

$$1 - Pr(\mu - 3\sigma \leq X \leq \mu + 3\sigma) = 2.7 \cdot 10^{-3} = 0.27\%, \tag{3.2}$$

meaning that out of a hypothetical sample of 500 measurements it is expected that the number of pixels with fluxes outside of the 3σ range entirely due to noise is:

$$500 \cdot 2.7 \cdot 10^{-3} = 1.35. \tag{3.3}$$

As most of our cutouts contain more than 500 pixels and we want to keep the expected number of pixels outside of the $N\sigma$ range less than one, we need to user a higher significance level. It is here found that 4σ is more than sufficient for our cutouts, as the probability of a single pixel lying outside of this range is as small as:

$$1 - Pr(\mu - 4\sigma \leq X \leq \mu + 4\sigma) = 6.334 \cdot 10^{-5} = 0.00006334\%, \tag{3.4}$$

meaning that we can have a cutout containing $\sim$ 15787 pixels before crossing the threshold, as:

$$15787 \cdot 6.334 \cdot 10^{-5} \approx 1. \tag{3.5}$$

This corresponds to $\sim$ 125 x 125 pixel cutout. Given the interferometric beam scales and the final image pixel scales used by the surveys of interest, a 5 beam x 5 beam cutout queried from any of the survey data will never cross the limit of 125 x 125 pixel count. A significance level of 4σ is therefore chosen for the following segregation of the cutouts into priorities and classes.

3.4.2 Priority categories

The previously queried sky cutouts are sorted into three different categories, henceforth called priorities, based on the quality of the detections, if any. The sky cutouts where nicely centred sources are detected within two beams of the expected source position are designated as priority 1. This group is sub-divided into two classes, I and II, class I being nice Gaussian shaped sources, while class II are irregularly shaped. The priority 1 class I (P1C1) detections are our best detections, and are the sources which we analyse further in the Results section. In the cases where no source is detected within two beams of the expected positions, we look for secondary detections outside this threshold. The secondary sources which are found to not have Gaussian shapes are given the priority 3 class I (P3C1) designation, while the sources which are found to be Gaussian are given a designation of priority 2, once again divided into classes I and II based on the significance of the flux. The cutouts where no significant flux is detected are given a priority 3 class II (P3C2) designation, being non-detections. The different priorities and classes are described in Table 3.2.

Priority	Significant flux in cutout?	Within 2 beams of expected position?	Gaussian?	Source flux significant?
Priority 1, Class I (P1C1)	Yes	Yes	Yes	Yes
Priority 1, Class II (P1C2)	Yes	Yes	No	Yes
Priority 2, Class I (P2C1)	Yes	No	Yes	Yes
Priority 2, Class II (P2C2)	Yes	No	Yes	No
Priority 3, Class I (P3C1)	Yes	No	No	Yes
Priority 3, Class II (P3C2)	No	No	No	No

Table 3.2: The priorities and priority classes we use to sort our sky cutouts into fitting categories based on the quality of the detections.

3.4.3 Priority sorting

Initially the entire cutout is checked for pixels with significant fluxes, done by finding the pixel with the highest flux and comparing its flux with the root-mean-square noise of the cutout. If the flux is greater than 4σ the detection is deemed significant, and the cutout is let through to the next check. If the flux is smaller than 4σ there are no significant detections in the cutout and the cutout is designated Priority 3 class II, the worst priority designation in our sample.

The cutouts which we now know contain significant fluxes are run through a new check, that checks if any significant source can be found at the expected position of the source the cutouts were queried based on, where we allow a deviation of two beams from the expected position to still be counted as a central detection. The cutouts that pass this test are fitted with Gaussian functions centred on the position of the central source using one of the built-in function in CASA. If the fitting function converges the cutouts is given a Priority 1 Class I designation, the best designation given to any of the cutouts in our sample, only given to significant, centred and Gaussian sources. However, if the fitting function fails to converge the cutout is given a Priority 1 Class II designation, still a good detection, but the source might not be shaped like a Gaussian function, which could be caused by a lot of factors.

Meanwhile, cutouts where no significant flux is found within two beams of the expected position is run through another check. As with the central detections we here try to fit a Gaussian function to the previously found non-centred source. If the fitting function fails to converge the cutouts is given a Priority 3 Class I designation, slightly better than the Class II equivalent, as we now know that the cutouts does indeed contain a significant flux, although it is not found to be Gaussian. In the cases where the fitting function converges successfully the cutout is given a Priority 2 designation, meaning a good secondary detection is found in the cutout. The two classes are here separated based on the significance of the flux of the source. If the flux is found to be greater than 4σ the cutout is designation to Class I, while everything less than 4σ is designated to Class II.

3.4.4 Filtering out false P1C1 detections

The surveys with lower pixel resolutions such as VLA FIRST and VLASS, where a point source just spans a few pixels, our script for sorting the sky cutouts into fitting categories sometimes fail, as CASA can fit a Gaussian function over several bright points in the image, or simply due to some of the cutouts being very noisy. As a crude solution to this we go through all detections by-eye and remove any that are obviously false detections. After finally having a good sample of actual detections we are ready to query the stellar parameters associated with the detected stars, which allows us to begin our analysis.

3.5 Querying stellar parameters

One of the goals of this project is to explore possible relations between the stellar parameters of detected sources and their observational properties in the various surveys. Since very few stellar parameters are included in the Gaia DR3 catalogue, we need to query stellar parameters of our sources. This is done using Vizier ALMA and SIMBAD

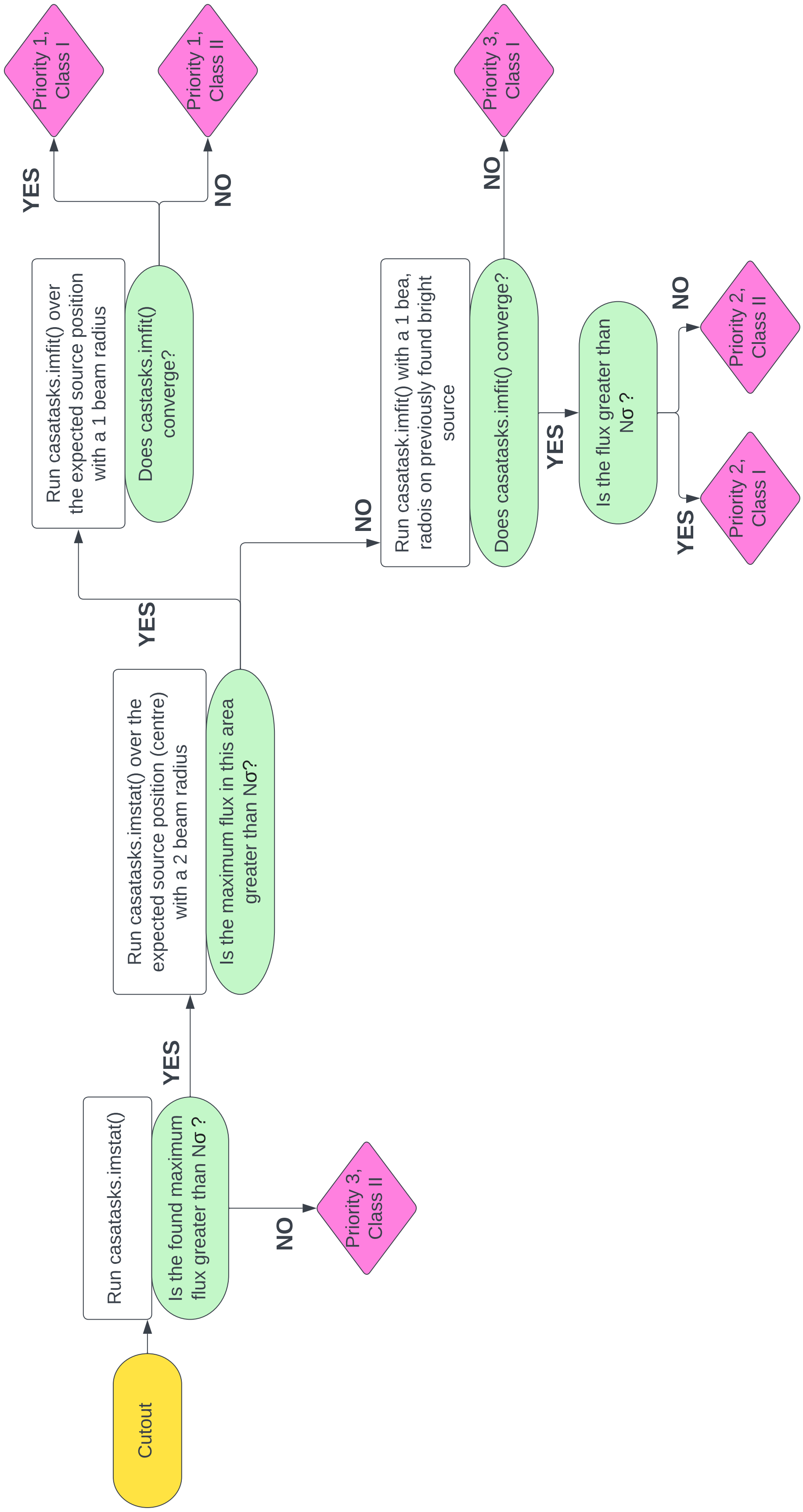

Figure 3.2: Flow chart describing the process of segregating the sky cutouts based on the quality of the detection into three different priorities, each divided into two classes.

Explorer (VASE), a python script originally developed to be used in the Exploring Millimetre Indicators of Solar-Stellar Activity (EMISSA) project at Rosseland Centre for Solar Physics (RoCS) Mohan et al. (2021), Mohan et al. (2022). VASE is a very flexible script, that can be used to query desired stellar parameters from any specified or non-specified publicly available catalogues in Vizier. A .txt file of important catalogues is required for VASE to know which catalogues to search initially, but if not all the desired stellar parameters are found within these catalogues, VASE resorts to search all the publicly available catalogues in Vizer for the remaining parameters. VASE requires a .txt file containing the SIMBAD main ids of the stars it is to look for stellar parameters for, and the parameters of interest must also be specified, in addition to the permitted units of the specified parameters.

Chapter 4

Results

4.1 Stellar sample

We here present the samples of detected stars in the considered radio surveys. Unfortunately, we were not able to find any significant evidence of stellar emission in GLEAM, and as such no results are presented for this survey. In the remaining surveys we detect several single main sequence stars. In LoTSS we detect a total of **90** main sequence stars, in TGSS we detect **151**, in RACS **124**, in VLA FIRST **11** and in VLASS we detect **103** main sequence stars. In addition, the samples of detected evolved stars, white dwarfs, young stellar objects and binary stars are presented briefly in Sect. **X**. These samples are not analysed any further as the focus of this study in on main sequences stars but can be used for future investigations.

4.1.1 Lofar Two-metre Sky Survey

Fig. 4.1 contains bar charts showing the distributions of main sequence detections across our priority categories in LOFAR Two-metre Sky Survey (LoTSS). Because of the much better pixel resolution in LoTSS compared to VLASS and VLA FIRST no by-eye filtering is needed to filter out false detections, as the script is much better at LoTSS' resolution. We still go through the cutouts to look for false detections, but none are found. Fig. 4.1 shows that we have a large fraction of secondary detections in LoTSS, being detections of stellar emission outside a two-beam radius of the expected position. We find a nice correlation between the number of good (P1C1) detections and the stellar type, the number of good detections increasing as we approach smaller and cooler stars. We detect 90 single main sequence stars in LoTSS, and the detected stars are summarised in Table 4.1.

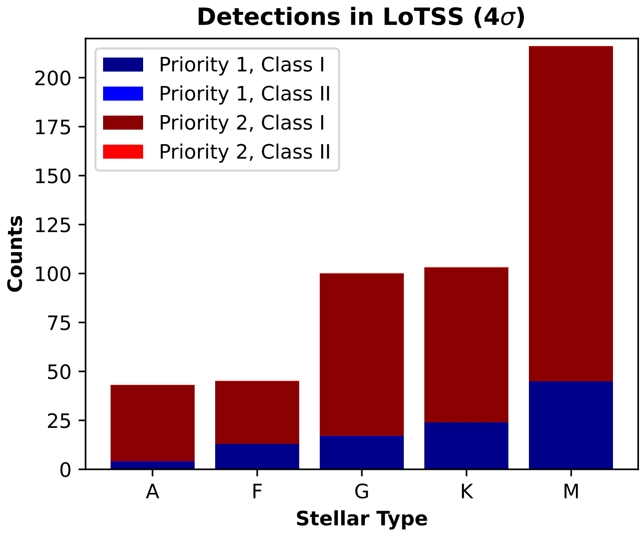

Figure 4.1: Bar chart showing the distribution of stellar detections in LOFAR Two-metre Sky Survey (DR2) over stellar type.

Main sequence P1C1 detections in LOFAR Two-metre Sky Survey (LoTSS)					
SIMBAD ID	Type	RA [deg]	DEC [deg]	S_I [mJy]	Distance [pc]
V* BP Boo	A0VpSiCr	235.7243	52.3708	0.3731	91.7910
HD 218079	F0	346.2643	18.6424	1.3613	74.8618
HD 130786	F8	222.2650	36.0736	0.5845	59.4812
BD+62 1281	F8	197.7467	61.7525	1.2097	59.4857
HD 14348	F5	34.9896	31.3446	10.5099	60.2936
HD 123573	F8	211.8160	46.8441	0.6858	91.7082
HD 98044	F2	169.4111	67.8883	0.7747	96.0068
HD 108954	F9V	187.7191	53.0877	0.3515	22.3091
HD 134788	F8	227.3593	57.1258	2.0553	99.9153
HD 86964	F5	150.9647	59.8764	0.3561	93.1054
BD+64 1099	F8	238.4006	64.5570	2.3008	99.0186
HD 125858	F5	215.2832	38.9964	36.6750	82.2106
HD 150234	G0	249.0685	59.3418	0.7550	74.9101
HD 113319	G4V	195.6551	32.4430	1.1627	31.7461
HD 55918	G5	109.1119	35.0257	4.2787	36.5245
HD 78366	G0IV-V	137.2310	33.8862	10.9125	18.9498
HD 10126	G8V	24.9181	28.1194	1.5412	31.7556
HD 117122	G5	201.8757	44.7139	0.4323	55.5621
HD 115734	G5	199.5516	51.5132	0.4479	97.4045
HD 132562	G5	224.5412	48.0369	0.3631	58.0247
HD 82733	G5	143.8009	43.6866	0.6329	47.4072
BD+37 2777	G0V	249.2439	36.9233	0.5348	92.5426
HD 58947	G5	112.2379	26.6304	2.8274	90.4784
BD+49 1932	G0	153.5259	48.8296	27.9091	89.7498
BD+26 4715	G5	359.2934	27.7865	0.4731	84.3170
HD 115349	G5V	199.0572	35.8952	0.4892	46.9952
BD+35 2336	G6V:	186.1330	34.9803	1.0961	93.6314
HD 63932	G5	118.5799	54.7206	0.5961	64.2620
HD 101240	G0	174.8679	64.0777	1.2693	84.9916
BD+66 995	G5	256.7559	65.9746	1.7739	78.2337
StKM 1-915	K4	167.2759	35.5174	0.8596	61.7160
StKM 1-912	K5	166.6693	57.9157	4.5394	80.5236
BD+51 1567	K4V	150.5189	50.9340	0.9583	47.0098
BD+49 2212	K0	201.0959	48.8948	0.6060	61.4761

BD+41 2091	K2V	156.8379	40.7252	0.7091	41.8838
G 123-33	K5V	186.6048	35.9396	12.6883	47.7812
StKM 1-1190	K5	222.4820	48.5663	0.3964	65.8401
BD+37 2401	K2	200.5043	36.6049	0.6155	70.0692
StKM 1-876	K4/5	160.8436	53.4609	0.4403	67.8875
StKM 1-954	K5	172.8145	50.2110	0.9605	92.9368
2XMM J115846.5+434735	K3:V	179.7021	43.8032	1.4366	76.0866
BD+35 2024	K0	143.8307	35.0589	0.5278	82.4570
G 164-7	K2V:	189.5164	31.1626	0.6034	86.4249
BD+38 2612	K4/5	225.4126	37.8086	0.6029	61.3223
StKM 1-789	K5	144.5790	40.2570	2.3718	38.2560
HD 82882	K0	144.0578	44.5775	0.6437	62.5719
BD+63 1004	K0	184.4209	62.4371	0.2595	61.5723
BD+39 2428	K0	168.1843	39.1579	0.4659	92.8431
BD+33 4737	K0	353.6654	34.0539	0.8144	49.9472
HD 90875	K4/5V	157.7091	59.7557	0.5154	23.5104
HD 95419	K3V	165.3310	29.5990	0.5433	49.5773
StKM 1-647	K5	112.0516	38.6612	1.6442	58.6413
PM J12324+3028	K2V:	188.1206	30.4806	3.0487	50.7212
BD+40 2365	K5	161.3044	39.5923	1.3804	47.1423
BD+31 2691	M0	226.3395	30.9376	0.6302	74.5689
2MASS J12585353+3711365	M7V	194.7340	37.1988	0.5614	79.5540
2MASS J10581684+6451494	M9V	164.5820	64.8791	0.4936	95.6671
Ross 324	M0V	19.4721	28.6754	0.9542	16.7093
V* CW UMa	M3.5V	167.9780	33.5468	1.1031	13.3540
2MASS J12341542+4813070	M3	188.5807	48.2273	0.9135	46.8271
G 74-29	M3	38.5194	41.7869	0.5635	22.1049
SDSS J133136.80+541104.5	M8	202.9198	54.1962	0.6765	93.0855
RX J1419.0+6451	M3	214.7758	64.8725	5.3054	44.9809
LSPM J0755+5257	M3.60	118.8110	52.9782	0.6912	24.0623
2MASS J12470291+5034285	M7V	191.7696	50.5892	2.6570	90.9246
2MASS J14293163+5938102	M6V	217.3945	59.6518	0.6184	88.2778
UCAC4 617-051335	M2.3	227.9587	33.2338	0.7206	98.3774
LP 92-297	M0.0V	161.7895	57.2192	0.6649	38.1780
UCAC4 729-050408	M1.6	206.0650	55.6414	1.2602	69.7596
SDSS J135936.53+291010.3	M8	209.9152	29.1833	0.6526	55.7726
2MASS J13032398+3602486	M9V	195.8644	36.0590	0.5424	43.9177
G 176-14	M3.8	166.5343	42.8993	1.7790	67.6415
LP 270-17	M2.9	209.3643	34.0166	1.6051	53.8926
2MASS J11192504+5947125	M8V	169.8683	59.7999	2.1178	98.5592
LP 257-1	M2.9	117.7662	35.0380	1.2789	70.7087
LP 124-56	M4V	129.9354	53.1637	0.6305	80.5945
2MASS J16104135+5047114	M4.2	242.6818	50.7986	10.7495	84.2151
G 122-49	M4.5V	177.7417	48.3834	0.5517	8.0426
Ross 493	M1.5V	207.1514	56.3429	0.9913	31.9241
2MASS J12344887+4444174	M7V	188.7142	44.7534	1.7262	83.6691
G 202-44	M4.0	245.4841	43.9229	0.7569	44.2742
[BHR2005] 263-27	M3V	155.2915	43.4969	0.6908	64.5759
2MASS J13275491+5143565	M7V	201.9895	51.7477	0.4420	70.1233
LP 124-51	M3.3	129.2146	54.1254	0.3236	43.4035
LP 266-67	M5V	187.6678	37.8478	1.0249	75.2209
G 223-74	M3.0Ve	219.2392	58.3540	0.7495	18.4555
LP 212-62	M5.0V	155.9805	43.9022	6.2003	18.1903
LSPM J1334+6830N	M1	203.6482	68.5199	0.5541	49.7150
Sand 175	M3:	194.4596	32.1497	0.5925	49.7396
UCAC4 689-054546	M2.6	211.1989	47.6493	1.1892	98.5549
[BHR2005] 161	M4V	148.1607	47.4422	0.4917	60.3954

Table 4.1: Table of P1C1 detections in LOFAR Two-metre Sky Survey (LoTSS).

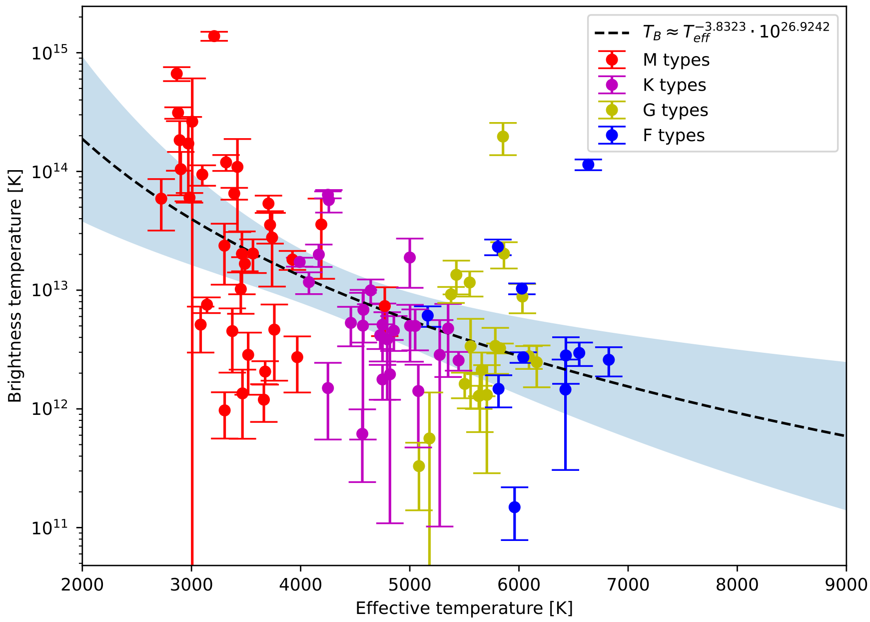

Figure 4.2: Brightness temperature versus effective temperature for the sources we detect in LoTSS. A first order polynomial fit is done on $\log(T_B)$ vs $\log(T_{\text{eff}})$, indicated by the dashed black line, with blue indicating the 3σ region.

We relate the computed brightness temperatures of the detected sources to their effective temperatures, which is a good way to show which types of main sequence stars are brighter in radio. Note that the origin of the incoming radio emission is likely non-thermal, meaning that the brightness temperatures are not physical temperatures. A plot of brightness temperature against effective photospheric temperature is shown in Fig. 4.2. We here find that the cooler, smaller and less massive M-dwarfs are generally brighter at 144 MHz compared to the more massive, larger and hotter K-, G- and F-dwarfs. To try and show this relation better we perform a first-order polynomial fit on the logarithm of both brightness- and effective temperature. This fit yields the following relation,

$$T_B \approx T_{\text{eff}}^{-3.8328\pm1.917} \cdot 10^{26.9242\pm6.99}, \tag{4.1}$$

and this relation is shown in Fig. 4.2 as a dashed black line. The given uncertainties correspond to the three sigma level, meaning that the relation between brightness- and effective temperatures is statistically significant. From this relation it is obvious that the cooler stars are generally much brighter at 144 MHz compared to their hotter counterparts. For example, a star with an effective temperature of 3000 K, corresponding to a star of type M5V, would have a brightness temperature at 144 MHz of $\sim 4 \cdot 10^{13}$ K, while a star with an effective temperature of 6000, corresponding to a star of type F9V, would have a brightness temperature of $\sim 2.7 \cdot 10^{12}$ K, a difference of roughly an order of magnitude. Fig. 4.2 also shows that sample of stars deviate quite a lot from the fitted function in many cases, maybe most obviously for some of the K and M dwarfs. Some K dwarfs are observed to be considerably less bright than the fitted function, in the worst case almost having two orders of magnitude less brightness temperature than the fitted function. The M dwarfs are clearly separated into two groups, the hottest

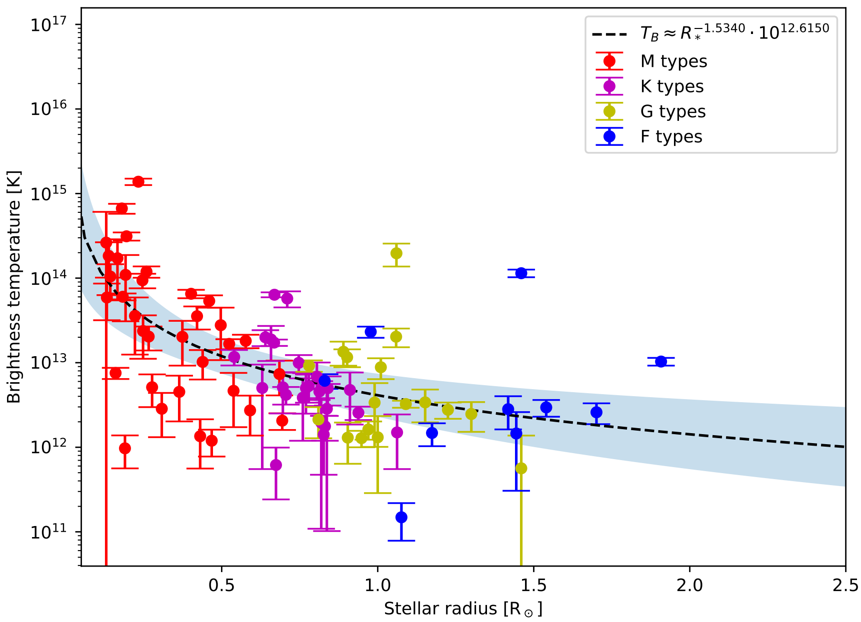

Figure 4.3: Brightness temperature versus stellar radius for the sources we detect in LoTSS. A first order polynomial fit is done on log(TB) vs log(R), indicated by the dashed black line.

half of the M dwarfs generally being cooler (in T_B) than the fitted function, while the cooler half of the M dwarfs generally have higher brightness temperatures than the fitted function. The two groups also deviate by almost two orders of magnitude from the fitted function in their respective directions. Interestingly we also find one G star and a F star that have brightness temperatures far higher than expected of stars with similar temperatures, both having brightness temperatures on the level of some of our M dwarfs. These two outliers are discussed further in Section 5.4.1.

As we have already seen that brightness temperatures seem to increase towards cooler stars (see Fig. 4.2), it is therefore no surprise that the brightness temperatures seem to also increase with decreasing radius towards smaller stars (see Fig. 4.3). The most dramatic increase is found for stars smaller than $\sim 0.35\ R_\odot$. A first-order polynomial fit on the logarithms of both brightness temperature and stellar radius yields the following relation:

$$T_B \approx R^{-1.5340\pm0.675} \cdot 10^{12.6150\pm0.255}, \tag{4.2}$$

where the uncertainties correspond to the 3σ level, meaning that the relation is once again statistically significant. A black dashed line is used to indicate the fitted function in Fig. 4.3. Following the fitted function from short to long radii, an initial sharp decrease in brightness temperature is observed up until around 0.5 R$_\odot$, spanning most of the M dwarfs in the sample. Once again it is evident that our M dwarfs have brightness temperatures spanning around three orders of magnitude in brightness temperatures, which could be because of the incoming radio emission having different origins in the different M dwarfs. The two outlying G and F dwarfs are also found in Fig. 4.3, as they also have much higher brightness temperature then their similarly sized counterparts.

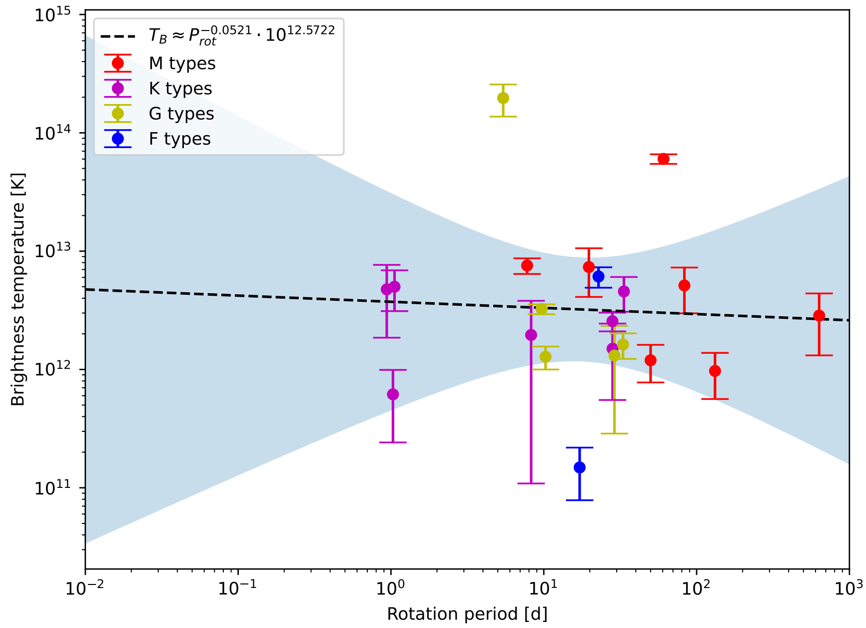

Figure 4.4: Brightness temperature versus rotation period for the sources we detect in LoTSS. A first order polynomial fit is done on $\log(T_{\rm b})$ vs $\log(P)$, indicated by the dashed black line.

Although already having found that cool and small stars are generally brighter at 144 MHz, the reasons for which are yet to be explored. One way of investigate the activity of our sample is to further analyse the relation between the stars' rotational periods and brightness temperature. However, only a small minority of the stars we detect in LOFAR have reported rotation periods in Vizier, so that the plot of brightness temperature versus rotational period in Fig. 4.4 includes much fewer stars than the two previous plots, therefore making it harder to find a meaningful relation between the two properties. As we have so few stars with reported periods in Vizier, using the sample to show some relation between brightness temperature and rotational period with any confidence is not really possible. Almost all sources with reported rotation periods have brightness temperatures between 10^{12} and 10^{13} K, spanning a relatively large range of periods from rapidly rotating K dwarfs with periods around 1 day to very slowly rotating M dwarfs with periods around 800 days. Because of this, the relation (if any) looks to be very flat, with some very noticeable outliers, namely a G- and a M dwarf with brightness temperatures around two orders of magnitude greater than stars with similar periods. As before we perform a first-order polynomial fit to our data, and the relation is found to be:

$$T_B = P^{-0.0521\pm0.648} \cdot 10^{12.5722\pm0.918}, \tag{4.3}$$

with uncertainties corresponding to the 3σ level, meaning that the relation between rotation period and brightness temperature is far from statistically significant. This is also evident by looking at Fig. 4.4 where the 3σ confidence region is very large, so that the possible relation between the two quantities can be both positive and negative.

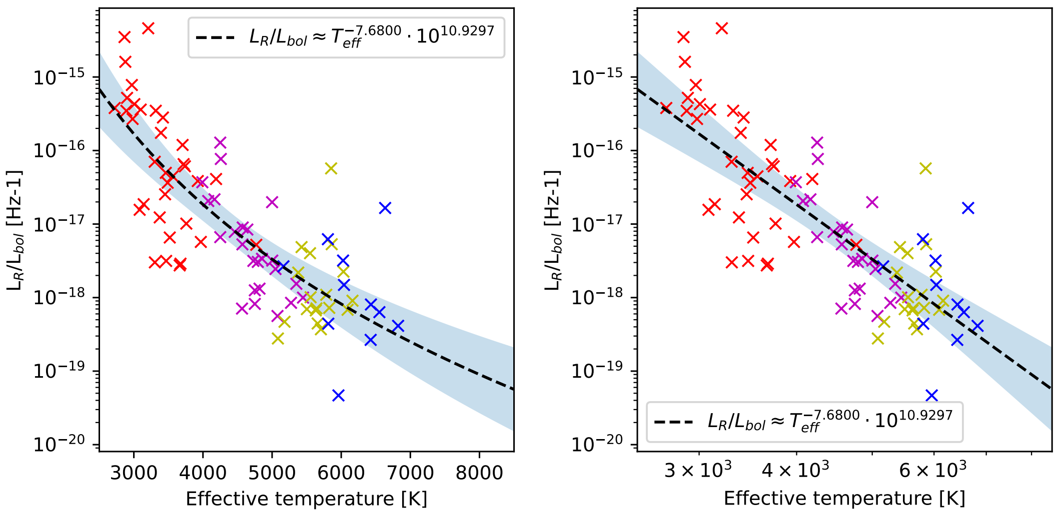

Figure 4.5: Plot of the ratio of radio- to bolometric luminosity as a function of effective temperature, both in lin-log and log-log scale. A first order polynomial fit of the logarithms is shown as a black dashed line in both plots. The log-log plot shows a neat linear relationship between the logarithm of L_R/L_{bol} and the logarithm of T_{eff} at 144 MHz.

Alternatively to non-thermal brightness temperatures, for which the interpretation might not be intuitive, it is useful to look at how the fraction of the radio luminosity L_R over the bolometric luminosity L_{bol} evolves as a function of different stellar parameters. This is a way of clearly showing which stellar parameters are important when it comes to a star's brightness in radio frequencies. However, comparing L_R/L_{bol} to stellar parameters is very similar to relating brightness temperatures to the same parameters, so no new, surprising relations are expected. Once again, as all the stars in our sample do not have reported bolometric luminosities, the star sample plotted in the following figures is slightly smaller than some of the ones above. We begin by plotting ratio of radio luminosity over bolometric luminosity as a function of effective temperatures as shown in Fig. 4.5. The right-most plot with a linear x-axis of effective temperatures, while the left-most has a logarithmic x-axis of temperatures. As before we perform a first-order polynomial fit the log-log values, yielding the following relation:

$$L_R/L_{\mathrm{bol}} \approx T_{\mathrm{eff}}^{-7.6800\pm1.887} \cdot 10^{10.9297\pm6.882}, \tag{4.4}$$

and the relation is shown as a black dashed line in both windows of Fig. 4.5. The relation is also found to be statistically significant. It is here observed that the stars with bolometric luminosity values follow the fitted relation quite well, but as before the spread is quite large. However, it is immediately evident that the trend in the log-log plot looks very close to linear, increasing our confidence in our fit. We also note that the previously mentioned outlying G and F dwarfs are still clearly visible in Fig. 4.5.

As we did for brightness temperatures, we now try to relate the ratio of radio- to bolometric luminosity to stellar radius, a plot of which is shown in Fig. 4.6. The trend is not as obvious in Fig. 4.6 as in the L_R/L_{bol} versus T_{eff} plots in Fig. 4.5, but we still try to perform a first-order fit of the log-log values. This yields the following relation,

$$L_R/L_{\mathrm{bol}} \approx R_*^{-2.6774\pm0.684} \cdot 10^{-17.6588\pm0.258}, \tag{4.5}$$

with uncertainties corresponding to the 3σ level, meaning that the relation is statistically significant. As was the case when we previously tried to relate brightness temperatures to rotational periods in Fig. 4.4, we still have only a few stars in our sample that have reported rotation periods in Vizier. Because of this, our attempt to relate the two quantities in Fig. 4.7 yields no obvious trend. As previously, a first-order fit is performed on the log-log values, yielding the relation,

$$L_R/L_{\mathrm{bol}} \approx P_{\mathrm{rot}}^{0.2512\pm0.777} \cdot 10^{-17.8752\pm1.104}. \tag{4.6}$$

Contrary to the fitted relation between brightness temperature and rotational period, this new relation is slightly increasing for longer rotational periods. However, the slope is not statistically significant in either of the two period fits, as we have so few data points.

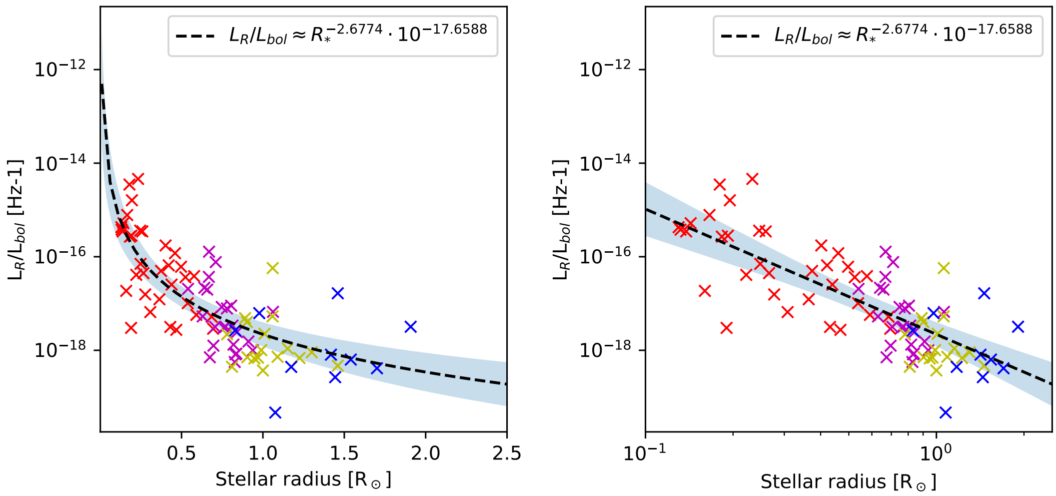

Figure 4.6: Plot of the ratio of radio- to bolometric luminosity as a function of radius, both in lin-log and log-log scale. A first order polynomial fit of the logarithms is shown as a black dashed line in both plots.

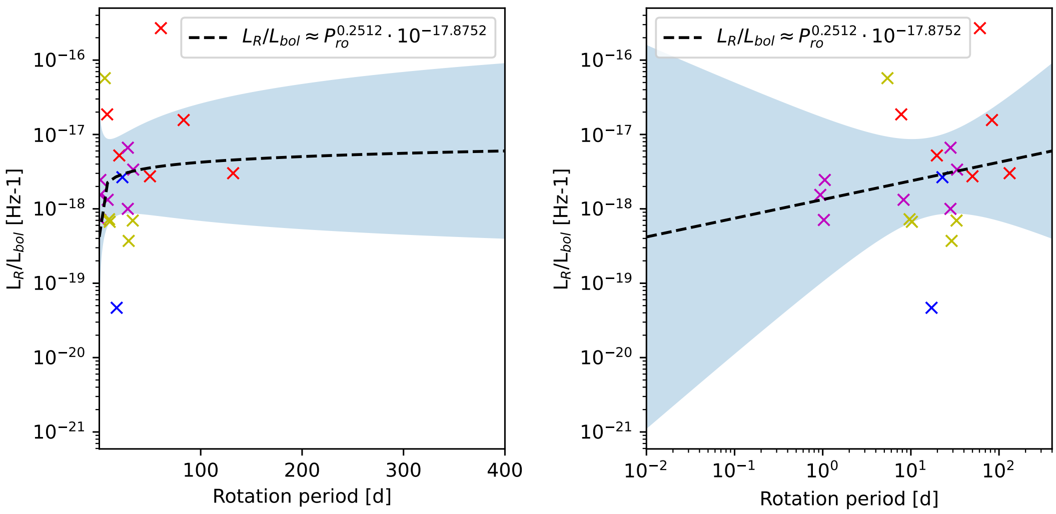

Figure 4.7: Plot of the ratio of radio- to bolometric luminosity as a function of period, both in lin-log and log-log scale. A first order polynomial fit of the logarithms is shown as a black dashed line in both plots.

As a final comparison we try to relate the Rossby number to the ratio of radio- to bolometric luminosity, as in previous studies it has been found that the ratio of X-ray to bolometric luminosity as a function of Rossby number saturates and flattens out at a Rossby number of ~ 0.1. It could therefore be expected that a similar phenomena could be found in relating the ratio of radio- to bolometric luminosity, a plot of which is shown in Fig. 4.8. No obvious saturation is here found, as a the radio luminosity fraction appears to decrease for lower Rossby numbers. As before we perform a first-order fit on the log-log data, yielding the following relation with uncertainties corresponding to the 3σ level.

$$L_R/L_{\text{bol}} \approx R_O^{-0.1257\pm0.894} \cdot 10^{-17.6256\pm0.708}. \tag{4.7}$$

This relation is obviously not statistically significant, meaning that we cannot conclude that the ratio of radio- to bolometric luminosity is in any way dependent on the Rossby number at 144 MHz.

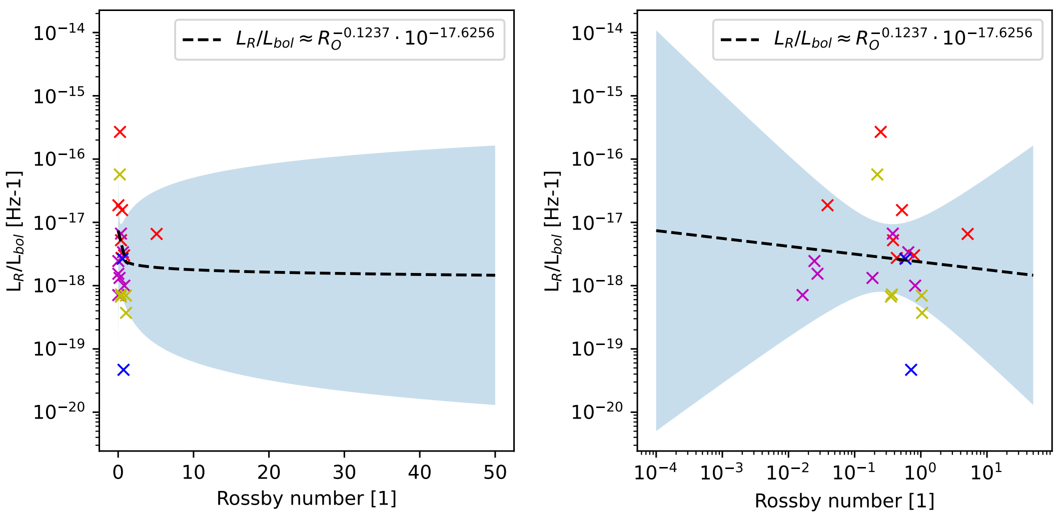

Figure 4.8: Plots of the ratio of radio- to bolometric luminosity as a function of Rossby number, the left plot in lin-log scales, and the right in log-log.

4.1.2 The GMRT 150 MHz all-Sky radio Survey (TGSS)

Fig. 4.9 contains a bar chart showing the distribution of main sequence detections across our priority categories in the GMRT 150 MHz all-Sky radio Survey (TGSS). As was the case with LoTSS, the pixel resolution of TGSS is good enough that no by-eye filtering out any false P1C1 detections were necessary, but each of the cutouts were inspected just in case. Similarly to LoTSS, the majority of our detections are here given priority 2 designations, meaning that they are detections outside of 2 beams of the expected position of the source. Because of TGSS' relatively poor resolution of 25" compared to LOFAR's 6", we can be relatively sure that these secondary detections are actually secondary sources, and not our primary source shifted outside our accepted region because of errors in its position or proper motion. In the LOFAR detections we found the number of P1C1 detections to increase towards the cooler stars, having more M dwarf detections than K dwarf detections, and more K dwarf detections than G dwarf detections etc. However, in TGSS we find the number of detections to more or less flatten out at ~ 40 detections per stellar type for G-, K- and M dwarfs. This is very unexpected, seeing as the cooler dwarfs are both more numerous and more active. A complete summary of the 151 detected main sequence stars in TGSS is given in Table 4.2.

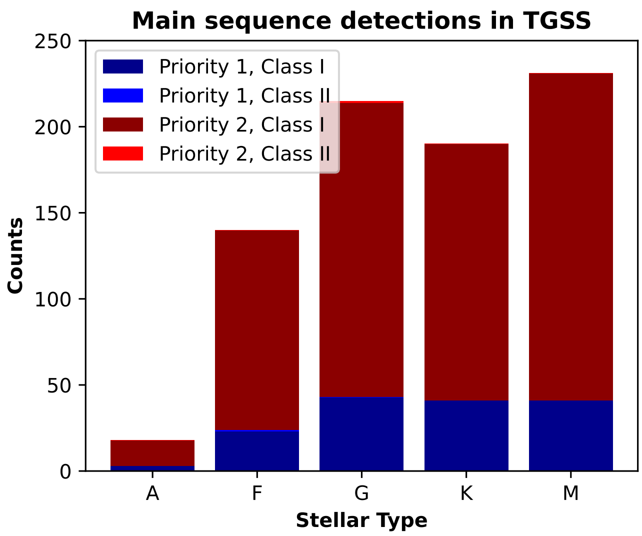

Figure 4.9: Bar chart showing the distribution of stellar detections in TGSS over stellar type.

Main sequence P1C1 detections in The GMRT 150 MHz all-Sky radio Survey (TGSS)					
SIMBAD ID	Type	RA [deg]	DEC [deg]	S_I [mJy]	Distance [pc]
HD 116798	A5	201.2282	54.8945	2436.7591	91.1990
* 31 Sgr	A3V	283.0435	-21.9238	2448.5674	79.0553
HD 115227	A2V	198.4076	72.7947	173.2917	88.4486
HD 84887	F7V	146.9277	-28.3833	74.4192	56.3984
HD 216625	F8	343.5401	19.8895	85.1017	41.8206
HD 108008	F8V	186.1371	22.1618	59.7130	97.2381
* 4 Pup	F2V	116.4969	-14.5687	42.2358	67.7494
HD 17146	F5	41.6470	43.7624	217.2381	86.7407
HD 85087	F5	147.5522	24.5594	1010.1577	54.2678
HD 109931	F0V	189.6937	-18.2529	50.3873	66.5617
HD 90530	F6V	156.6630	-32.2649	72.4649	70.3270
HD 211212	F2V	333.9009	1.9426	378.4403	98.5560
* 83 Cnc	F5	139.7531	17.7006	36.7733	42.3521
HD 37990	F7/8V	85.1897	-36.5883	99.7078	52.2229
* 38 Psc C	F8Vm-2	4.3620	8.8722	33.6983	78.8348

HD 123339	F2	211.6163	27.7231	32.9034	93.8766
HD 28579	F8	68.3305	55.4595	52.0044	73.7834
HD 223436	F8	357.3466	23.8717	273.1769	97.9254
HD 214879	F0	340.0854	51.5452	345.5583	85.5322
HD 190009	F7V	300.9450	-22.5992	116.3071	60.8464
HD 98563	F5V	170.1097	-1.8019	951.8724	84.9219
BD+11 463	F8	50.4385	12.0974	96.6614	94.1546
HD 58183	F5	112.1945	63.8699	143.7939	75.4475
HD 30411	F0	72.2288	33.9853	56.2912	98.0654
HD 57362	F4V	110.5273	29.8351	80.3340	93.1608
HD 41750	F8	92.1131	31.1999	32.7657	64.4401
HD 1252	G0	4.2504	39.7958	438.7294	66.5872
HD 24722	G6V	58.9173	-3.1278	283.1027	95.9390
HD 150687	G5/6V	250.8896	-23.2745	3607.0204	97.0804
HD 107600	G3V	185.5290	-13.4951	125.1068	66.5165
HD 69739	G3/5V	124.4287	-19.1272	48.4853	69.5983
HD 234245	G0	233.6716	49.9573	431.9205	67.3118
HD 95714	G8/K0V	165.6653	-24.2867	60.5791	69.7006
BD+37 2782	G6V	249.5553	37.1408	221.1180	64.6168
HD 17552	G5	44.6544	81.0580	127.7029	85.6574
HD 319026	G0	272.3359	-32.1110	287.4082	96.2874
HD 137510	G0IV-V	231.4797	19.4760	153.2004	43.4409
CD-45 13385	G0	295.7556	-45.0534	163.0382	98.1809
BD+33 3164	G0	279.7359	33.7451	59.4123	76.7304
BD+13 2682	G0	203.6907	12.7648	63.6057	84.3341
HD 36213	G0	82.9354	32.4542	165.6365	97.7312
HD 21916	G0	53.1219	10.7342	598.9414	82.5124
BD-08 1195	G7	84.6559	-8.9471	672.4334	81.9090
BD+23 2491	G0	191.7253	22.4845	189.9500	83.1285
HD 178486	G8/K0V	287.2671	-6.2537	387.8062	80.3415
CD-35 7097	G5	169.1267	-35.8660	195.5120	72.7391
BD+08 1988	G5	122.9165	7.7277	65.7536	94.5737
HD 168556	G3V	275.2935	-20.2912	659.8959	80.4333
HD 24045	G8V	57.3081	-17.9749	102.9519	40.0953
BD+49 1932	G0	153.5266	48.8112	44.9044	89.7498
HD 173748	G3V	281.9750	-22.1749	144.9052	78.5662
HD 89773	G	155.4821	19.7901	81.6845	89.4217
HD 197310	G0	310.4336	35.5410	194.0345	34.6339
HD 338348	G2V	292.1020	27.5175	479.8264	91.6099
HD 38665	G3V	86.6763	-18.9676	91.9606	69.1731
BD+04 3799	G0	278.8822	4.9977	445.8420	99.1586
HD 61417	G5	115.4072	49.0414	123.4211	42.5951
HD 190617	G2V	301.6454	-21.6813	153.7014	45.2913
HD 133829	G8/K0V	226.7882	-19.8188	83.2255	58.9635
HD 218602	G5	347.2895	18.4071	846.8131	94.2974
HD 240912	G5	77.1187	24.8969	58.6645	88.6778
HD 195633	G0Vw	308.1088	6.5149	38.1016	99.5865
BD+38 1222	G0	84.1779	38.5816	31.1860	96.8928
BD-11 279	G0	22.4939	-10.5677	103.4686	89.0758
BD+06 2357	G5	162.3495	5.7060	72.1580	92.8104
HD 237234	G0	63.3912	56.3017	55.4905	97.2689
HD 243312	G0	81.2555	28.9835	31.4951	73.9943
HD 80830	G8V	140.3711	-23.7891	128.8155	49.1463
BD-15 861	G5	71.6705	-14.7612	112.9176	51.9517
StKM 1-958	K4	174.6127	49.8020	90.8025	56.2942
Ross 596	K5	68.1827	34.1302	33.0835	39.9631
HD 178693	K0	287.2572	14.7781	281.2355	83.3666
CD-33 501	K6.5Vk:	20.6089	-33.2175	150.3377	27.7321
HD 155524	K2	257.7125	32.1753	182.2116	95.8537
StKM 1-296	K4	42.2795	13.4330	27.0353	76.9359
StKM 1-304	K5	42.6869	11.3266	151.6833	76.0462
BD+34 2940	K0	259.8459	34.1474	396.8945	51.8626

BD+25 162	K7V	16.1479	26.1156	140.6729	29.7927
HD 92213	K0V	159.6668	-13.7660	39.8620	46.2770
StKM 1-672	K5	119.4651	50.6574	230.4591	46.9581
BD-08 2813	K4Vk:	149.8054	-9.1883	38.3115	33.0464
BD+40 150	K2	10.9194	40.9012	653.8183	58.6648
1RXS J234334.2-192756	K7	355.9017	-19.4713	212.4225	52.7928
BD+17 541	K0	50.6450	17.7214	687.5860	41.3804
BD+20 2927	K4V	211.9773	19.9618	66.9468	77.3816
HD 44821	K0/1V(+G)	95.7493	-24.5601	297.0522	29.4271
Ross 214	K5	340.2462	64.9037	89.1154	45.8218
BD+78 374	K0	167.0585	78.1634	39.4208	74.6476
StKM 1-228	K5	30.7070	25.1045	109.3475	68.3394
G 123-53	K5V	190.4547	43.0364	133.6692	44.6603
TYC 3982-4163-1	K2V	336.3302	53.1562	50.2663	88.1162
HD 7192	K	18.1065	14.2319	662.2468	80.2852
BD+38 2239	K5	171.5842	38.2180	120.4829	77.3525
HD 170510	K2	277.3927	9.0591	37.6546	27.5760
BD+04 1936	K0	123.6051	4.1182	32.8476	79.3108
HD 284930	K0	73.1069	18.9932	126.7828	50.7182
LP 301-82	K4	62.6907	32.9300	378.6387	48.0047
StKM 1-40	K4	7.1132	-4.8762	408.8765	81.8798
BD+10 4534	K7.5V	320.6208	10.8719	317.2764	21.2140
Ross 9	K5	20.1815	57.3249	137.2538	21.7352
HD 203897	K1V	321.4944	-31.1859	275.7839	51.2338
TYC 2531-2112-1	K0V	191.7616	32.8362	70.7903	84.4706
G 67-11	K2	340.2559	18.9348	138.3583	72.7197
CD-26 5360	K3	120.2662	-26.4644	84.1987	65.9812
HD 6378	K5+Vk:	16.1108	-25.6092	100.1986	26.9811
HD 47979	K0	101.0624	53.2916	614.3884	79.1032
StKM 1-2066	K4	344.1788	-11.1753	99.4435	82.3457
BD-04 4341	K0	266.2404	-4.9547	581.4102	82.8084
HD 312478	K0	270.1837	-17.9650	214.9565	88.7751
HD 169604	K0V	276.5791	-21.4771	57.5848	63.3963
2MASS J20363026-3131224	M6.0	309.1353	-31.5261	78.1403	34.8773
2MASS J08281014+2533435	M9V	127.0519	25.5598	66.8510	89.4118
G 63-45	M3.5	204.8264	15.6745	31.9556	30.5396
2MASS J10595340+4201329	M8V	164.9843	42.0228	36.5101	53.6109
PM J18490+1230	M1.6	282.2660	12.5025	105.5815	63.5965
LSPM J2131+5601	M3.9	322.9687	56.0299	76.2687	84.0743
[PS78] 146	M3	18.2242	-22.3476	134.0099	59.5684
LP 649-28	M4.5V	30.7142	-5.5294	38.0935	57.4587
2MASS J20025265-1316418	M8.5	300.7298	-13.2811	217.5836	63.6408
G 226-67	M3.2	265.1934	56.6802	321.5825	51.0368
2MASS J12264892+1744021	M9V	186.7137	17.7289	36.3017	76.1958
LSPM J1145+2558	M2.8	176.3712	25.9660	25.0707	38.7112
2MASS J08404809+2024121	M8V	130.2110	20.3997	16.2899	92.5084
2MASS J15472702+0741342	M7V	236.8707	7.6903	41.5764	72.6709
LSPM J1417+4124	M3.0	214.3420	41.4029	141.3646	37.1268
2MASS J16030492+3851438	M7V	240.7818	38.8593	423.5423	94.6111
MGC 28950	M2.6	181.6213	0.0343	41.2925	90.1856
SDSS J123515.40+663006.2	M7	188.8337	66.4980	248.4174	76.2700
2MASS J10435088+0929353	M6V	160.9712	9.4900	171.7221	91.5987
SDSS J161144.49+123553.9	M8	242.9439	12.5954	30.9729	94.0145
LSPM J1239+1341	M6	189.8777	13.6918	567.0461	47.2268
V* DS Cnc	M4	131.3145	17.7211	374.3056	77.8648
LP 90-36	M0V	131.8239	59.5473	197.3946	37.1479
PM J03466+8207	M1.0V	56.7259	82.1261	442.7981	41.3600
LSPM J1045+3954	M2.5	161.3680	39.9105	193.0397	63.4512
LSPM J1227+5705	M2.7	186.8192	57.0925	16.7213	44.9042
LSPM J1225+4552E	M3.3	186.5044	45.8629	919.2511	77.4554
2MASS J01314609-1013374	M7V	22.9503	-10.2307	147.1035	82.3571
G 67-50	M3	347.8426	19.6893	430.6474	52.4518

2MASS J11560723+1509502	M8V	179.0380	15.1602	155.2468	55.6978
UCAC4 356-002031	M1.1	26.5145	-18.9924	1190.6012	87.0215
G 196-12	M3.4	153.1297	48.3590	141.4268	61.7620
LAMOST J070352.99+172452.2	M5	105.9807	17.4094	44.5180	38.0394
LSPM J1848+6135	M2.0V	282.2125	61.5810	87.6875	23.8739
V* V1252 Cen	M2Ve	188.7774	-41.6132	51.0849	57.4831
LP 650-181	M1.5Ve	38.0931	-6.0442	58.8779	60.7176
G 40-16	M2.5V	124.3895	20.9947	169.8636	31.2375
PM J15390+2931	M2.4	234.7827	29.5249	23.7321	42.3123
SDSS J113240.92+494055.4	M7	173.1830	49.6791	64.8942	71.1856
2MASS J08385719+1825330	M9V	129.7472	18.4227	55.2742	47.5978
2MASS J16173107+5140224	M8V	244.3929	51.6693	379.2854	59.6770

Table 4.2: Table of P1C1 detections in TGSS.

The measured fluxes in Table 4.2 all seem incredibly large, some stars having fluxes in the Jansky scale. This is also unexpected, seeing as the highest measured fluxes in LoTSS were on the tens of milli-Janskys scale, two orders of magnitude lower, and only 6 MHz separates the two surveys. Actually, this two order of magnitude difference between the two surveys is something that comes up frequently in the following analysis, the implications of which we explore further in Section 5.6. As we did for the LOFAR data we plot the measured brightness temperature as a function of effective temperature, which is shown in Fig. 4.10. As in LoTSS we here find the brightness temperatures to decrease as effective temperature increases, the M dwarfs once again found to be the brightest at 150 MHz. A first order fit is performed on the logarithms of the values, yielding the following relation between brightness- and effective temperature:

$$T_B \approx T_{\text{eff}}^{-3.3069\pm1.563} \cdot 10^{27.0682\pm5.763}, \tag{4.8}$$

where the uncertainties correspond to the 3σ level, meaning that the relation is once again significant. It is immediately obvious that the brightness temperatures are here much larger than those computed from the LoTSS data, and this coincides with the abnormally large measured fluxes. This mysterious difference between the LoTSS and TGSS surveys is explored further in Section 5.6. Nevertheless, we observe a very large spread in our data points, both above and below our fitted function, but some points are still very clear outliers. Interestingly, we have a group of five M dwarfs with effective temperatures around 3000 K that all have brightness temperatures about one order of magnitude higher than their on-function counterparts with very similar effective temperatures. We also observe one G type star to be much brighter than the other stars of type G. K. We also surprisingly detect two A type stars, both very bright and much brighter than the fitted function would suggest.

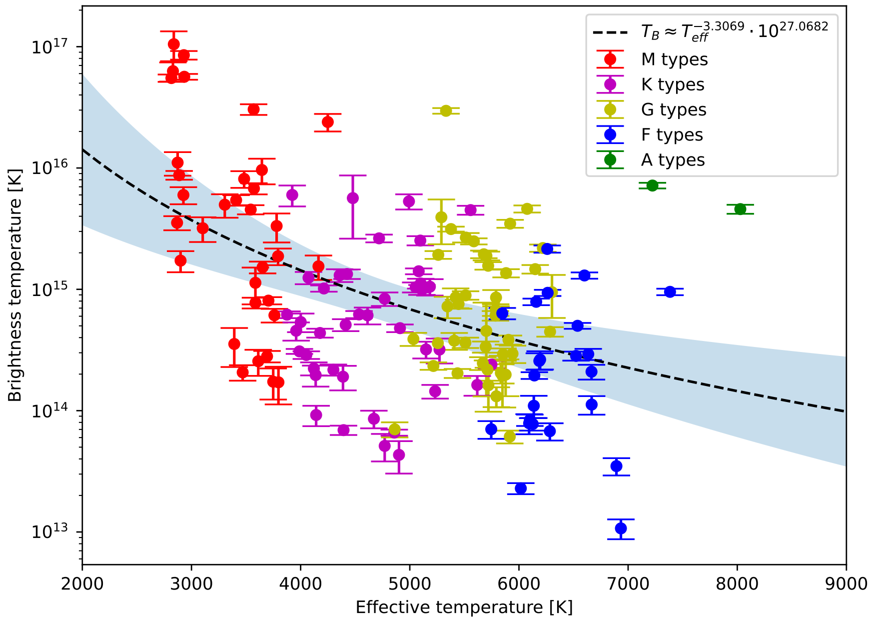

Figure 4.10: Brightness temperature versus effective temperature for the sources we detect in TGSS. A first order polynomial fit is done on log(TB) vs log(Teff), indicated by the dashed black line.

Similarly we plot the stars' radii against brightness temperature in Fig. 4.11, as before finding a trend where brightness temperature decreases as the stellar radius increases. Similarly to in Fig. 4.10 we find a group of five M dwarfs that are significantly brighter than their similarly sized counterparts. The significantly brighter G type compared to other G types is also here observed. The A types here overlap significantly with the F types in radius, but are not found to be significantly brighter than their similarly sized F type stars. As previously we here find several stars that have nonsensical radii, for example we find a G type star with a radius of 2 $R_\odot$ and one with 1.6 $R_\odot$. If this is a fault of our code, letting in giants into our sample or simply wrongly classified stars is discussed further in Section 5.1. As before we here perform a first-order fit on the logarithmic values, yielding the relation;

$$T_B \approx R_*^{-1.3962\pm0.537} \cdot 10^{14.7712\pm0.168}, \quad (4.9)$$

with uncertainties corresponding to the 3σ level. The relation is found to be statistically significant, and very similar to the fitted function to the same properties using the detections in LoTSS, except that the exponent of 10 is about two orders of magnitudes greater in TGSS.

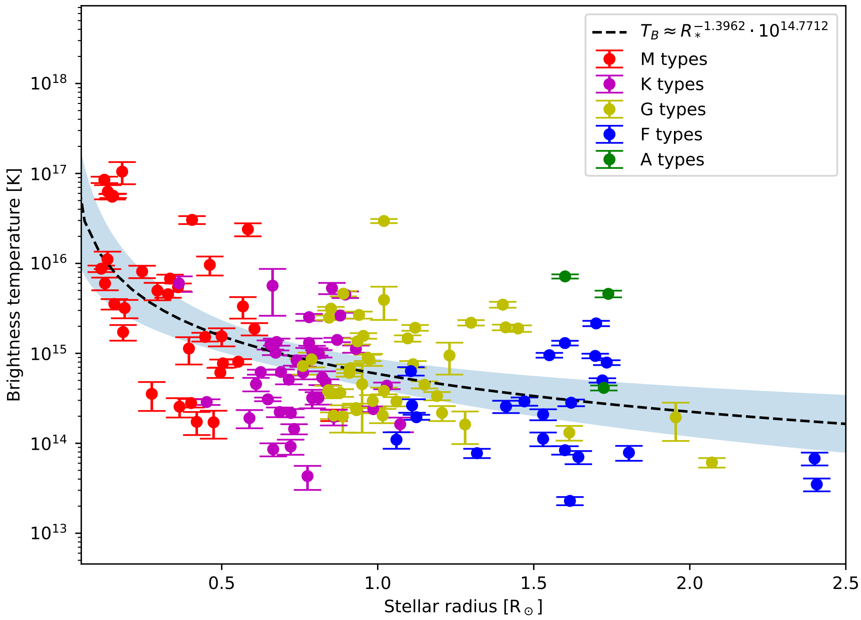

Figure 4.11: Brightness temperature versus stellar radius for the sources we detect in TGSS. A first order polynomial fit is done on $\log(T_\mathrm{b})$ vs $\log(R)$, indicated by the dashed black line.

Similarly to what we did for the LoTSS data we also try to relate brightness temperature to rotation period, but as not all stars have reported rotational periods, the resulting first order fit on the logarithmic values is found to be bad, with a large 3σ interval. The plot of brightness temperature against rotational period is found in Fig. 4.12, with a first order log-log fit shown as a dashed black line. As in LoTSS the first-order fit is found to be bad and non-significant, the yielded relation with 3σ uncertainties being;

$$T_B \approx P_\mathrm{rot}^{-0.0486\pm0.459} \cdot 10^{14.5412\pm0.480}. \tag{4.10}$$

As dealing with brightness temperatures at frequencies where most of the incoming radiation is coherent and non-thermal can be a bit counter-intuitive we also explore the relations between the ratio of radio- to bolometric luminosity and the same stellar parameters. A plot of the radio luminosity ratio against effective temperature is shown in Fig. 4.13, the left plot with a lin-log scale and the right with a log-log scale. As in LoTSS, we here see a clear relation between a star's luminosity at 150 MHz and its effective temperature. As before we have a lot of spread in our data, and all stellar types (except A) are found to have a large spread of radio luminosity ratios, in some cases spanning two orders of magnitude. Still, a clear trend is found and given as:

$$L_R/L_\mathrm{bol} \approx T_\mathrm{eff}^{-7.1397\pm1.395} \cdot 10^{11.0965\pm5.145}, \tag{4.11}$$

where the given uncertainties correspond to the 3σ level.

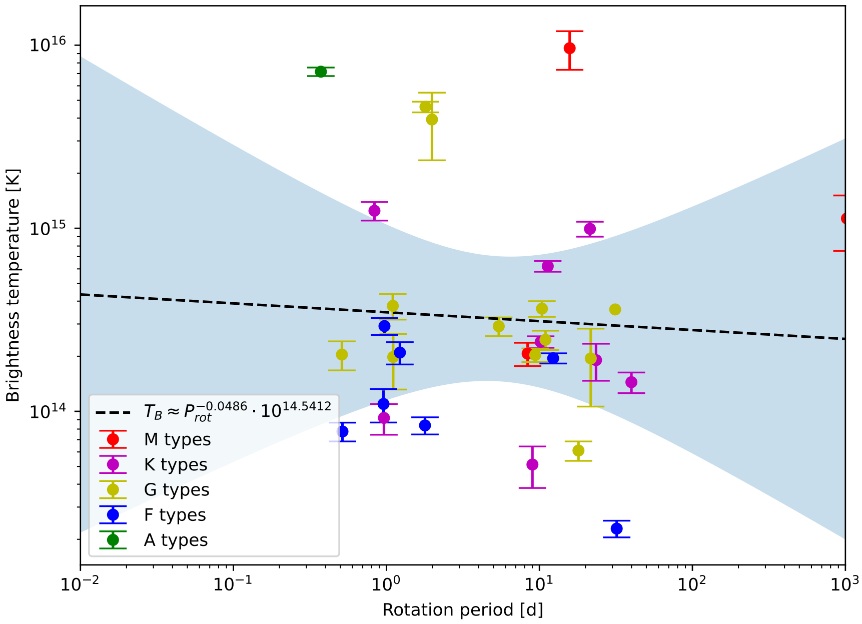

Figure 4.12: Brightness temperature versus rotational period for the sources we detect in TGSS. A first order polynomial fit is done on $\log(T_{\rm b})$ vs $\log(P_{\rm rot})$, indicated by the dashed black line.

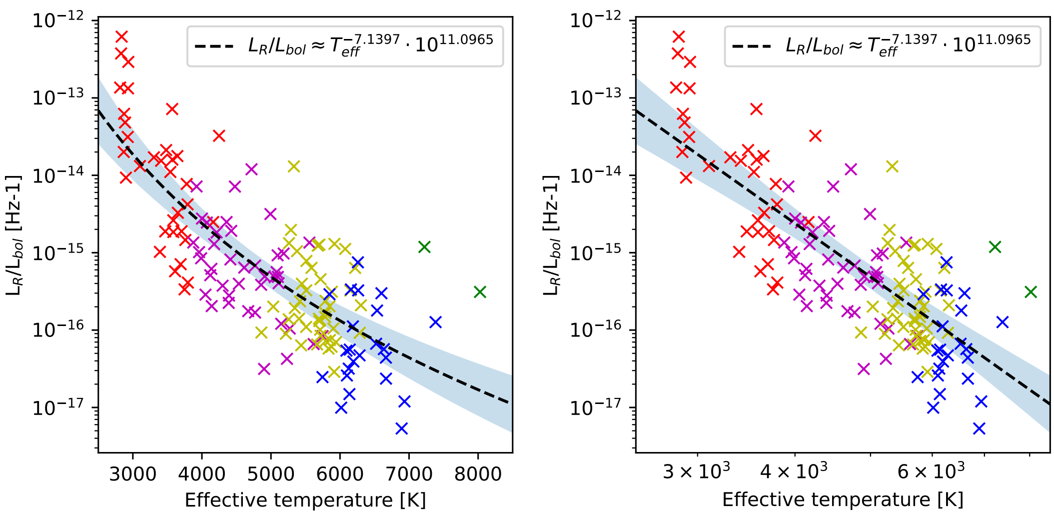

Figure 4.13: Plots of the ratio of radio- to bolometric luminosity against effective temperature, the left on a lin-log scale, and the right on a log-log scale. A black dashed line with 3σ limits is used to indicate the first-order fit.

Similarly we plot the ratio of radio- to bolometric luminosity against stellar radius, as shown in Fig. 4.14. As before a first-order fit is performed on the logarithmic values, yielding the following relation:

$$L_R/L_{\rm bol} \approx R_*^{-2.3034\pm0.519} \cdot 10^{-15.4369\pm0.174}. \tag{4.12}$$

As in Fig. 4.11 we here find that the smaller stars are generally brighter in radio, a small M dwarf of radius ~ 0.1 $R_\odot$ having a radio luminosity fraction two orders of magnitude greater than a Sun-like star of radius ~ 1 $R_\odot$.

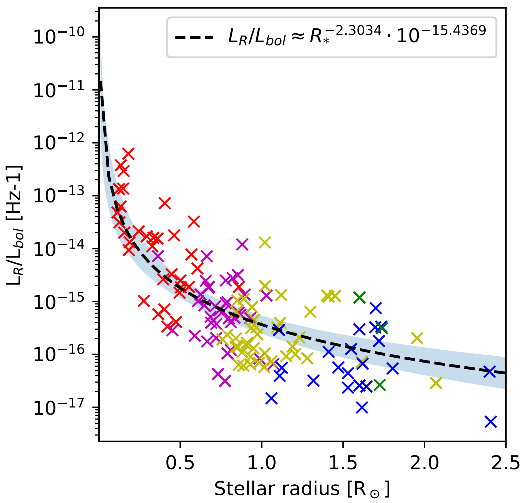

Figure 4.14: Plots of the ratio of radio- to bolometric luminosity against stellar radius, the left on a lin-log scale, and the right on a log-log scale. A black dashed line with 3σ limits is used to indicate the first-order fit.

Finally we try to relate the ratio of radio- to bolometric luminosity to the activity indicators; rotational period and Rossby number. Unfortunately, as many of our stars don't have reported periods in Vizier, the plots of these relations are once again sparse, meaning that fitting a meaningful trend to our data becomes nearly impossible. The plot of radio luminosity ratio against rotational period is shown in Fig. 4.15, and against Rossby number in Fig. 4.16. In both cases, the ratio of radio- to bolometric luminosity appears to be relatively flat across both periods and Rossby numbers, although a slight decrease towards longer rotation period and higher Rossby numbers can be seen. However, our sample of stars with reported periods and computed Rossby numbers is simply too small to draw any certain conclusions. We do perfmorm first-order fits on the two sets of log-log values, yielding the following insignificant relations;

$$L_R/L_{\mathrm{bol}} \approx P_{\mathrm{rot}}^{-0.0276\pm0.657} \cdot 10^{-15.8040\pm0.597}, \tag{4.13}$$

$$L_R/L_{\mathrm{bol}} \approx R_O^{-01055\pm0.624} \cdot 10^{-15.8671\pm0.651}. \tag{4.14}$$

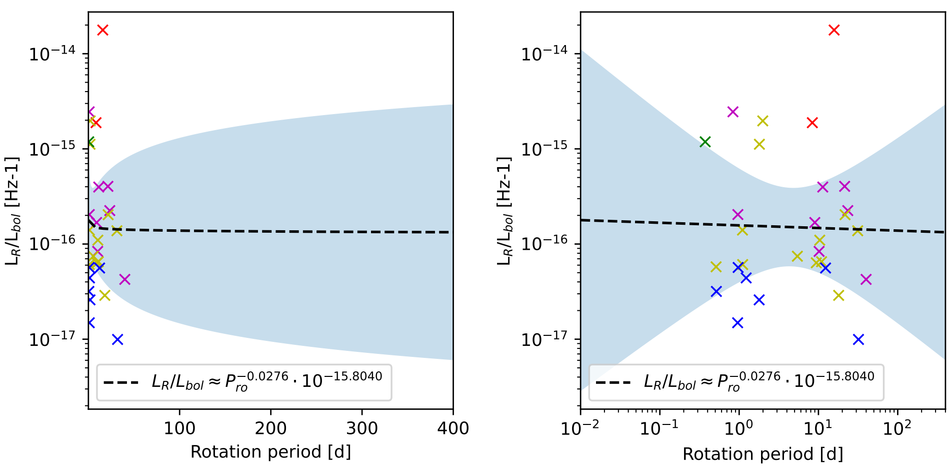

Figure 4.15: Plots of the ratio of radio- to bolometric luminosity against rotation periods, the left on a lin-log scale, and the right on a log-log scale. A black dashed line with 3σ limits is used to indicate the first-order fit.

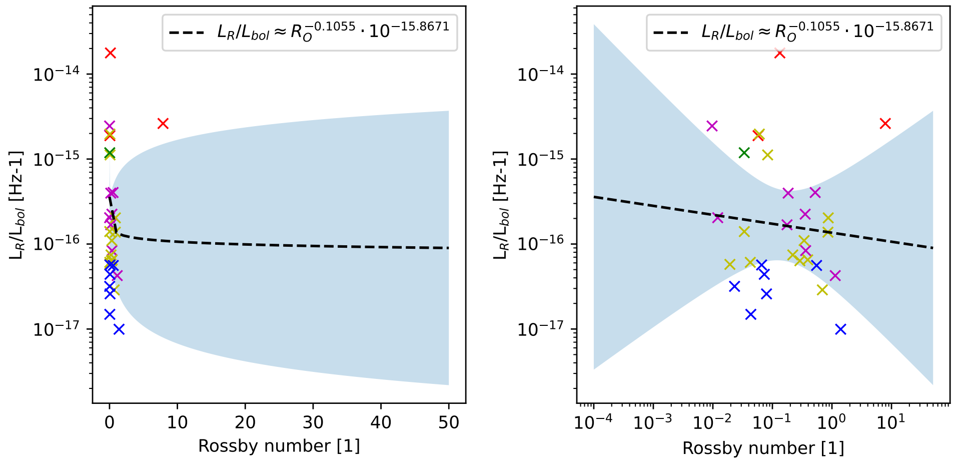

Figure 4.16: Plots of the ratio of radio- to bolometric luminosity against Rossby numbers, the left on a lin-log scale, and the right on a log-log scale. A black dashed line with 3σ limits is used to indicate the first-order fit.

4.1.3 Rapid ASKAP Continuum Survey

Fig. 4.17 contains a bar chart showing the distribution of main sequence detections across our priority categories in the Rapid ASKAP Continuum Survey (RACS). As was the case with both LoTSS and TGSS, the pixel resolution of RACS is good enough that no by-eye filtering out any false P1C1 detections was necessary. As in the two previous surveys the majority of our detections are so-called secondary detections, which are given a priority 2 designation. As in TGSS we here find the number of priority 1 class I detections to not increase towards M dwarfs, which one would expect because how numerous and active M dwarfs are. Instead we here detect the most F dwarfs, closely followed by G dwarfs, with the M dwarfs being the third most detection stellar type. A complete summary of the 124 detected main sequence stars in RACS is given in Table 4.3.

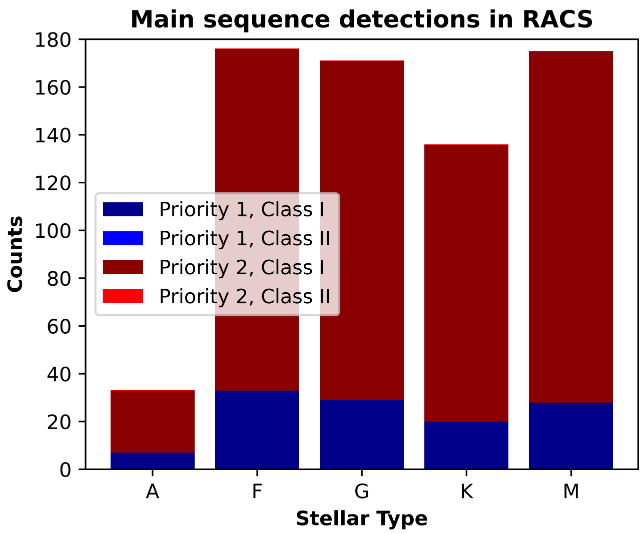

Figure 4.17: Bar chart showing the distribution of stellar detections in TGSS over stellar type.

Main sequence P1C1 detections in RACS					
SIMBAD ID	Type	RA [deg]	DEC [deg]	S_I [mJy]	Distance [pc]
* b01 Hya	A3V	161.7266	-17.3010	249.2441	56.1814
HD 79765	A3	139.1228	18.8069	2.7559	71.2883
HD 90211	A0/1	156.2212	-0.4066	2.7848	73.5516
* 31 Sgr	A3V	283.0446	-21.9241	531.6550	79.0553
HD 188097	A1mA5-F2	299.6933	-69.1700	14.3133	69.2828
HD 110261	F2V	190.2184	3.8645	4.0916	82.6668
HD 137515	F5V	231.9956	-39.5347	2.5901	88.8764
HD 111545	F5V	192.5314	-7.6367	15.6876	48.6033
HD 125752	F5	215.3374	10.8322	7.8469	72.0497
* 83 Cnc	F5	139.7537	17.7002	9.5263	42.3521
HD 29445	F6V	69.2675	-28.9575	61.3283	97.3925
HD 223436	F8	357.3471	23.8711	43.4284	97.9254
HD 139327	F0V	234.5098	-14.5345	3.9344	88.9152
HD 210944	F5V	333.3181	27.3148	4.8311	66.3409
HD 126375	F6V	216.7662	-57.2927	1.9316	70.3113
HD 190009	F7V	300.9453	-22.6000	48.0500	60.8464
HD 1466	F8V	4.6306	-63.4808	1.2304	42.8164
HD 93638	F5V	162.1445	-3.2598	7.1037	80.9972
HD 48332	F3/5V	100.7062	-4.1448	3.5391	78.2173
HD 95230	G5(V)	164.5851	-64.4803	1.5171	74.3520
HD 173197	G8V	281.0298	3.3038	5.7449	50.3364
CD-40 5290	G0	143.1571	-41.4047	63.7880	91.5520
HD 326583	G0	254.4579	-43.8048	9.4918	98.9451
HD 317107	G5	271.8613	-29.6245	4.7958	94.3962
BD+26 1630	G5	115.7123	25.9700	5.2884	55.8764
HD 89773	G	155.4828	19.7894	23.3520	89.4217
HD 139056	G1/2V	234.0131	0.2643	3.6618	93.1426
HD 198675	G3/5V	313.4779	-49.4540	11.3947	89.6855
HD 286561	G0	62.4191	11.4639	4.0110	87.5603
HD 136130	G6V	230.6338	-64.1313	2.6210	92.3900
V* BP Ind	G8/K0V	312.6949	-56.2467	1.7244	45.2287
HD 24702	G0	59.1301	22.6673	4.4393	46.8520
HD 188264	G5	298.4592	13.9780	1.8854	93.6572
HD 113970	G3V	196.8600	-12.6746	11.5739	99.3802
HD 10430	G8V	25.3390	-19.9431	1.7283	54.3709
BD+23 55	K2	6.5997	23.8939	13.1103	56.6229
HD 162598	K6V	268.0790	-7.5610	5.2369	30.6516
MCC 351	K7V	2.1234	17.4207	42.2482	21.7436
HD 197823	K0IV-V	311.8311	-35.1585	2.3139	37.0397
BD-16 931	K2V	70.9099	-15.8096	5.4453	48.8370
G 16-34	K3	243.0553	5.4834	13.7185	88.6341
HD 6378	K5+Vk:	16.1112	-25.6098	23.7594	26.9811
2MASS J02013550-1609538	K5	30.4085	-16.1695	7.3359	72.6459
BD-04 4341	K0	266.2408	-4.9551	115.1676	82.8084
2MASS J21534698+1157479	M7	328.4557	11.9591	3.2357	52.1667
LP 732-30	M4.5V	172.2404	-15.9434	20.4731	44.1612
BPM 33365	M2	124.5392	-48.2916	3.3731	52.2727
LSPM J0253+0024	M6V	43.3970	0.4092	10.5471	57.1665
LEHPM 694	M4.5	7.9484	-29.4876	10.1293	42.7734
LP 785-18	M3V	129.0854	-19.3490	11.4043	42.2600
LP 928-42	M3.0	315.0259	-28.8688	2.3270	32.7581
LP 374-30	M6.6	170.2950	21.4365	4.6719	26.1914
2MASS J18151564-4927472	M3	273.8306	-49.4669	11.9879	61.9850
L 886-20	M3.5V	102.7563	-9.1889	3.1865	24.3920
LP 569-16	M4.0V	273.3973	5.5302	4.2411	29.3754
LSPM J2347+2544	M2.89	356.9918	25.7360	0.8835	38.5395
G 40-16	M2.5V	124.3896	20.9945	48.9036	31.2375

Table 4.3: Table of P1C1 detections in RACS.

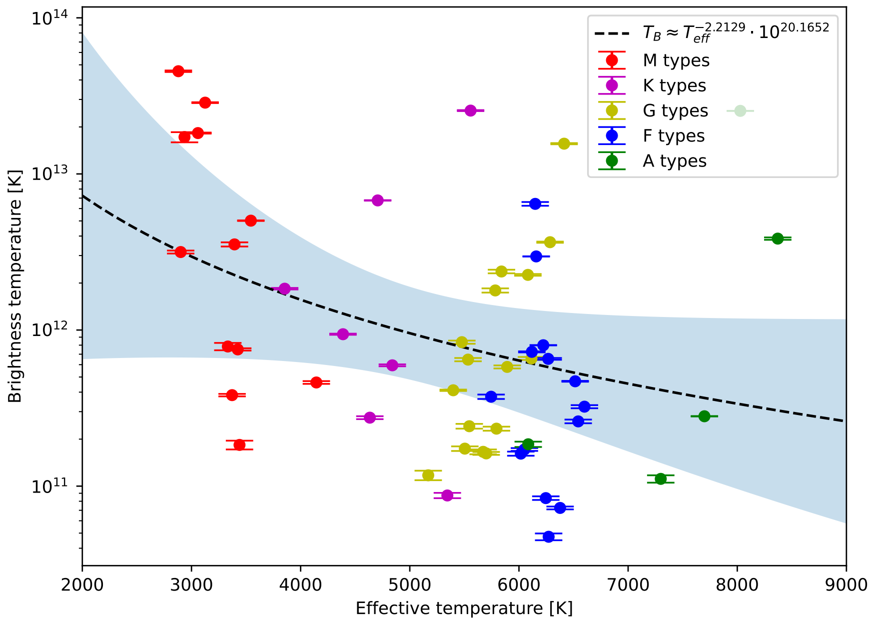

Figure 4.18: Brightness temperature versus effective temperature for the sources we detect in RACS. A first order polynomial fit is done on log(TB) vs log(Teff), indicated by the dashed black line.

As we did with the samples from the previous surveys we try to relate the computed brightness temperatures of our sample at the RACS frequency of 887.5 MHz to the stars' effective temperatures, a plot of which is shown in Fig. 4.18. Similarly to our previous attempts at relating these two properties, we here find that cooler stars generally have higher brightness temperatures, although the spread in brightness temperature seems to be larger in RACS compared to the previous surveys. For example, we report G type stars with brightness temperatures ranging from $\sim 10^{11}$ K to $\sim 10^{13}$ K, a difference of two orders of magnitude. The same large spread is found for the other stellar types as well, even the A types, although the sample of detected A stars is very limited. As before, we find a group of M dwarfs that are significantly brighter than their similarly cool counterparts, but interestingly we here have a K-, G- and A type star with very similar brightness temperatures to these M dwarfs. As before we perform a first-order fit to the log-log values, yielding the following function:

$$T_B = T_{\text{eff}}^{-2.2129 \pm 2.43} \cdot 10^{20.1652 \pm 9.036}, \tag{4.15}$$

where the uncertainties correspond to the 3σ level. We here find that the relation between brightness temperature and effective temperature is statistically insignificant, likely due to the previously mentioned large spread in our RACS data, the causes of which are unknown.

A plot of brightness temperature against stellar radius is shown in Fig. 4.19, also with first-order fitted trend. As in the previous surveys, we also here find the larger stars to generally be less bright at 887.5 MHz, but as in Fig. 4.18 there is a large spread in our data. Exactly as for the T_B versus T_{eff} plot, we here see the same outlying K-, G- and A type with similar brightness temperatures as the brightest M dwarfs, all potentially interesting targets for further research. A fit is again performed on the log-log values, yielding the relation:

$$T_B = R_*^{-1.2177 \pm 0.9} \cdot 10^{11.8593 \pm 0.297}, \tag{4.16}$$

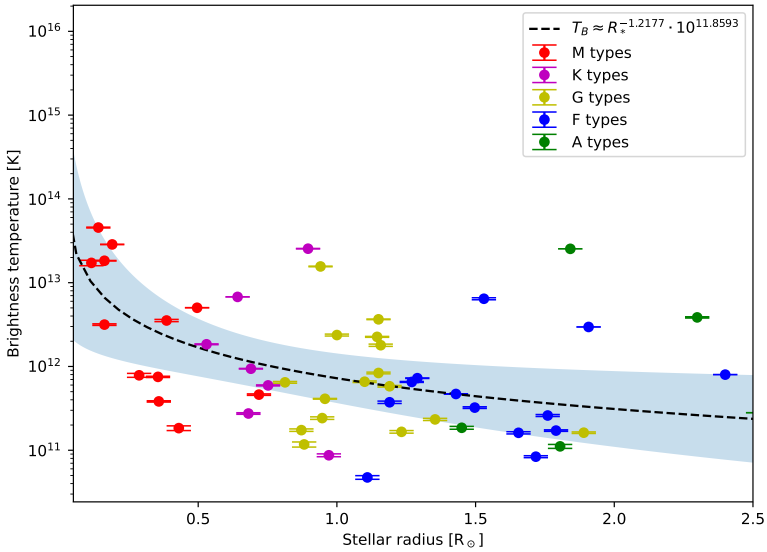

Figure 4.19: Brightness temperature versus stellar radius for the sources we detect in RACS. A first order polynomial fit is done on log(TB) vs log(R), indicated by the dashed black line.

which is found to be statistically significant. Similarly, we plot brightness temperature against rotation period, as shown in Fig. 4.20. As before we have very few stars with reported rotation periods, so one must be careful not to interpret the fitted trend as certain. However, RACS is the first survey to show any sign of increase in brightness temperature as the rotation period increases. Performing a first-order fit on the logarithmic values yields the following relation:

$$T_B = P_{\text{rot}}^{0.2616 \pm 0.498} \cdot 10^{11.0579 \pm 0.297}, \tag{4.17}$$

which is statistically insignificant. One can therefore not interpret the apparent increase in T_B as P_{rot} increases as true, as the 3σ range of its slope also covers decreasing functions. As all other surveys show that brightness temperature generally decrease as rotation period increases, we expect this to be the case, as rapidly rotating stars are also thought to be more active.

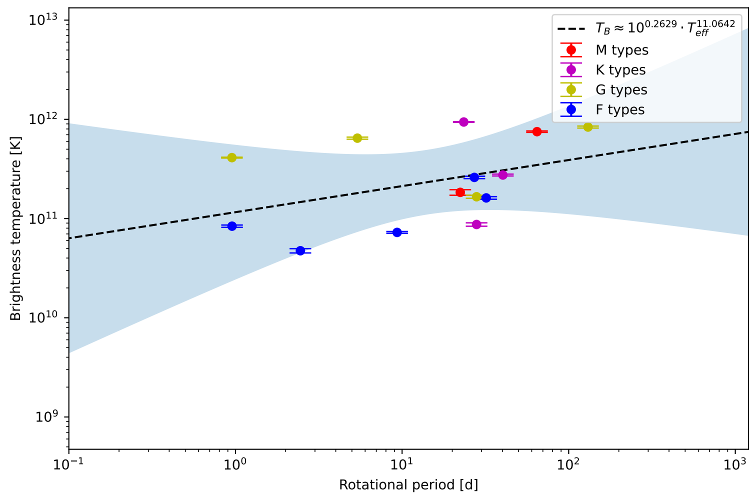

Figure 4.20: Brightness temperature versus period for the sources detected in RACS. A first order polynomial fit is done on $\log(T_B)$ vs $\log(P_{\text{rot}})$, indicated by the dashed black line.

Plots of the ratio of radio- to bolometric luminosity against effective temperatures are found in Fig. 4.21. Similarly to our plot of brightness temperature against effective temperature, we here find that hotter stars are generally less luminous at RACS' frequency of 887.5 MHz. A first order fit is performed on the logarithmic values, yielding the following relation:

$$L_R/L_{\rm bol} \approx T_{\rm eff}^{-5.5271\pm2.754} \cdot 10^{3.7497\pm10.221}. \tag{4.18}$$

In contrast to our fit relating T_B to $T_{\rm eff}$, this relation is statistically significant, showing within 3σ confidence that an increase in effective temperature is associated with a decrease in the ratio of radio- to bolometric luminosity. Similarly we try to relate the radio luminosity ratio to stellar radius, plots of which are shown in Fig. 4.22. A first-order fit is performed on the log-log values, and yields the relation:

$$L_R/L_{\rm bol} \approx R_*^{-2.4040\pm0.813} \cdot 10^{-16.8566\pm0.273}, \tag{4.19}$$

which is also statistically significant.

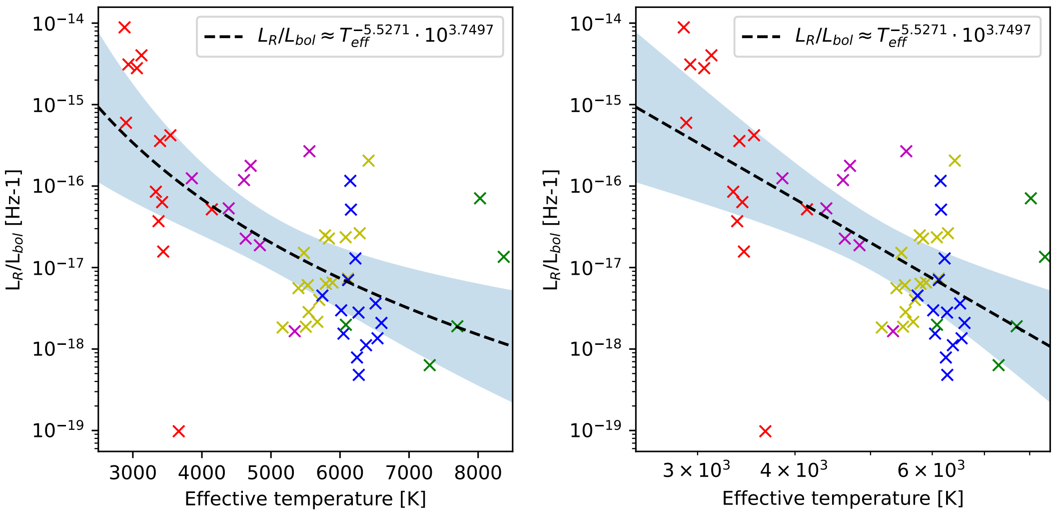

Figure 4.21: The ratio of radio- to bolometric luminosity versus effective temperature for the sources detected in RACS. A first order fit on the log-log values is shown as a black dashed lines with blue indicating the fit's 3σ confidence interval.

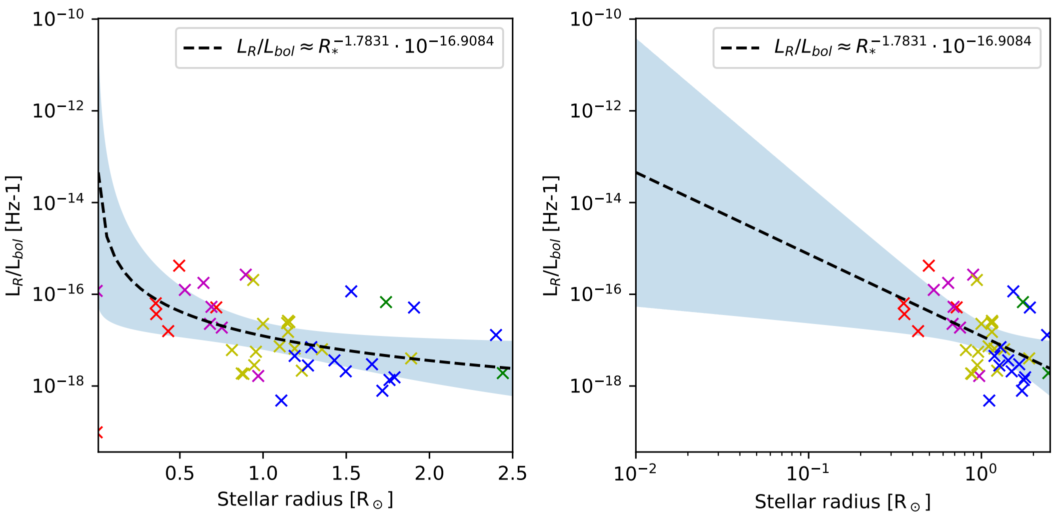

Figure 4.22: Same as Fig. 4.21, but plotted against stellar radius.

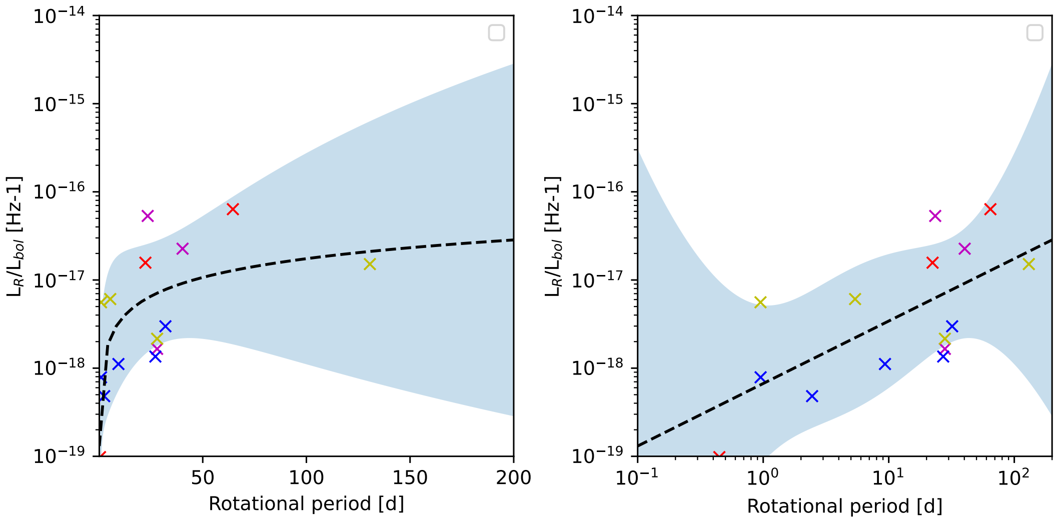

Figure 4.23: Same as Fig. 4.21, but plotted against rotation period.

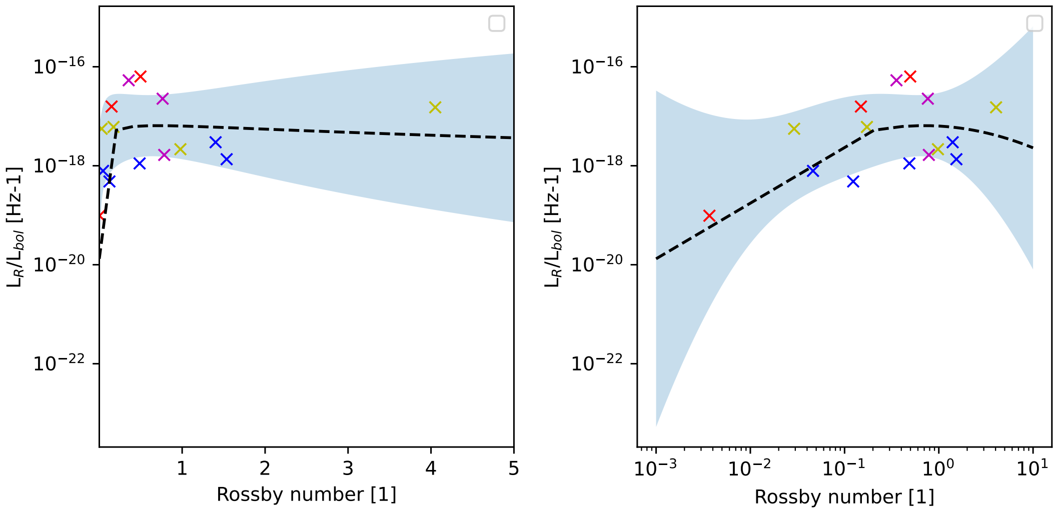

Figure 4.24: Same as Fig. 4.21, but plotted against Rossby number.

Finally we attempt to relate the ratio of radio- to bolometric luminosity to the activity indicators rotation period and Rossby number. Plots of the radio luminosity ratio against rotation period are found in Fig. 4.23. Also here we see an apparent increase in the radio luminosity ratio as rotation period increase, the opposite of what we would expect. A relation is again fitted to the log-log values, yielding the relation:

$$L_R/L_{\mathrm{bol}} \approx P_{\mathrm{rot}}^{0.7001\pm0.645} \cdot 10^{-18.1899\pm0.819}. \tag{4.20}$$

Surprisingly the slope of this relation is statistically significantly different from zero and positive, meaning that the apparent increase in L_R/L_{bol} as P_{rot} increases is statistically significant. RACS is the only survey where this trend is found. Finally we relate the radio- to bolometric luminosity ratio to the Rossby number, plots of which are shown in Fig. 4.24. Also here an apparent slight increase in L_R/L_{bol} as rossby number increases is observed, although not as steep as in Fig. 4.23. A first-order relation is fitted, yielding the relation:

$$L_R/L_{\mathrm{bol}} \approx R_O^{0.4594\pm0.717} \cdot 10^{-17.215\pm0.645}, \tag{4.21}$$

which is not statistically significant, meaning that there is a possibility that L_R/L_{bol} is completely independent of the Rossby number.

4.1.4 VLA FIRST

Fig. 4.25 contains bar charts showing the distributions of main sequence detections in the VLA FIRST survey both before and after obviously false detections are filtered out. We detect very few AFGKM stars in FIRST compared to VLASS, with only 11 main sequence (or transition to sub-giant) stars being designated as a P1C1 detection compared to the 103 in VLASS. However, as FIRST has a much smaller field-of-view this is not immediately concerning. Fig. 4.25 shows that the majority of our detections are of M dwarf stars, but surprisingly no K dwarfs are given a P1C1 designation in VLA FIRST, the second most commonly detected stellar type in VLASS (see Fig. 4.30). Every single main sequence star given a P1C1 designation is shown in Table 4.4.

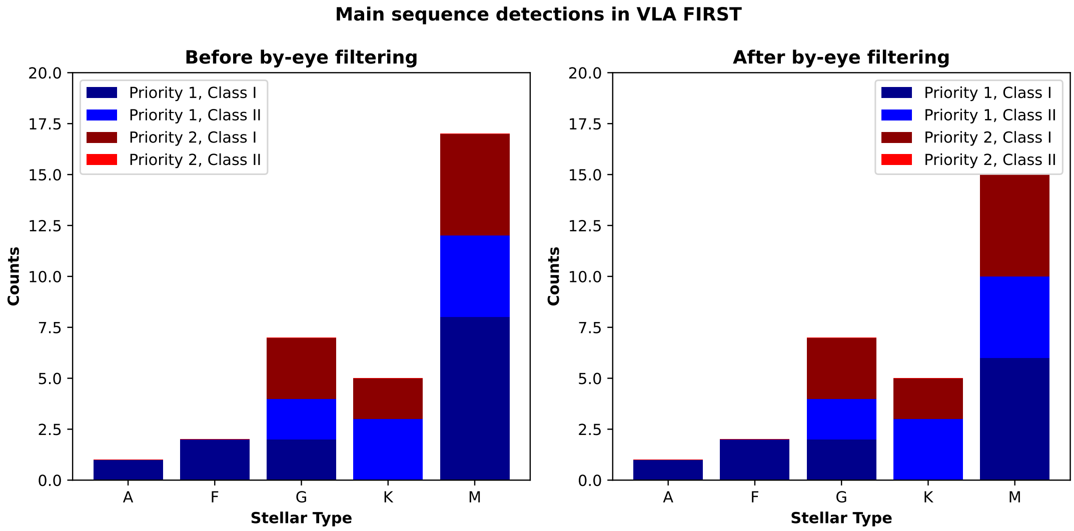

Figure 4.25: The distribution of detections across stellar types both before and after by-eye filtering out obvious non-detections.

Main sequence P1C1 detections in VLA FIRST					
SIMBAD ID	Type	RA [deg]	DEC [deg]	S_I [mJy]	Distance [pc]
V* BU Psc	A9V/IV	0.5174	-2.7618	14.0905	63.9036
HD 151651	F5	251.6056	47.5475	1.6684	63.1523
HD 125858	F5	215.2766	38.9916	5.2734	82.2106
HD 71558	G5V	127.0516	0.9030	0.3597	63.7491
HD 138573	G5IV-V	233.1880	10.9722	0.6620	30.1774
2MASS J13582164-0046262	M5.5	209.5964	-0.7700	0.5928	45.9003
G 226-67	M3.2	265.1874	56.6895	54.4367	51.0368
MGC 29282	M3.5	181.8199	-0.2163	0.5556	56.0188
V* RY Sex	M4V	159.0113	5.1245	0.5733	15.2740
2MASS J16104135+5047114	M4.2	242.6785	50.7907	3.5991	84.2151
1RXS J001650.6-071013	M0	4.2148	-7.1668	0.5134	71.3826

Table 4.4: Table of P1C1 detections in VLA FIRST.

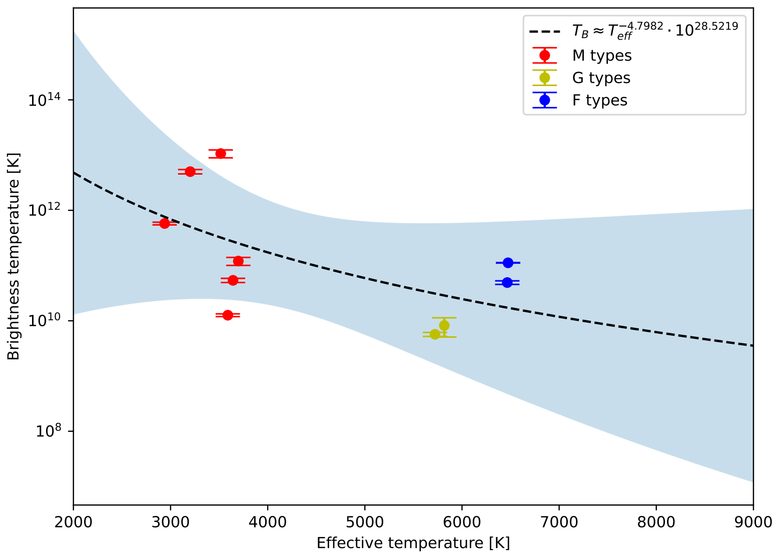

Figure 4.26: Brightness temperature versus effective temperature for the sources we detect in FIRST. A first order polynomial fit is done on log(T_B) vs log(T_{eff}), indicated by the dashed black line.

As our sample of detected stars in VLA FIRST is that much smaller than the samples from the other surveys, any trends in plots of observational properties against stellar properties will also be harder to find. Firstly, we attempt to relate brightness temperature to effective temperature, a plot of which is shown in Fig. 4.26. As before, as we only have one A type detection, we are not able to query its properties using VASE, and it is therefore not plotted. A first-order fit on the logarithms of brightness- and effective temperature is performed, yielding the following relation:

$$T_B \approx T_{\text{eff}}^{-4.7982\pm7.197} \cdot 10^{28.5219\pm26.178}, \tag{4.22}$$

where the uncertainties correspond to the 3σ level. It is here found that the slope of the fitted relation is insignificant to the 3σ level, which means that we can not conclude that there is a relation between a star's radio brightness and its effective temperature only using our VLA FIRST samples. However, as all other surveys show significant relations between brightness temperature and effective temperature it is still safe to say that there is some relation between the two. Similarly we plot brightness temperature against stellar radius, which is shown in Fig. 4.27. Also here we attempt to fit a relation to our data, which in this case also yields a statistically insignificant relation:

$$T_B \approx R_*^{-1.7950\pm2.652} \cdot 10^{10.6431\pm1.119}. \tag{4.23}$$

Unfortunately only two of our detected stars in VLA FIRST have reported rotation periods, so we here skip trying to relate brightness temperature to period, as no meaningful relation can be determined from two points only.

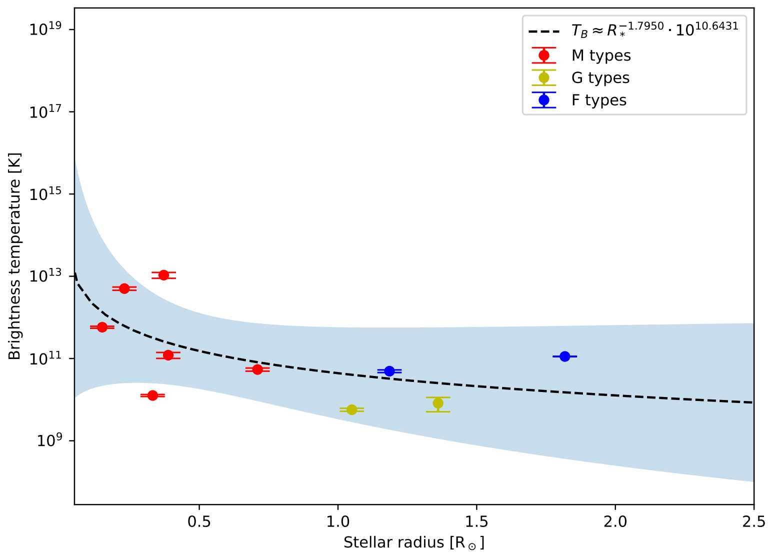

Figure 4.27: Brightness temperature versus stellar radius for the sources we detect in FIRST. A first order polynomial fit is done on log(TB) vs log(R), indicated by the dashed black line.

As for the previous surveys we also here attempt to relate the ratio of radio- to bolometric luminosity to some stellar parameters, beginning with effective temperature. Plots of the radio luminosity ratio against effective temperature are shown in Fig. 4.28, both on lin-log and log-log scales. As before we fit a relation to our data, yielding the now statistically significant relation;

$$L_R/L_{\text{bol}} \approx T_{\text{eff}}^{-8.633\pm6.702} \cdot 10^{14.5262\pm24.372}. \tag{4.24}$$

Although the 3σ uncertainties are relatively large, the slope is statistically different from zero, meaning that we have a more-or-less guaranteed relationship between the ratio of radio- to bolometric luminosity and effective temperature. We also plot the radio luminosity ratio against stellar radius, as shown in Fig. 4.29. Also here a first-order fit is performed on the logarithmic values, yielding yet another statistically significant relation:

$$L_R/L_{\text{bol}} \approx R_*^{-3.1046\pm2.607} \cdot 10^{-17.6112\pm1.101}. \tag{4.25}$$

We note that both of these relation cover the previous relations fitted using data from the previous surveys (excluding TGSS) with their 3σ intervals, which could mean that the ratio of radio- to bolometric luminosity is independent of frequency in the range from 144 MHz to 3 GHz, the implications of which are discussed in the Discussion section. As only two stars in our VLA FIRST sample have reported periods, no plots of the ratio of radio- to bolometric luminosity against rotation period or Rossby number are created, as fitting a trend to two points is not useful.

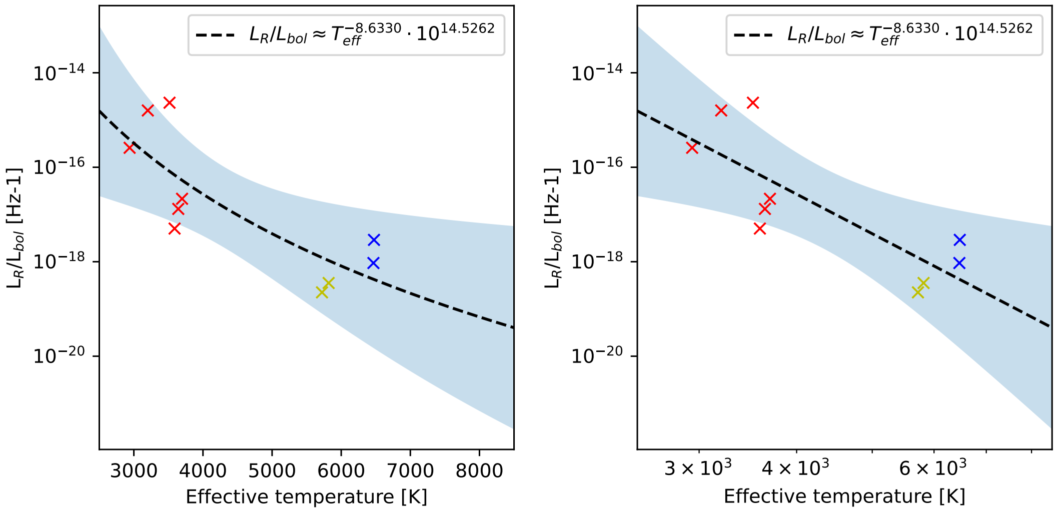

Figure 4.28: Plots of the ratio of radio- to bolometric luminosity against effective temperature for the sample of detected mains sequence stars in VLA first. A fitted first-order function is fitted to the logarithmic values, and is indicated by a black dashed line. Its 3σ region indicated by blue shading.

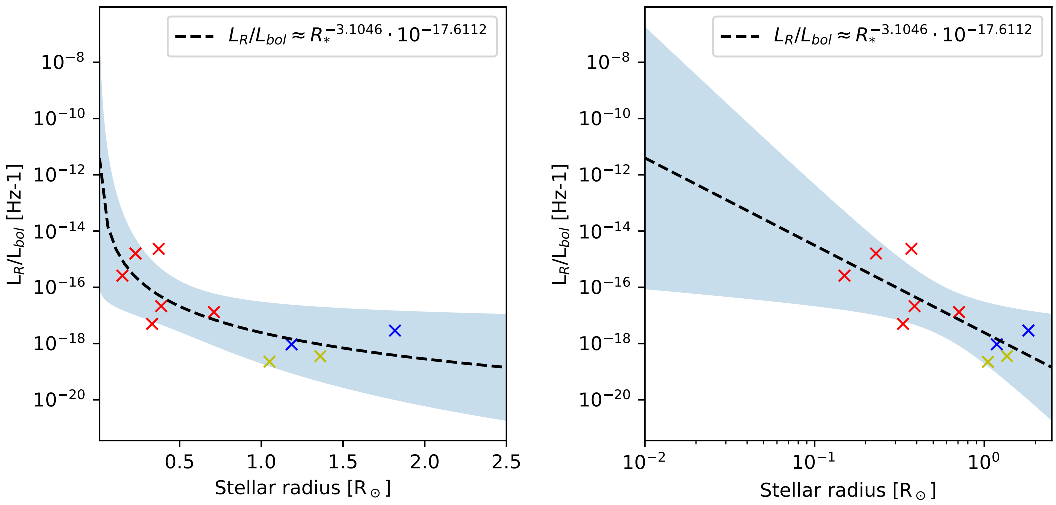

Figure 4.29: Plots of the ratio of radio- to bolometric luminosity against stellar radius for the sample of detected mains sequence stars in VLA first. A fitted first-order function is fitted to the logarithmic values, and is indicated by a black dashed line. Its 3σ region indicated by blue shading.

4.1.5 VLA Sky Survey

Fig. 4.30 includes bar charts showing the distributions of main sequence detections across our priority categories both before and after obviously false P1C1 detections are filtered out by eye. This by-eye filtering is performed due to a weakness of the sorting algorithm previously described in Sect. 3.2.3, where the Gaussian fitting function from CASA sometimes struggles to fit reasonable Gaussian functions in cutouts with poor pixel resolutions. This is therefore only a problem with VLASS and VLA FIRST, as they both have relatively poor pixel resolutions. There are also cases where the cutouts

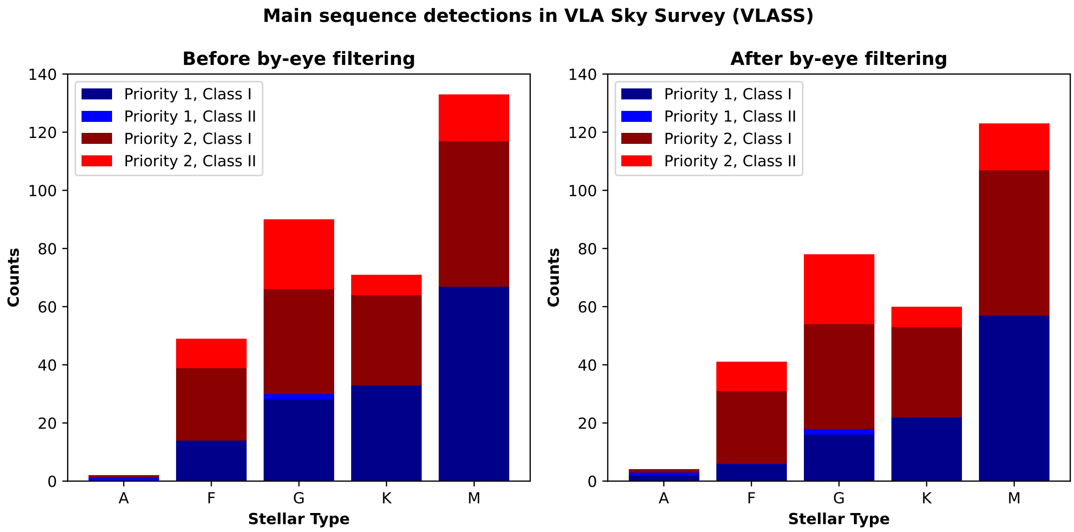

Figure 4.30: Bar charts showing the distribution of main sequence detections in VLASS, both before and after false P1C1 detections are filtered out by eye.

queried from VLASS are poor, sometimes being very homogeneously bright, where the sorting algorithm falsely assigns a P1C1 category, even though the huge and homogeneous flux in the cutout is obviously not due to stellar radiation.

The left-most bar chart in Fig. 4.30 shows the distribution of main sequence detections in VLASS given by the previously described sorting algorithm. We here see a clear relation where the number of P1C1 detections increases towards cooler, smaller and less massive stars. This is of course as expected, seeing as these types of stars are much more common in the galaxy, than their larger, hotter and more massive counterparts. Cooler stars, and especially M dwarfs are also thought to be more active. The number of detections falls nicely off towards larger and more massive stars, although we still have a surprising number of both F and G type stars. However, only two main sequence A types star are detected. The distribution of main sequence detections in VLASS after by-eye filtering out obviously false detections is shown in the right-most bar chart in Fig. 4.30. We have here lost a lot of the detections of the larger, hotter and more massive stars, but the A type detections remain. Most of the detections of M and K type dwarfs are found to be true detections and therefore kept. We are left with a main sequence sample of 103 main sequence AFGKM stars that we detect in VLA Sky Survey, two of type A, six of type F, 16 of type G, 22 of type K and 57 of type M. The entire sample of detected main sequence stars, their positions, distances and measured integrated flux are shown in Table 4.5.

Main sequence P1C1 detections in VLA Sky Survey (VLASS)

SIMBAD ID	Type	RA [deg]	DEC [deg]	S_I [mJy]	Distance [pc]
* b01 Hya	A3V	161.7220	-17.2954	47.4081	56.1814
V* BU Psc	A9V/IV	0.5159	-2.7640	7.6173	63.9036
HD 40216	F7V	88.9357	-38.1038	0.8906	52.7667
HD 177065	F2/3V	285.7715	3.8323	0.5372	98.9531
HD 14348	F5	34.9780	31.3374	2.0100	60.2936
HD 158736	F6V	262.7141	1.5811	0.4793	56.8703
HD 41221	F8	91.1809	25.1791	0.6203	85.3017
HD 125858	F5	215.2749	38.9888	2.9335	82.2106
HD 171587	G5V	279.0445	-10.8917	0.4972	35.0056
HD 255278	G5	95.1358	26.8550	0.6312	75.2486
HD 12763	G5	31.7413	57.7606	0.3005	97.1317

HD 10126	G8V	24.9087	28.1120	0.9582	31.7556
BD+38 2653	G5	231.1596	37.6883	0.4766	97.1656
TYC 1132-530-1	G5	324.9284	13.4072	1.0629	92.9371
TYC 4357-209-1	G5V	95.0386	73.8925	0.8145	76.4595
HD 295290	G0	100.0978	-3.5322	6.0289	60.5262
HD 199013	G0V	313.6768	-18.1504	0.8289	98.5905
HD 75524	G0	132.9689	38.9071	0.6864	75.6112
BD+15 2194	G5	155.7627	14.5373	0.5482	88.3539
HD 146562	G0V	244.2106	3.7719	4.2573	91.5478
HD 130838	G0	222.5088	12.3358	0.8611	86.0381
HD 295724	G0	103.6096	-2.8193	0.6588	43.9401
HD 224466	G0	359.5545	20.8369	1.0356	66.6880
HD 23565	G5V	57.1609	51.8223	4.7867	64.2141
HD 14635	K4-V	35.4407	-6.8787	0.6523	27.7283
BD-03 3937	K0	246.2062	-3.4539	0.7156	93.3382
BD+18 1512	K0	107.5507	18.4401	8.8168	61.7243
BD+40 2695	K2	207.5014	39.4051	0.9753	40.7963
HD 80133	K1/2V	139.4865	-3.3871	1.0884	32.2794
BPM 71732	K4/5V	82.9234	-9.8568	0.4788	93.2520
HD 275585	K0	54.6782	41.9819	0.4701	80.0006
TYC 3149-1560-1	K3V	298.6791	43.6263	0.6517	88.4208
BD-07 2388	K0	123.4667	-7.6392	1.2520	50.0627
1RXS J002012.0-341630	K5e	5.0512	-34.2701	1.0842	78.3546
BD+11 520	K4V	56.8521	11.4808	1.1235	48.8166
G 123-33	K5V	186.5931	35.9333	2.0656	47.7812
HD 314741	K5Ve	268.7306	-26.8275	1.7020	31.4492
G 187-21	K7	316.4222	26.6407	0.3855	54.3156
HD 98198	K1V	169.4491	0.7916	0.4873	37.4491
BD+13 2000	K0	132.7421	12.6229	0.5979	55.5876
CD-24 11855	K4V	226.6030	-24.7786	10.0295	61.1850
Wolf 456	K5V	194.9311	1.5397	0.5722	49.6954
StKM 1-374	K5	52.7974	31.1993	0.4642	82.9953
BD+39 2300	K2	149.9452	38.8195	0.5012	71.4845
LP 58-279	K5V	100.2442	63.8918	1.1536	39.0986
BD+01 806	K5V	71.0053	1.7279	1.7616	68.9606
2MASS J20363026-3131224	M6.0	309.1290	-31.5204	7.8720	34.8773
StKM 1-1332	M0.5V	245.6696	8.0396	0.6408	44.2636
PM J10581+5057	M3.52	164.5368	50.9519	0.9398	27.6724
PM J04472+2038	M5.0V	71.8058	20.6368	0.8513	23.2613
LP 864-20	M2.5	264.5407	-23.3767	0.4878	43.8885
LP 732-30	M4.5V	172.2352	-15.9381	10.1160	44.1612
2MASS J14440297+0250247	M7V	221.0171	2.8396	0.9526	92.8133
G 268-84	M3	14.5182	-23.3435	0.4561	40.5423
PM J07472+5020	M4.0Ve	116.8114	50.3463	0.3762	14.1090
LP 882-39	M3	11.8632	-27.1876	2.2708	49.3048
2MASS J16314393+4516226	M3.8	247.9390	45.2730	1.9059	70.2495
LP 691-15	M4.5V	282.2842	-3.2548	0.6384	17.1355
LP 930-43	M1	327.0054	-29.9414	0.7564	42.6901
2MASS J13582164-0046262	M5.5	209.5942	-0.7733	2.4236	45.9003
2MASS J11543135+1514471	M4V	178.6362	15.2487	0.5056	85.5273
V* CW UMa	M3.5V	167.9694	33.5382	1.6693	13.3540
2MASS J12182193+2744423	M3.9	184.5962	27.7465	0.7929	84.8748
2MASS J15141384+1201451	M8V	228.5621	12.0295	0.6968	48.2412
PM J05566-1018	M3.5V	89.1738	-10.3087	0.9042	15.9135
LSPM J1153+4302	M1.0V	178.3522	43.0499	0.5909	28.1958
2MASS J23412868-1133356	M7.9V	355.3768	-11.5584	0.7267	49.3889
LSPM J0551+3249	M3.3	87.7832	32.8316	1.0737	55.3479
V* IZ Boo	M3.0Ve	215.0240	39.0518	1.8367	36.0022
LP 99-246	M3	231.3581	60.7457	0.8365	37.5058
HG 7-141	M2	64.0211	18.8601	0.7765	48.0353
LSR J1835+3259	M8.5V	278.9123	32.9953	1.1989	5.6885
V* DD Cnc	M3-4	128.3456	20.7212	0.3321	49.3889

UCAC4 345-006842	M5	77.1185	-21.0280	3.9320	48.3029
UCAC4 354-189365	M5	317.5242	-19.3412	1.2440	33.5961
LSPM J1927+6802	M6.5V	291.7938	68.0378	0.8408	37.1365
2MASS J14325112+3636440	M9V	218.2175	36.6128	0.4035	47.8582
2MASS J09165078+2448559	M4.5	139.2156	24.8161	0.6197	35.0954
PM J04544+6504	M4.0V	73.6321	65.0803	0.7805	19.6092
2MASS J01574350-0948076	M4	29.4379	-9.8012	0.8306	97.2023
LP 205-44	M5.84	97.9661	41.4960	0.8069	27.8495
2MASS J14223872+0646143	M5V	215.6654	6.7722	2.9000	90.5978
UCAC4 334-001378	M3	18.3299	-23.2463	1.0260	59.6063
SDSS J094810.83+071343.5	M8	147.0497	7.2288	1.7171	89.3075
2MASS J04580385+4857169	M1.0	74.5217	48.9538	0.5461	80.0568
2MASS J16104135+5047114	M4.2	242.6763	50.7881	2.5260	84.2151
2MASS J20352037-3110083	M7.9V	308.8384	-31.1664	0.5106	33.6629
2MASS J14332295+3848226	M6V	218.3497	38.8089	0.3239	97.5783
Wolf 320	M3	130.6904	44.5428	1.0118	26.8561
RX J0506.2+0439	M4.5V	76.5586	4.6582	1.1465	27.6302
G 249-36	M4.5V	91.3817	60.8201	8.4162	16.2797
V* V374 Peg	M3.5Ve	330.3118	28.3084	1.4913	9.1029
LP 270-41	M4	212.0826	37.1431	0.3465	85.8770
LSPM J0529+2619	M2.5	82.3541	26.3325	0.9199	38.3712
[R78b] 233	M5V	54.1753	3.4893	1.7375	26.7764
2MASS J19243494-3442392	M4.0Ve	291.1508	-34.7103	1.1576	51.5468
BD+17 2966	M0	242.0257	17.2305	0.3868	32.0072
G 133-48	M6V	28.4636	44.4585	0.4854	23.9351
Ross 42	M4Ve	83.0646	9.8208	0.9274	12.9641
UCAC4 519-003400	M1.6	31.4743	13.7563	0.3931	64.6617
PM J20502-3424	M5e	312.5734	-34.4120	0.4388	9.6033
LP 52-34	M4Ve	184.9565	-23.5337	1.5134	27.7644
PM J03510+1413	M4.5V	57.7583	14.2284	0.5839	40.0331

Table 4.5: Table of P1C1 detections in VLA Sky Survey (VLASS).

The sample of main sequence detections in VLA Sky Survey are studied further by looking for possible relations between their measured brightness temperatures at the central frequency of VLASS, 3 GHz. The first parameter we plot the logarithms of the sample's brightness temperatures against its effective temperatures. A plot of 3 GHz brightness temperature against effective temperature is shown in Fig. 4.31, where the stars are coloured based on their SIMBAD spectral type. As the stellar effective temperatures are queried from a plethora of Vizier catalogues using VASE, the plotted effective temperatures may not coincide with the SIMBAD spectral type in some cases. This is most obvious for some of the stars SIMBAD report to be M types, but still having effective temperatures well above the usual boundary of 3500 K, the hottest having an effective temperature of $\sim$ 5000 K, which coincides more with a hot K dwarf star. Fig. 4.31 clearly shows that cooler stars are generally brighter in 3 GHz compared to their hotter counterparts, with the brightest M dwarfs having brightest temperatures around two orders of magnitude higher than the brightest F dwarfs. The decrease in log brightness temperature as effective temperature increases does however not appear to be linear, as we observe a sharp decrease in brightness temperature already for the M dwarf stars, while the brightness temperature seems to increase somewhat when reaching effective temperatures coinciding with K dwarf stars, before once again decreasing towards the hot K dwarf or cold G dwarf regime. Once again a slight increase is observed at G dwarf temperatures, but as the sample size is limited, it is not immediately obvious if the observed relation is in any way real, or just an effect of our very limited sample. However, the wave-like shape for M and K dwarf effective temperatures can not be immediately thrown out, as most of the

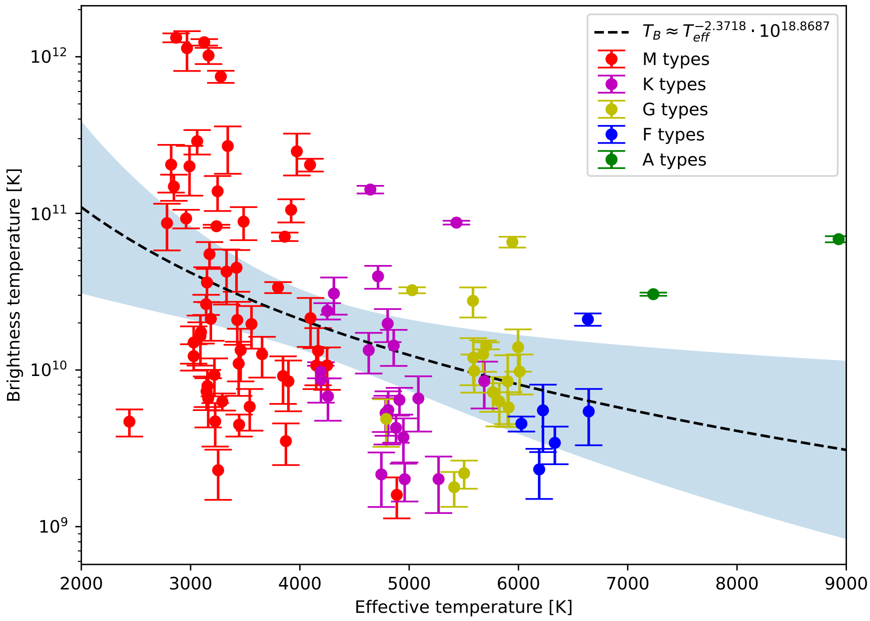

Figure 4.31: Plot of the measured brightness temperatures at 3 GHz of the detected main sequence stars in VLA Sky Survey as a function of effective temperature. The stars are coloured according to their SIMBAD spectral types.

observed sources follow this trend very nicely. As for the two A type stars we observe, we can't deduce an obvious trend, as we have too few data points in the temperature range between the FGKM sample and the two lonely A types. However, they both show brightness temperatures well above all the reported F dwarfs, making them both interesting targets for further analysis. Especially, as one of the A types is of type A3V and therefore thought to don't have either a chromosphere or corona, while the A9V/VI star is thought to be cold enough to have both a chromosphere and a corona.

Fig. 4.32 shows the computed brightness temperatures of every P1C1 detection in VLASS plotted over the stars' radii. The strange wave-like pattern observed in the plot of brightness temperature as a function of effective temperature is here not recreated, but the sharp increase in brightness temperature towards the cooler M dwarfs is still observed, although as before, the M dwarfs in our sample seem to span a relatively large range in brightness temperature. Instead of dropping sharply into a slightly decreasing wave-like pattern as we observed in Fig. 4.31, we here find the brightness temperature to drop sharply in radius range of 0.1-0.5 $R_\odot$, before reaching a point where the brightness temperatures as a function of radius seems to flatten out into a perhaps slightly declining linear function (in log-log). Some outliers above this relatively flat linear drop-off are observed, all seemingly within one order of magnitude brighter compared to their non-outlier counterparts. Fig. 4.32 also reveals a problem that was not that obvious in the effective temperature plot, that some of the stars in our sample are either wrongly taken to be main sequence, wrongly classified in SIMBAD or wrongly assigned stellar parameters in VASE. This is most evident for one of the right-most stars in Fig. 4.32 that has a stellar radius close to 2 $R_\odot$ while still having a spectral type of K in SIMBAD. This must therefore be either a K giant that has sneaked through our sorting algorithm described in Section 3.2.3, an A dwarf that has been wrongly classified to be a K dwarf and therefore having a wrong classification in SIMBAD, or a real K dwarf that for some reason has been assigned a wrong stellar radius by the VASE algorithm. The primary suspicion is that there is something wrong in the

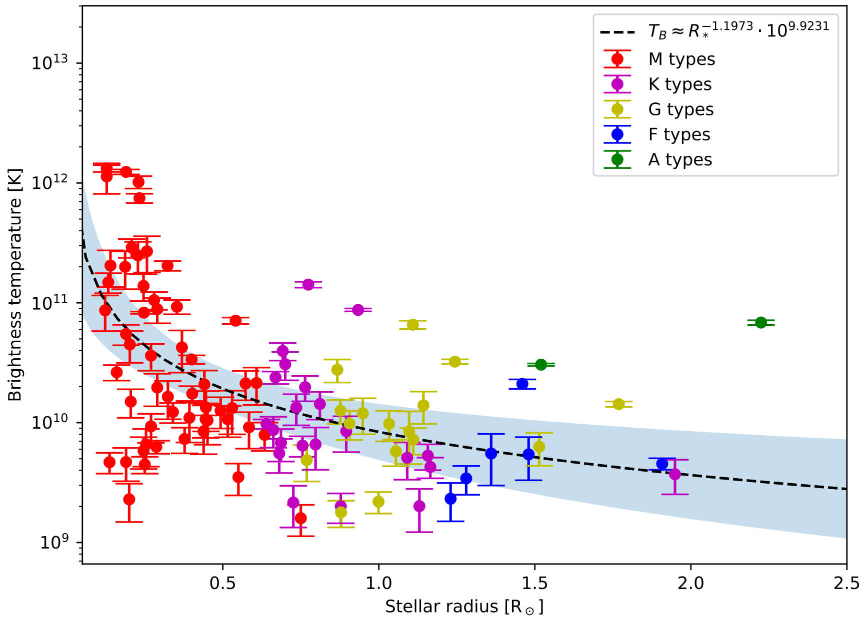

Figure 4.32: Measured brightness temperatures at 3 GHz of the detected main sequence stars in VLA Sky Survey as a function of radius. The stars are coloured according to their spectral type in SIMBAD.

sorting algorithm, either a plain bug in the code or a fault in how we sort the stars into categories. That is because there are plenty of cases that are found to have too large radii for their stellar classification, with at least two G dwarfs and one F dwarf having radii higher than the usual set limit for their spectral type, an indication that some giants are still in our main sequence sample. This is discussed in Section 5.1.

We also try to relate the measured brightness temperature to the activity indicator, rotation period. A plot of brightness temperature against rotation period is shown in Fig. 4.33. As in the previous surveys we find a large spread in brightness temperatures in similarly rotating stars, which makes determining a trend problematic. A first-order fit is performed on the log-log values, and yields the following statistically insignificant trend;

$$T_B \approx P_{rot}^{-0.1533\pm0.243} \cdot 10^{10.0835\pm0.228}, \tag{4.26}$$

where the plotted uncertainties correspond to the 3σ level. One can here immediately see that the fitted slope is insignificant (to the 3σ level) as its uncertainty is greater than its slope, thus containing the horizontal, where there is no relation between brightness temperature and rotation period.

We now move on to study how the fraction of radio- to bolometric luminosity relates to the same stellar parameters, as working with luminosities is more intuitive than working with high non-thermal brightness temperatures. As previously we start by relating the radio luminosity fraction to effective temperature, as shown in Fig. 4.34. As before, we here find a neat linear relationship between the logarithmic values, and a first-order fit on these values yields the following relation;

$$L_R/L_{\rm bol} \approx T_{\rm eff}^{-5.9975\pm1.776} \cdot 10^{4.7322\pm6.435}, \tag{4.27}$$

where the given uncertainties correspond to the 3σ level. We here find a statistically significant relation between the ratio of radio- to bolometric luminosity and effective

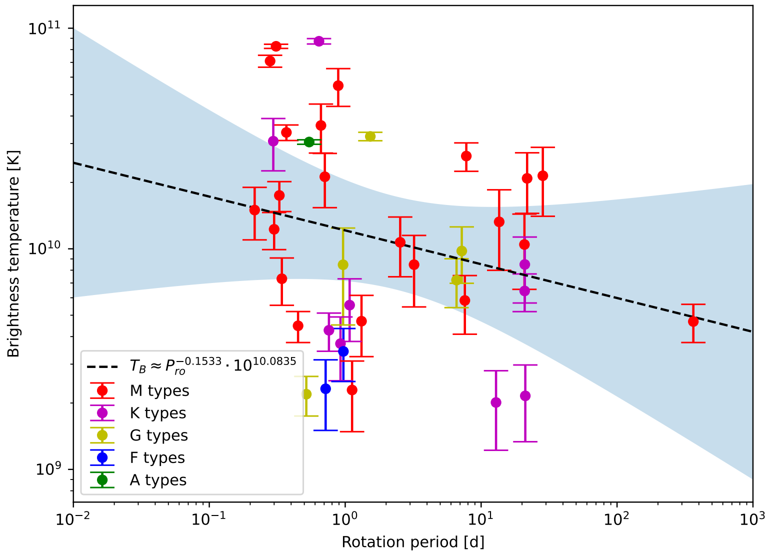

Figure 4.33: Plot of brightness temperature against rotation period for the main sequence stars detected in VLASS. A dashed black line is used to indicate the best fit, with blue marking the 3σ region around the fitted function.

temperature, as we have done for all previous surveys with detections. We also here find that about the hottest half of the detected M dwarfs have radio luminosity fractions considerably lower than the fitted function, while the coolest half generally have much higher radio fractions compared to the function. This difference might be caused by the transition from partially to fully convective stars, thought to happen around M4.5V. Fig. 4.35 shows plots of the ratio of radio- to bolometric luminosities against stellar radius, both in lin-log and log-log scales. The relation between the logarithms of the values looks very linear, and a first-order fit is performed on the logarithms, yielding the following relation with uncertainties corresponding to the 3σ level:

$$L_R/L_{\rm bol} \approx R^{-2.234\pm0.634} \cdot 10^{-17.6205\pm0.273}. \tag{4.28}$$

This relation is also statistically significant, and is found to follow the observed trend very well. As in the plot of brightness temperature against stellar radius in Fig. 4.32 we here observe a slight splitting in the M dwarf sample in the lin-log plot, where some of the sample is found to decrease in radio luminosity fraction as radius decreases, while the majority are found to have radio luminosity fractions that increase drastically as radius decreases. If this splitting of the M dwarf samples is in any way connected to the radio under- and over-luminosities for the lower and upper halves of the M dwarf sample seen in Fig. 4.34 is discussed further in the Discussion section. We also attempt to relate the radio- to bolometric luminosities to the rotation period, which is an important activity indicator, plots of which are shown in Fig. 4.36 both in lin-log and log-log scales. As before we find huge spreads in radio luminosity fractions, and no significant trend is found. Nevertheless, a first-order fit is performed on the logarithms, yielding the following statistically insignificant (to the 3σ level) relation,

$$L_R/L_{\rm bol} = P_{\rm rot}^{-0.3128\pm0.462} \cdot 10^{-17.1509\pm0.369}. \tag{4.29}$$

We note the detection of the very slowly rotating star LSR J1835+3259 (M8.5V) with a rotation period of ~ 364.2 days as a very interesting detection, which could end up

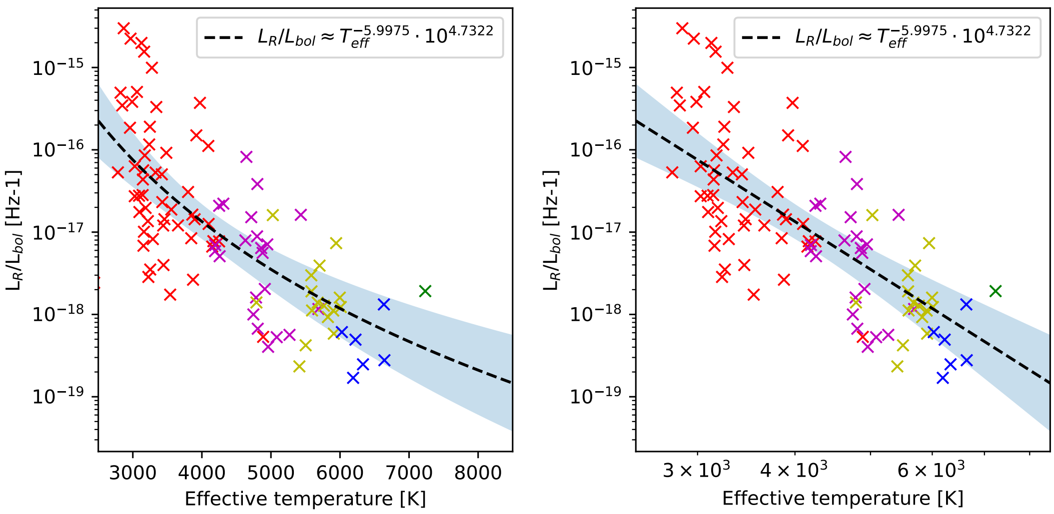

Figure 4.34: Plots of the ratio of radio- to bolometric luminosity against effective temperatures, both in lin-log and log-log scale. A dashed black line is used to indicate the best fit, with blue marking the 3σ region around the fitted function.

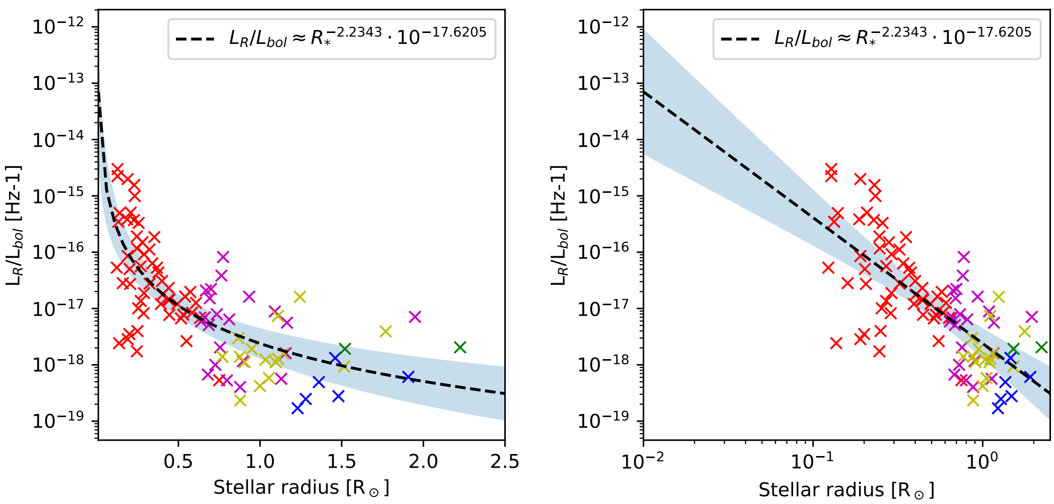

Figure 4.35: Plots of the ratio of radio- to bolometric luminosity against stellar radii, both in lin-log and log-log scale. A dashed black line is used to indicate the best fit, with blue marking the 3σ region around the fitted function.

as a prime target for future targeted studies. Similarly we try to relate the ratio of radio to bolometric luminosity to the Rossby number, also a frequently used activity indicator, plots of which are found in Fig. 4.37 both on lin-log and log-log scale. We here find a somewhat more noticeable trend in the log-log plot, and a first-order fit on the logarithms yields the following statistically significant trend:

$$L_R/L_{\mathrm{bol}} \approx R_O^{-0.4097\pm0.303} \cdot 10^{-17.8759\pm0.552}, \tag{4.30}$$

where the uncertainties correspond to the 3σ level as before. We here see that the majority of stars in our sample, for which the stellar parameters needed to compute the Rossby number are reported, have very low Rossby number. The only exception is the rotational variable BD-07 2388 (K0), which has a Rossby number of ~ 36.32.

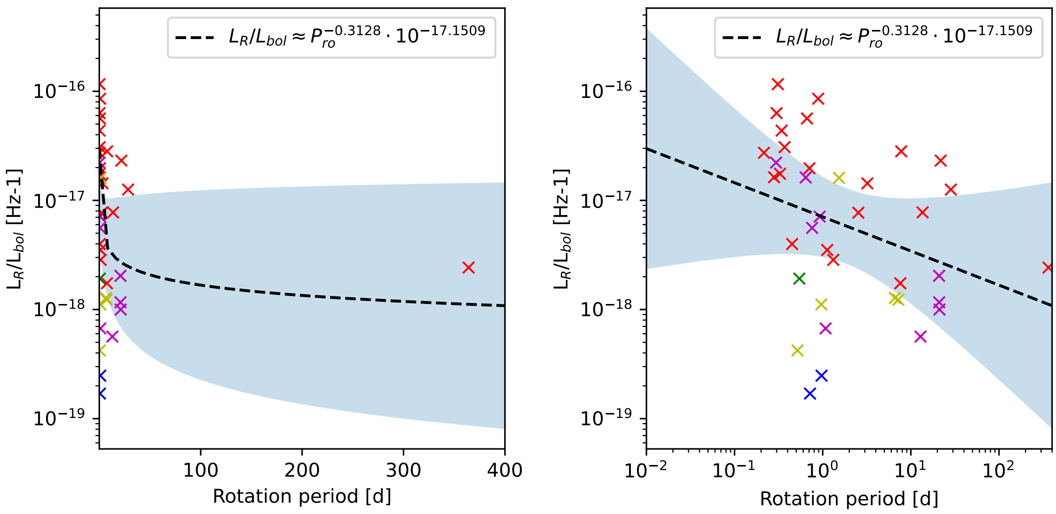

Figure 4.36: Plots of the ratio of radio- to bolometric luminosity against rotation period, both in lin-log and log-log scale. A dashed black line is used to indicate the best fit, with blue marking the 3σ region around the fitted function.

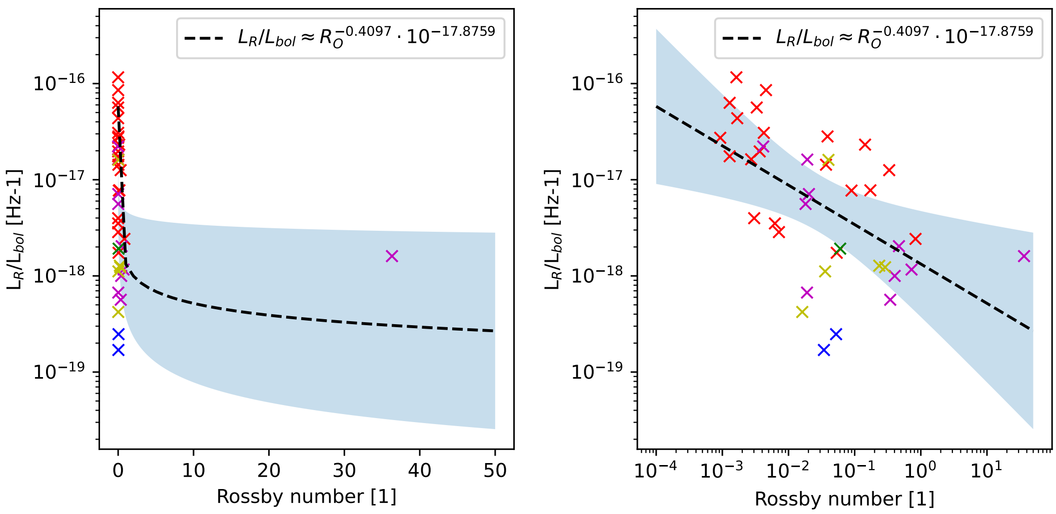

Figure 4.37: Plots of the ratio of radio- to bolometric luminosity against Rossby number, both in lin-log and log-log scale. A dashed black line is used to indicate the best fit, with blue marking the 3σ region around the fitted function.

4.2 Relating measured radio luminosities to bolometric luminosities

We have previously shown that the ratio of radio- to bolometric luminosity is both dependent on the star's effective temperature and radius. From the data from LoTSS we found the radio luminosity ratio to be proportional to $T_{\rm eff}^{-5.7526}$ and $R_*^{-2.101}$. Although individually fitted, these two proportionalities remind us of the expression for bolometric luminosity as a function of radius and effective temperature;

$$L_{\rm bol} = \left(\frac{R_*}{R_\odot}\right)^2 \left(\frac{T_{\rm eff,*}}{T_{\rm eff,\odot}}\right)^4, \tag{4.31}$$

where $R_\odot$ and $T_{\text{eff},\odot}$ is the solar radius and effective temperature respectively. As bolometric luminosity is only a function of radius and effective temperature, it would be very interesting to see how the ratio of radio- to bolometric luminosity varies as a function of it. If the radio luminosities are found to be more or less constant over our sample we expect the radio luminosity fraction to be inversely proportional to the bolometric luminosity, $L_R/L_{\text{bol}} \propto L_{\text{bol}}^{-1}$. Plots of the ratio of radio- to bolometric luminosity against bolometric luminosity for the five surveys with detections are shown in Fig. 4.38, with black lines showing first-order fits of the log-log values. We here find that the radio luminosity fraction is greater the lower the bolometric luminosity is. The slopes of the fitted curves are all surprisingly similar, and all surprisingly close to -1, which one would expect if the radio luminosity was independent stellar type. The shallowest slope is found from the VLASS survey, which has a slope of -0.7455, and the steepest slope is found from the VLA FIRST survey with a slope of -0.9138. However, due to the very small sample of stars we detect in VLA FIRST, this slope is not as significant as the others.

All fits and their associated 3σ uncertainties are summarised in Table 4.6, where the first row contains the fits of the ratio of radio- to bolometric luminosity against bolometric luminosity. It is here clear that all five slopes are very similar and within each other's 3σ uncertainty. This means that how the fraction of radio- to bolometric luminosity evolves as a function of bolometric luminosity is independent of frequency in the range 144 MHz - 3 GHz. However, the constant offsets are not all found to lie within each other's uncertainties, meaning that the value of the radio luminosity fraction is not completely independent of frequency in the considered range. It is however noted that the constant offsets are surprisingly similar, as just the offsets from TGSS and RACS are found to lie outside the 3σ uncertainties of the other surveys. The deviation in TGSS is likely caused by a systematic effect of its flux calibration, which we discuss further in Sect. 5.6. The exponent of the offset in RACS is very similar to the others, but it is a bit smaller, meaning that the fraction of radio- to bolometric luminosity should be a bit higher in RACS compared to the remaining surveys, except TGSS. The frequency dependence of other fits are explored further in Sect. 4.3.

Survey Frequency		LoTSS 144 MHz	TGSS 150 MHz	RACS 887.5 MHz	VLA FIRST 1.4 GHz	VLASS 3 GHz
L_R/L_{bol} vs L_{bol}	X	-0.85 ± 0.19	-0.81 ± 0.15	-0.74 ± 0.23	-0.91 ± 0.79	-0.75 ± 0.17
	Y	-17.85 ± 0.26	-15.66 ± 0.16	-17.00 ± 0.28	-17.84 ± 1.24	-17.85 ± 0.27
T_B vs T_{eff}	X	-3.8 ± 1.9	-3.3 ± 1.6	-2.2 ± 2.4	-4.8 ± 7.2	-2.4 ± 1.6
	Y	26.9 ± 7.0	27.1 ± 5.8	20.2 ± 9.036	28.5 ± 26.2	18.9 ± 5.8
T_B vs R_x	X	-1.53 ± 0.68	-1.40 ± 0.54	-1.2 ± 0.9	-1.8 ± 2.7	-1.20 ± 0.54
	Y	12.62 ± 0.26	14.77 ± 0.17	11.86 ± 0.30	10.6 ± 1.1	9.92 ± 0.23
T_B vs P_{rot}	X	-0.05 ± 0.65	0.05 ± 0.46	0.26 ± 0.50	–	-0.15 ± 0.24
	Y	12.57 ± 0.92	14.54 ± 0.48	11.06 ± 0.65	–	10.08 ± 0.23
L_R/L_{bol} vs T_{eff}	X	-7.7 ± 1.9	-7.1 ± 1.4	-5.5 ± 2.8	-8.6 ± 6.7	-6.0 ± 1.8
	Y	10.93 ± 6.9	11.1 ± 5.1	3.7 ± 10.2	14.5 ± 24.4	4.7 ± 6.3
L_R/L_{bol} vs R_*	X	-1.53 ± 0.68	-2.30 ± 0.52	-2.4 ± 0.8	-3.1 ± 2.6	-2.23 ± 0.64
	Y	-17.66 ± 0.26	-15.44 ± 0.17	-16.86 ± 0.27	-17.6 ± 1.1	-17.62 ± 0.27
L_R/L_{bol} vs P_{rot}	X	0.25 ± 0.78	-0.03 ± 0.66	0.70 ± 0.65	–	-0.31 ± 0.46
	Y	-17.88 ± 1.1	-15.80 ± 0.60	-18.19 ± 0.82	–	-17.15 ± 0.37
L_R/L_{bol} vs R_O	X	-0.13 ± 0.89	-0.11 ± 0.62	0.46 ± 0.72	–	-0.41 ± 0.30
	Y	-17.63 ± 0.71	-15.87 ± 0.65	-17.22 ± 0.65	–	-17.88 ± 0.55

Table 4.6: Exponents with 3σ uncertainties for all fitted relations across the five radio surveys with detections. The fits have the form $A \approx B^X \cdot 10^Y$.

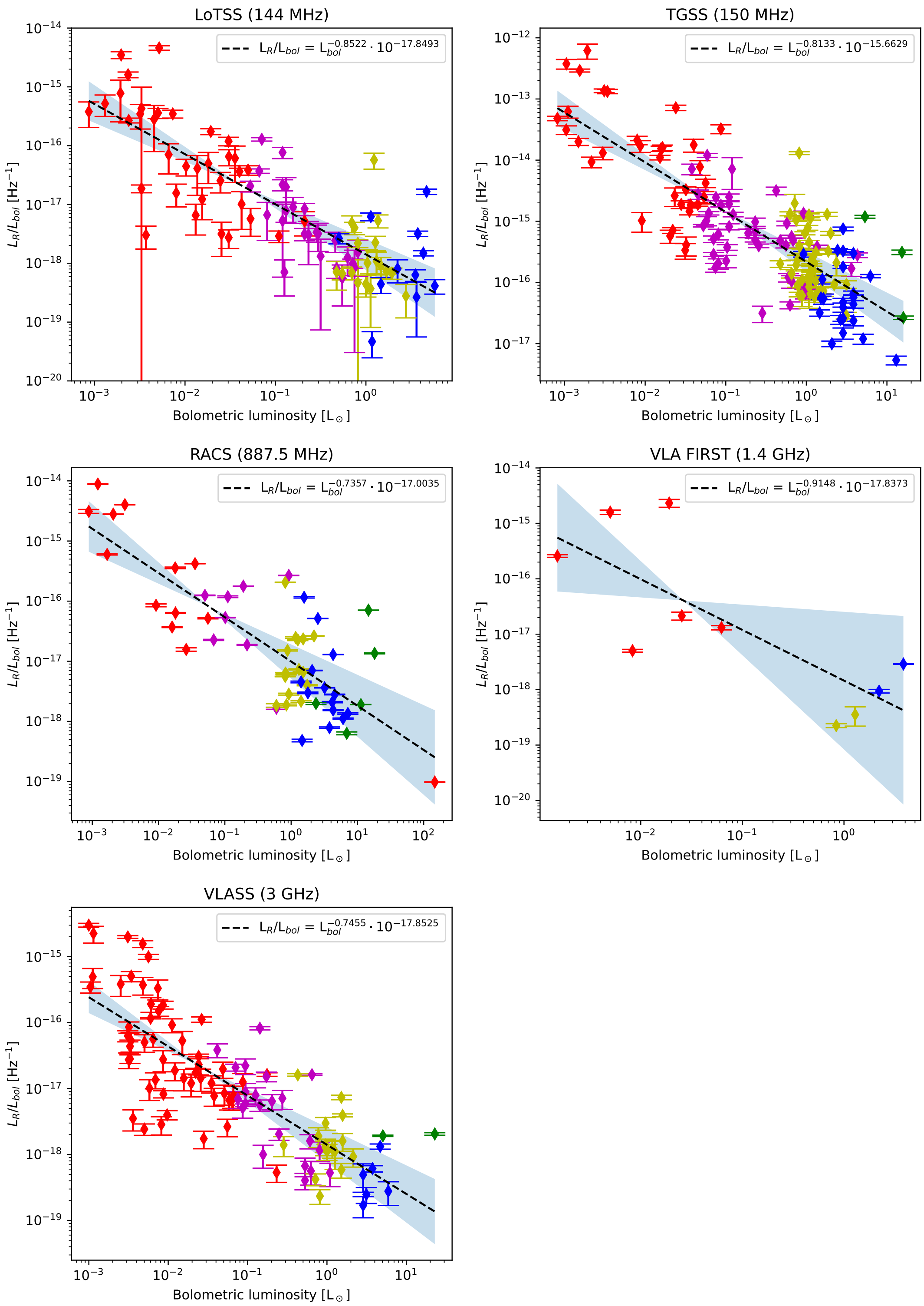

Figure 4.38: Plots of the ratios of radio- to bolometric luminosity against bolometric luminosity. dashed black lines show the fitted functions, and blue regions indicate the 3σ confidence intervals.

4.3 Frequency-dependence of the found relations

In Sect. 4.1, we have derived relations between stellar parameters and observed brightness temperatures and radio luminosities for each of the five radio surveys. All fits between a quantity A and B follow the form

$$A \approx B^X \cdot 10^Y \tag{4.32}$$

The exponents X and Y for all fitted relations and the associated 3σ uncertainties are summarised in Table 4.6. Please note that for VLA FIRST the data was only sufficient to derive four of these relations. We now want to compare the fitted relations across frequency (as probed by the different surveys) to determine any possible frequency-dependence. Just by eye one can here easily see that the fitted trends are very similar across all frequencies, as the fitted slopes in the log-log plane are always within the error bars of the slopes of the other surveys. There does however seem to be some flux-dependence of the constant offsets. To clearly see if we have any flux-dependencies in our slopes or offsets we plot the log slope and offset as functions of frequency for each of the seven different fitted relations. These plots are shown in Fig. 4.39, the left column showing the frequency dependence of the fitted slopes and the right column the frequency dependence of the fitted constant offset. We here find that the slopes are generally frequency-independent, as all of the slopes' 3σ uncertainties seem to overlap. This means that how brightness temperature and/or the ratio of radio- to bolometric luminosity evolves as functions of the considered stellar parameters is independent of frequency in the range 144 MHz - 3 GHz. However, this does not mean that the values are the same across all frequencies, which we see by looking at the plots of the constant offsets as functions of frequency.

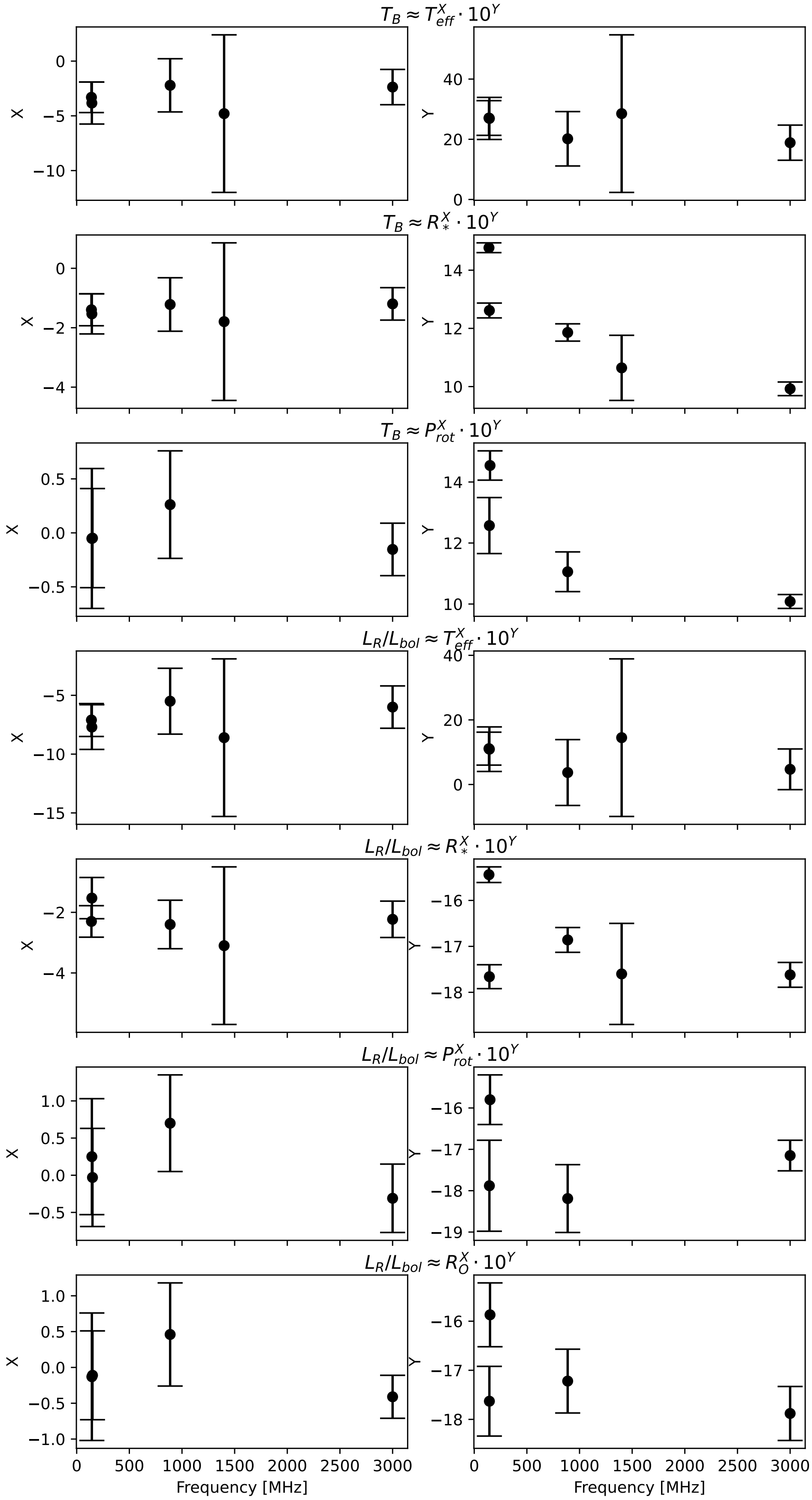

Figure 4.39: The frequency dependence of our fitted relations, the left column showing the frequency dependence of the slope, and the right column the frequency dependence of the constant offset.

As before we note that the offsets from TGSS consistently deviate from those of LoTSS by about two orders of magnitude, which we discuss further in Sect. 5.6. As we believe this two order of magnitude deviation is due to a systematic effect in the flux calibration, we interpret TGSS' offsets to lie closer to those of LoTSS when looking for frequency-dependence. Surprisingly, for the relation between brightness- and effective temperature we find the offsets' uncertainties to overlap, meaning that we can not conclude that the measured brightness temperature are frequency-dependent from this plot alone. However, for the relation between brightness temperature and stellar radius we find an obvious decrease in the offset as a function of frequency, and the same can be said for the relation of brightness temperature and rotation period. The offsets from the relation between the ratio of radio- to bolometric luminosity are once again frequency-independent. From the relation between the radio luminosity ratio and stellar radius we surprisingly see a slight increase in the offset going from 144 MHz to 887.5 MHz, before a decrease again towards 3 GHz. It is noted that the increase is statistically significant. Neither of the relations between the ratio of radio- to bolometric luminosity show statistically significant frequency-dependence. However, one can again discern a slight increase between 144 and 887.5 MHz, although this increase is now statistically insignificant.

4.4 Secondary samples

Finally, we present the secondary samples of detections in the considered surveys. Bar charts showing the distribution of detections of the different categories across the considered surveys are found in Fig. 4.40. Sadly the website hosting the VLA FIRST data our scripts depend on to query sky cutouts was down during our query, so we only report detections from LoTSS, TGSS, RACS and VLASS. Binary stars are detected in all fours surveys, and we detect 36 binaries in LoTSS, 43 in TGSS, 255 in RACS and 98 in VLASS. Young stellar objects (YSO) are only detected in TGSS, RACS and VLASS. In TGSS we detect 1 yso, in RACS we detect 8 and in VLASS we detect 2. We find evidence of radio emission from white dwarfs in all four surveys. We detect 15 white dwarfs in LoTSS, 21 in TGSS, 87 in RACS and 6 in VLASS. Sub-dwarfs are only detected in RACS, however. Where we detect 3 stars. Giants stars are detected in all four surveys, and we detect 1 in LoTSS, 13 in TGSS, 37 in RACS and 4 in VLASS. No P1C1 detections of evolved stars are found in any of the four considered surveys, but five secondary detections are found in RACS. From the bar charts it is found that RACS has the most detections of all categories. These secondary samples are not analysed further, but could still prove useful in further work.

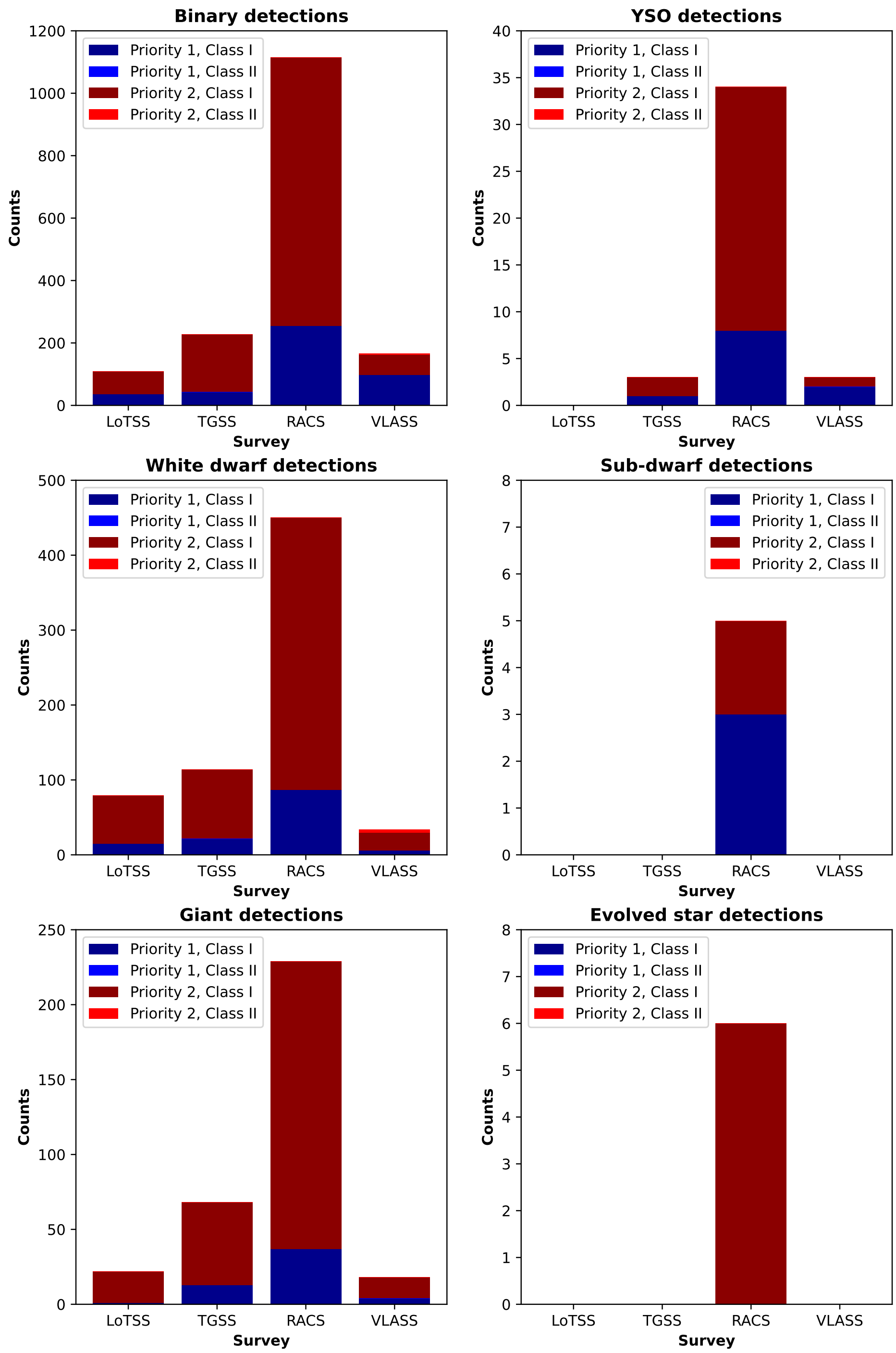

Figure 4.40: The distributions of secondary detections across the considered radio surveys.

Chapter 5

Discussion

5.1 On the quality of our filtering

In Section 3.2.2 we describe how we sort the stars in the initial Gaia DR3 catalogue into fitting categories based on their luminosity class and/or object types. This is found to work well for the majority of the stars, but some stars that have not been observed thoroughly before may lack appropriate object types in SIMBAD. For example, a giant star that has not been studied in detail before may not have a specified luminosity class and only have the object type of Star* in SIMBAD, while in reality it should also have object types associated with it being a giant. In this case, our sorting algorithm would let the star being included in our sample of single main sequence stars, thus creating the potential of wrongly interpreting the emission from giants to originate from main sequence stars. To check how large of an issue this is we plot the bolometric luminosity against the effective temperature for our LoTSS main sequence sample, which should show a neat relation similar to the H-R diagram. Thus we should be able to easily detect any non-main sequence stars as outliers. The resulting plot in Figure 5.1 shows a neat and almost perfectly linear relation of the effective temperature and the logarithmic bolometric luminosity. Most of the samples lie along the obvious main sequence, although there are a few obvious outliers. In particular we see a star of spectral type G that is a bit brighter than its similarly hot counterparts, which could be because of it being a giant star, as bolometric luminosity is related to both effective temperature and radius through:

$$\frac{L}{L\odot} = \left(\frac{R}{R_\odot}\right)^2 \left(\frac{T}{T_\odot}\right)^4, \tag{5.1}$$

such that the only way two stars of similar temperatures should have different bolometric lumenosities is that they have different radii. By checking our sample from LoTSS we see that the outlying G type star is HD 63932 which does in fact not have a reported luminosity class in SIMBAD. By checking its radius we see that it has a radius of 2.71 $R_\odot$, which confirms the suspicion that this star is obviously a giant that has been wrongly included into our sample of main sequence stars due to incomplete information. Similarly, we see that one of the relatively hot M dwarfs has a much smaller bolometric luminosity than what we would expect of a main sequence star. However, further investigation reveals that this star is [BHR2005] 161, which does in fact have a luminosity class V reported in SIMBAD although it cannot be completely ruled out that this is a sub-dwarf nonetheless. To get a better sense of the problem we also plot the bolometric luminosities versus effective temperatures for the remaining

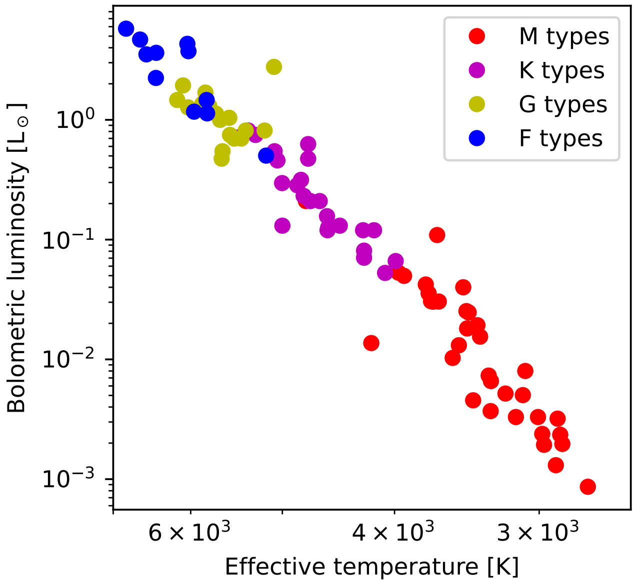

Figure 5.1: Plot showing bolometric luminosity against effective temperature for our main sequence sample from LoTSS.

samples, namely those of TGSS, RACS, FIRST and VLASS, and these plots are shown in Figure 5.2. The top-left plot is of the sample from TGSS, and we also here see a neat main sequence, although four obvious outliers are observed, namely three stars of type K and one of type G. These four outliers lie above the main sequence, and are therefore probably giant stars. The three K type stars are HD 47979 (K0), HD 178693 (K0) and HD 155524 (K2) and have respective radii 7.1, 5.88 and 4.794 $R_\odot$, thus all being giant stars. Checking their SIMBAD spectral types reveals that neither of the three outlying K stars have reported luminosity classes. The outlying G type is HD 17552 (G5) with a radius of 3.4782 $R_\odot$, therefore also being a giant.

Another giant is found in the RACS sample shown in the top-right plot, now being a M type star. Its luminosity of 147 $L_\odot$ is much greater than the expected luminosity on the main sequence, meaning that this star is probably a giant star. The outlying M dwarf is found to be 2MASS J18151564-4927472, with a spectral type M3 in SIMBAD. The star does not have a reported radius, but its mass is found to be 3.78 $M_\odot$, high enough to be associated with a giant. The remaining plots of the samples from VLA FIRST and VLASS shown no obvious outliers, as all the stars follow the neat relation expected from main sequence stars.

We have showed that some of our samples host giant stars that are able to sneak through our filtering by not having specified luminosity classes in SIMBAD in addition to missing object types associated with giants. However, the number of giants that sneak through is very low, their completely different luminosities can influence the analysis greatly if left unchecked. Because of this we are required to filter them out when creating the plots in the Results section to circumvent this problem with our sorting algorithm. This filtering error is something that could be fixed in the future, either by better surveys that are able to assign correct luminosity classes to more of the stars in SIMBAD, or more practically by just querying VASE for stellar parameters

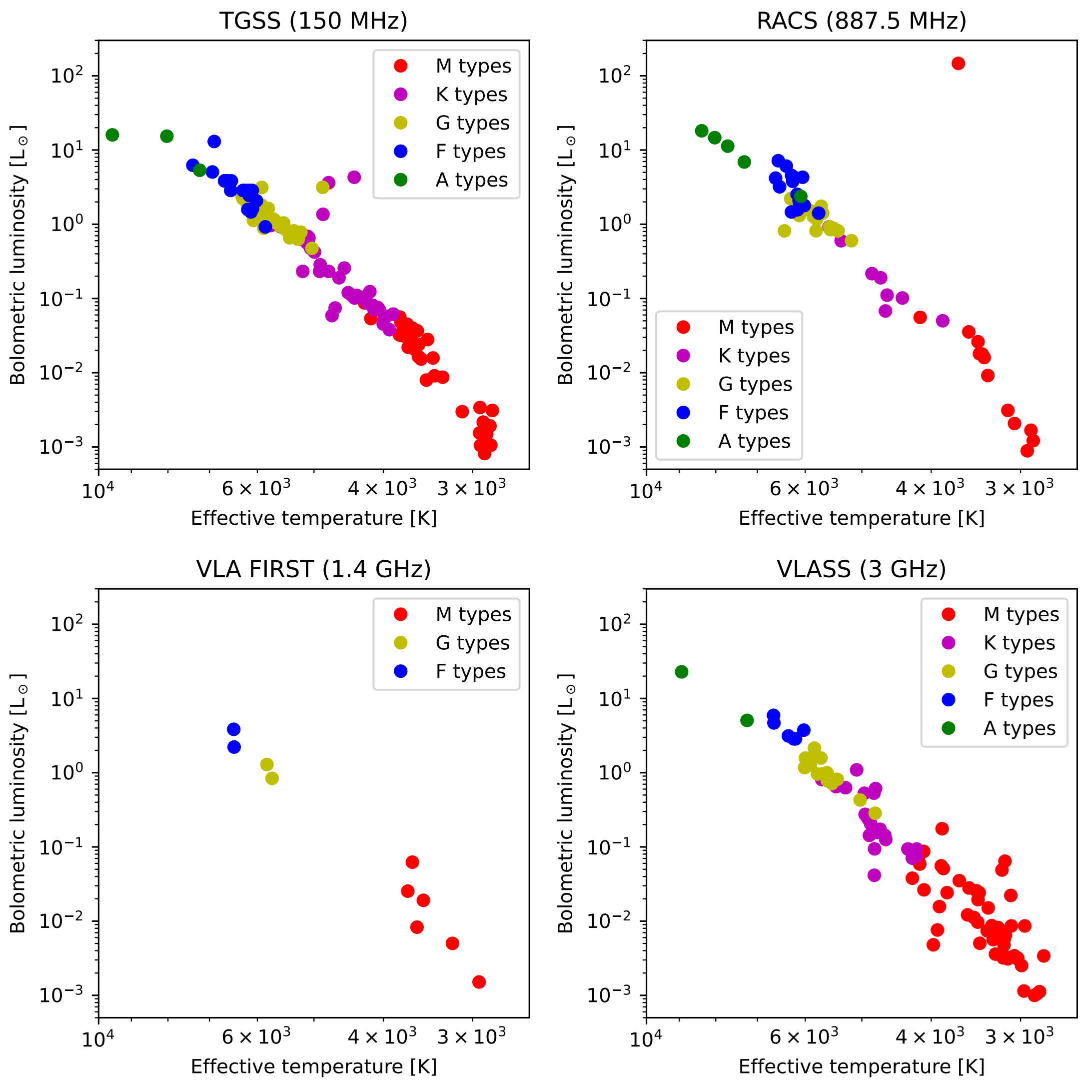

Figure 5.2: Plots of bolometric luminosity versus effective temperature for TGSS, RACS, VLA FIRST and VLASS. Clear mean sequences are observed, with some of the samples having a few outliers.

before filtering and querying cutouts. We would thus be able to sort based on stellar parameters as well.

5.2 On the size and completeness of our samples

To investigate the completeness of our sample of detected stars we peforms some comparisons with a similar catalogue of detected M dwarfs in LOFAR. Callingham et al. (2021) have blindly searched LoTSS for coherent emission, and present in total 19 detections of coherent radio emission associated with known M dwarfs of which only one had been previously reported. To check the completeness of our sample we want to compare our sample to theirs, but there are a few key differences in our methods that makes this difficult. Callingham et al. (2021) searched Stokes V maps for signs of stellar emission, while we opted for using Stokes I maps. This means that they might report stars that are obviously detected in Stokes V, while not being detected in Stokes I, and the other way around. In both cases sources above the 4σ threshold are counted as detected. Secondly, another problem arises from us using the Gaia DR3 catalogue as an initial catalogue, from which we take stellar positions to query cutouts of. This introduces the problem of us not being able to detect stars that are not part of Gaia DR3, which Callingham et al. (2021) circumvent this issue by blindly looking for stellar emission in LoTSS before cross-matching with Gaia, thus also finding evidence of sources which are not reported in Gaia. Thirdly, as we have made ourselves dependent on SIMBAD for querying both spectral and object types of the sources, we are not able to detect stars which do not have a specified spectral type in SIMBAD. Lastly, as our focus is on single main sequence stars, and Callingham et al. (2021) looked for every M-type star, we will only be comparing our sample to the single main sequence stars in their sample.

Taking all these limitations into account, there are only six stars in Callingham et al. (2021) that we should in theory be able to detect (see Table 5.1). However, we are only able to detect four out of these six. On further inspection, it appears like LP 169-22 and MCC 135 have been given P3C2 designations by our method, being both non-detections. To explore this further we plot their sky cutouts in Figure 5.3 in order to see if any obvious stellar emission can be seen by eye in either of the two cutouts. The left plot shows a Stokes I cutout from LoTSS-DR2 centred on the expected position of LP 169-22, but no obvious central source can be seen. However, two semi-circular and relatively bright patches are found, one on the left and one on the right of the expected position. The image is relatively noisy however, so that neither of the two seemingly bright patches have fluxes above the 4σ threshold. The right plot shows a LoTSS cutout centred on the expected position of MCC 135. We here see a dark patch covering the expected position of the source, however it is not found to be above the significance threshold and therefore also discarded. As neither of the two cutouts show very strong signs of significant stellar emission, we can conclude that the reason for us not detecting LP 169-22 and MCC 135 while Callingham et al. (2021) does, is that we search for emission in Stokes I, while they search in Stokes V, and not a fault of our method of handling detections.

This Stokes V and I difference, is likely why we report that many more single M dwarfs than Callingham et al. (2021), as sources can be bright in radio without being polarised, and Stokes V is used to indicate the direction of polarisation, be it counterclockwise or clockwise. We report a total of 37 single main sequence stars in LoTSS-DR2 in comparison.

Name	Spectral type	Detected?
LP 212-62	M5.0V	Yes
V* CW UMa	M3.5V	Yes
LP 169-22	M5.5	No
G 122-49	M4.5V	Yes
MCC 135	M1.5V	No
G 223-74	M3.0V	Yes

Table 5.1: Table of sources in Callingham et al. (2021) that we should theoretically be able to detect.

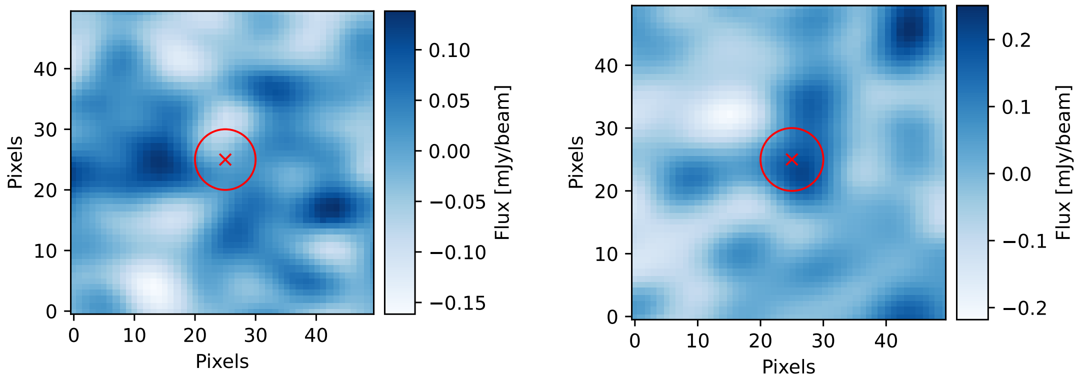

Figure 5.3: The left plot is the sky cutout from LoTSS centred on the expected position of LP 169-22, while the right plot is centred on MCC 135. A red cross is used to indicate the expected position, while a red circle is used to indicate the somewhat idealised beam shape.

5.3 Potential origin of low-frequency radio emission

Callingham et al. (2021) created the first blindly formed sample of coherently emitting stellar systems at 144 MHz. Similarly to what we have attempted, they also investigate the potential origins of the detected emission by looking for trends with different stellar properties, namely the coronal- and chromospheric activity indicators of rotation period and Rossby number. By doing so investigating if the observed coherent emission is powered by processes in the corona or the chromosphere.

In their attempt at relating their measured radio luminosity to the rotation period, they too struggle to discern any significant relation between the two, just as we did in our attempt at relating brightness temperature or ratio of radio- to bolometric luminosity. Out of their original sample of 19 M dwarfs, Callingham et al. (2021) report periods for 12 of them, eight binaries and four single stars, three of which we also detect. They state that no significant trend could be found within 95% confidence, which we also found to be the case using our LoTSS main sequence sample. In our attempt at relating rotation period to radio luminosity we end up with a second-order fit of the log-log values to be the best, with a p-value associated with the second-order term being 0.051. We are thus very close to having a trend within 95% confidence, but we are not able to find better relations. We are therefore only able to determine that there is a relation between a star's rotation period and 144 MHz radio luminosity within 94.9% confidence. Figure 5.4 shows radio luminosity against rotation period for our main sequence sample from LoTSS. The best second-order fit is shown as a dashed black lines, with blue indicating the associated 95% confidence region. Note that this confidence region includes the horizontal, as we are not able to prove a trend within 95% confidence. We overplot the sample of Callingham et al. (2021) in black, diamonds being used to indicate single stars and circles to indicate binaries. We here find that the single stars lie closer to our fitted function in general, but as we only have four single stars to compare with we can't really make any conclusions. The binaries span a large interval in radio luminosites, binaries with very similar rotation periods being found to have radio luminosities almost two orders of magnitude apart. However, it is noted that the majority of the binaries from Callingham et al. (2021) have lower radio luminosites compared to our fit, even outside the 95% confidence region. This could be

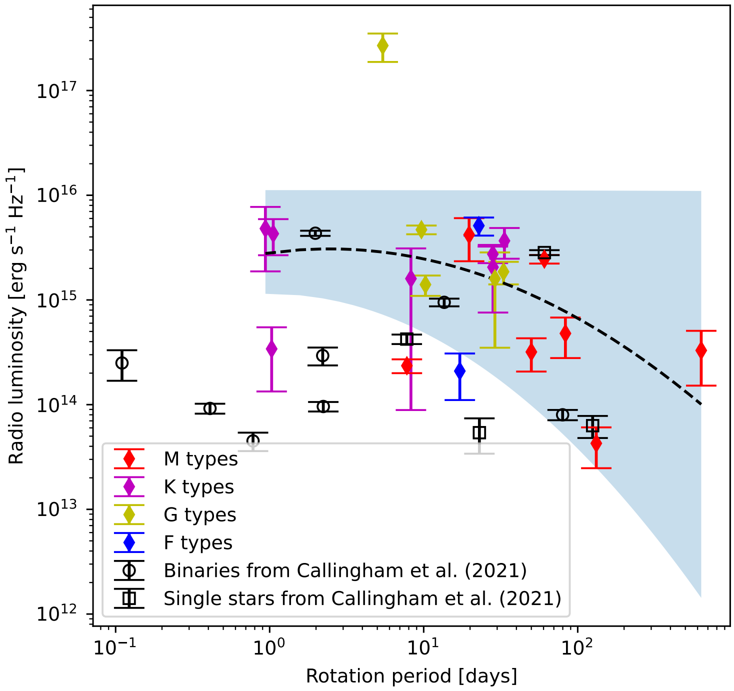

Figure 5.4: Plot of radio luminosity against rotation period for our main sequence sample from LoTSS. A second-order fit of the log-log values is indicated by the black dashed line, with blue indicating its 95% confidence region. The sample of M dwarfs from Callingham et al. (2021) is shown in black with appropriate error bars, the single stars as squares and binaries as circles.

an indication that the emission mechanisms responsible for the observed low-frequency radio emission are different between the single main sequence stars and the binaries.

Callingham et al. (2021) state that their sample likely consists of systems that produce low-frequency radio emission by either plasma emission or the electron-cyclotron maser instability (ECMI), and that there are only two known mechanisms that could power the possible ECMI emission, namely co-rotation breakdown and interaction with a magnetised satellite, such as an exoplanet. The former they write off for any star with rotation period greater than two days, and therefore argue that the ECMI mechanism for stars in their sample could be driven by either star-planet interactions or some unknown mechanism. Only three stars in our main sequence sample from LoTSS have periods shorter than two days, and by the arguments of Callingham et al. (2021), the observed radio emission from the remaining stars could be due to interactions with orbiting exoplanets. Especially interesting is the star G 74-29 (M3) which has a rotation period of 633.8 days, and has both a mass and a radius coinciding with a star on the main sequence.

Guedel & Benz (1993) proved that a relation between a stars X-ray luminosity and quasi-quiescent radio luminosity at 5 GHz exists for chromospherically active stars and binaries, commonly called the Güdel-Benz relation. They found the relation to be;

$$L_X \approx L_R \times 10^{15.5}. \tag{5.2}$$

Vedantham et al. (2022) state that the soft X-ray emission is due to thermal Bremsstrahlung, while the 5 GHz radio emission is thought to originate in incoherent gyrosynchrotron emission. Callingham et al. (2021) plot their sample of detected M dwarfs in LOFAR against the Güdel-Benz relation, and conclude that their sample is radio-overluminous and does not follow the relation. Similarly to Callingham et al. (2021), Vedantham et al. (2022) searched LOFAR for stellar emission, but chose to focus their efforts on RS CVn binaries and other high activity stars. They state that since that the highly polarised radio emission they find at 144 MHz likely originates in a coherent emission mechanism their sample should not follow the Güdel-Benz relation. However, they find their sample of mostly RS CVn binaries to adhere to the relation. Because of this we also want to explore were our sample of detections in LOFAR lie in relation to theirs. Figure 5.5 shows a plot of radio luminosity against x-ray luminosity for our samples of detected single main sequence stars and binaries in LOFAR. Note that very few of the reported single main sequence stars have reported x-ray luminosities in Vizier. We also show the samples of Callingham et al. (2021) and Vedantham et al. (2022) as black diamonds and circles respectively. We here find that our small sample of single main sequence stars of two M dwarfs, one G dwarf and one F dwarf are all radio-bright, meaning that they lie below the Güdel-Benz relation. Our larger sample of binaries with reported x-ray luminosities however, seem to span a large interval of x-ray luminosities, some even seemingly following the Güdel-Benz relation quite well. Vedantham et al. (2022) state that there could be a variety of reasons for the disconnect between the sample of cool M dwarfs from Callingham et al. (2021) and the Güdel-Benz relation, stating that it could be because the radio emission from these stars instead originates in a coherent cyclotron maser mechanism, or that the emission is still gyrosynchrotron, but because of the energetics of the cool M dwarfs they are not able to retain a stable thermal corona. However, we also show examples of G and F dwarfs that don't follow the relation, meaning that any preferred explanation of why cool M dwarfs do not follow the relation should also apply to them.

Some of the stars in our sample of detected binaries in LoTSS do seem to follow the Güdel-Benz relation, however the majority of the detected systems are still radio-overluminous. Vedantham et al. (2022) state that the reason their sample follows the Güdel-Benz relation so well could be that either the 144 MHz and 5 GHz radio emission originate in the same mechanism, or that they originate in two different mechanisms that produce very similar luminosities. As our sample of binaries only partially follows the relation we are not able to add much to their argument, only that the binary systems that do disconnect from the relation should not be disregarded. As Vedantham et al. (2022) state, more observations in the radio band spanning from 100s of MHz to GHz are needed to further study how the radio luminosities evolve as a function of frequency. This is something we have looked at briefly in our project, finding that the radio luminosities evolved very similarly as functions of various stellar parameters, independently of frequency, strengthening one of the arguments of Vedantham et al. (2022) that the spectrum between 144 MHz and 5 GHz could be flat. An example of this was shown in Figure 4.38, where it was found that the radio luminosity evolved

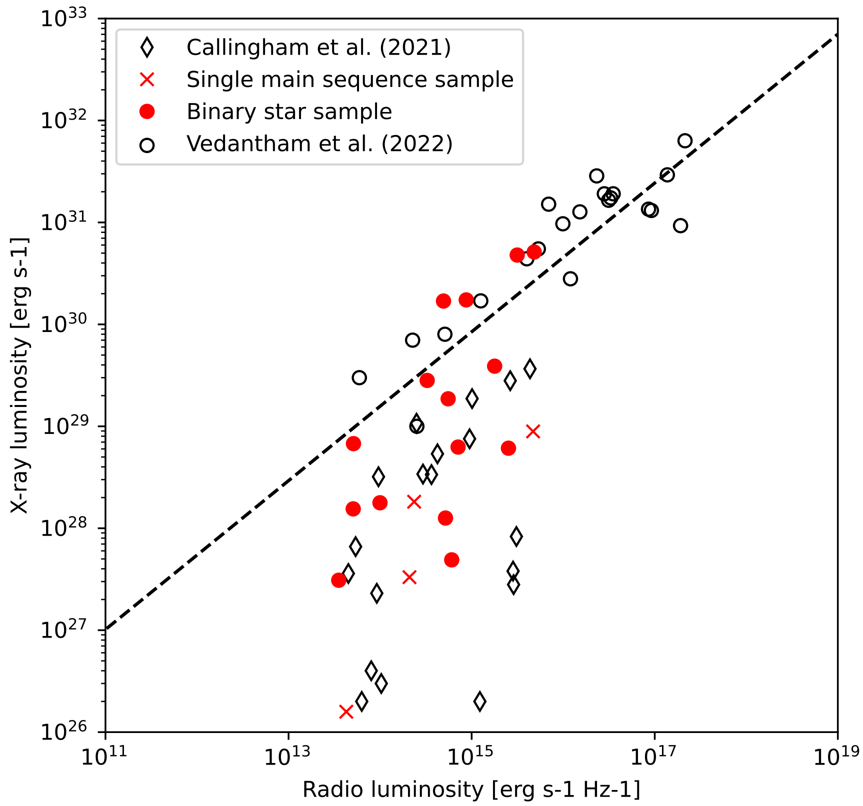

Figure 5.5: Plot of radio luminosity against x-ray luminosity of our samples of single main sequence stars and binaries from LoTSS in red. The sample of LOFAR-detected M dwarfs from Callingham et al. (2021) are shown as black diamonds, and the sample of LOFAR-detected RSCVnV variables from Vedantham et al. (2022) are shown as black circles. The Güdel-Benz relation is shown as a dashed black line, as given in Vedantham et al. (2022) to be $L_X = 9.48 \cdot 10^{18} L_{\nu,rad}^{0.73}$.

very similarly as a function of bolometric luminosity across all surveys. Another issue is the lack of reported estimates of rotation periods, X-ray- and bolometric luminosities, which would have increased the number of sources in our plots significantly, making finding a meaningful relation much more likely.

5.4 Obvious outliers

5.4.1 On the very bright G and F type stars in LoTSS

In Figure 4.2 we found two very bright non-M dwarf outliers, one of type G and one of type F, both having brightness temperatures on the order of 10^{14} K. The G type stars is BD+49 1932 with a spectral type G0, although it has no luminosity class in SIMBAD. The F type star is HD 125858, a star of type F5, also without a luminosity class in SIMBAD. This lack of luminosity classes is worrying, as the the stars may not be main sequence, but rather non-main sequence stars that have not been well observed, and therefore not yet determined to be non-main sequence. However, we show some of the important properties of the two stars in Table 5.2, which might indicate if the two stars are main sequence or not. Looking at the properties of BD+49 1932 we see that some of its properties are surprisingly similar to those of the Sun, mainly the mass, radius and effective temperature. However, no age is known, and its period is much lower than that of the Sun, meaning that BD+49 1932 is a relatively rapidly rotating star, its period of 5.425 days only being $\sim 22\%$ of the Sun's equatorial rotation period of 24.47 days. The fact that the star is rapidly rotating could explain some of the increased brightness temperatures. When looking up BD+49 1932 in SIMBAD it is found to have an infrared-excess, given by one of its object types of NIR, as designated by the 2 Micron All Sky Survey (2MASS) (Lonsdale 1998). Because of this the star could host a circumstellar disk, as these disks are known to emit infrared radiation (Melis et al. 2012).

HD 125858 is found to have mass, radius and temperature that closely match the expected values for a star of type F5V, although this does not mean that HD 125858 is confirmed to be main sequence. Contrary to BD+49 1932 we here have a reported Age of 2 Gyr, less than half of the Sun's age, which is still old enough to have reached the main sequence. Even though no period is reported for HD 125858, all the other properties match those of a main sequence star of type F5V, which strengthens our confidence that HD 125858 is in fact on the main sequence.

As an additional confidence check we look at the LoTSS cutouts of the two outliers, and these are shown in Figure 5.6. The left plot shows the cutout of BD+49 1932, where it is found that the source is both slightly off-centre and elongated. The red ellipse indicating the fitted Gaussian does not include all of the source's tail, but the fit does seem reasonable nonetheless. In the cutout of HD 125858 we see a very nice Gaussian shaped source almost exactly at the expected position of the star. The fitted Gaussian is here almost perfectly circular. The source in the cutout centred on the expected position of BD+49 1932 is slightly elongated, which hopefully is just because of an elongated beam in the region. However, it could also be contamination by an active galactic nuclei (AGN) or other radio source. To check this we look up the expected position of BD+49 1932 in the NASA/IPAC Extrgalactic Database[1]. We here find the relatively close radio source, NVSS J101404+484856. It is unknown if this radio source is in fact the same star or an AGN, although if it is an AGN it should not move in the sky over time. If that is the case the distance between the supposed AGN and our star is almost exactly 1', which should be sufficient to conclude that we do infact observe the star, as our cutout is only 30" wide.

The same sources in other surveys

To possibly explore how the fluxes of BD+49 1932 and HD 125858 change as functions of frequency we look for detections of the two sources in our remaining surveys. Detections

[1] http://ned.ipac.caltech.edu/

Name	SpType	Distance [pc]	Age [Myr]	Mass [$M_\odot$]	Radius [$R_\odot$]	Period [d]	T_{eff} [K]
BD+49 1932	G0	89.75	–	1.053	1.06	5.425	5854
HD 125858	F5	82.21	2000	1.471	1.46	–	6635.4

Table 5.2: Some of the properties of the outlier stars found in LoTSS.

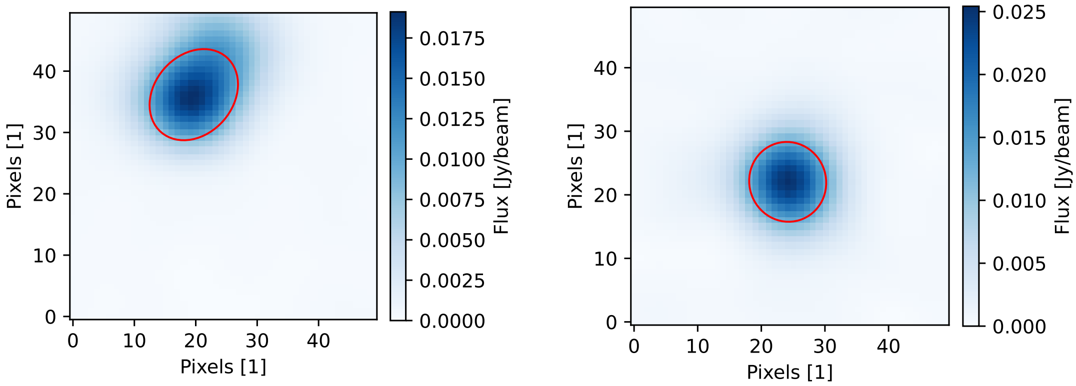

Figure 5.6: The left plot is a cutout from LoTSS-DR2 centred on the expected position of BD+49 1932. A clear detection is here found, although slightly off-centre and elongated. The right plot is a cutout from LoTSS-DR2 centred on the expected position of HD 125858. A very nice Gaussian and centred source is here detected. The red rings indicate the fitted Gaussian functions to the sources.

of BD+49 1932 are only found in LoTSS and TGSS, and the fluxes in TGSS mostly seem suspiciously high, which we explore further in Section 5.6. As here covered in more detail, Tiwari et al. (2019) explored the systematically high or low fluxes in TGSS by comparing the fluxes with those of GLEAM at 151 MHz, and thus produced a map showing the sky regions where TGSS produces systematically high or low fluxes. Checking the position of BD+49 1932 in this map would therefore tell us if the flux we measure in TGSS is artificially high (or low) due to TGSS' flux calibration. Sadly, BD+49 1932 is not found to lie within the map produced in Tiwari et al. (2019), as it does not lie within the field-of-view of GLEAM, as BD+49 1932 is a northern star. It is therefore not possible to claim that the flux we measure in TGSS is indeed correct. However, if it turns out to be correct, we have evidence of a consistently super-bright sun-like star, as very similar fluxes have been observed at two different epochs. BD+49 1932 could then be a very interesting target for future targeted observations with the GMRT or Karl G. Jansky Very Large Array (VLA). As previously mentioned, BD+49 1932 is also found to have an IR excess, meaning that it could perhaps have a circumstellar disk, which could be an interesting observational target with the Atacama Large Millimetre-Array (ALMA) if it is found to be resolvable. BD+49 1932 is found to be at a distance of 89.74 pc from Earth, meaning that if we were to be able to resolve a circumstellar disk of radius 10 AU around it we would need an angular resolution of:

$$\theta = \frac{10\text{ AU}}{89.75\text{ pc}}\ [\text{arcseconds}] \approx 0.11''. \tag{5.3}$$

ALMA can achieve angular resolutions of 20 ms at 240 GHz and 43 ms at 110 GHz at its most extended array configuration[2], meaning that it should be able to resolve a disk of radius 10 AU.

Detections of HD 125858 are found in LoTSS, VLA FIRST and VLASS, meaning that we have flux measurements of this star at 144 MHz, 1.4 GHz and 3 GHz. The measured fluxes of BD+49 1932 and HD 125858 as functions of frequency are shown in Figure 5.7, BD+49 1932 in the left plot and HD 125858 in the right. The fluxes

[2]Please refer to the following page for more details:
https://almascience.nrao.edu/about-alma/alma-basics

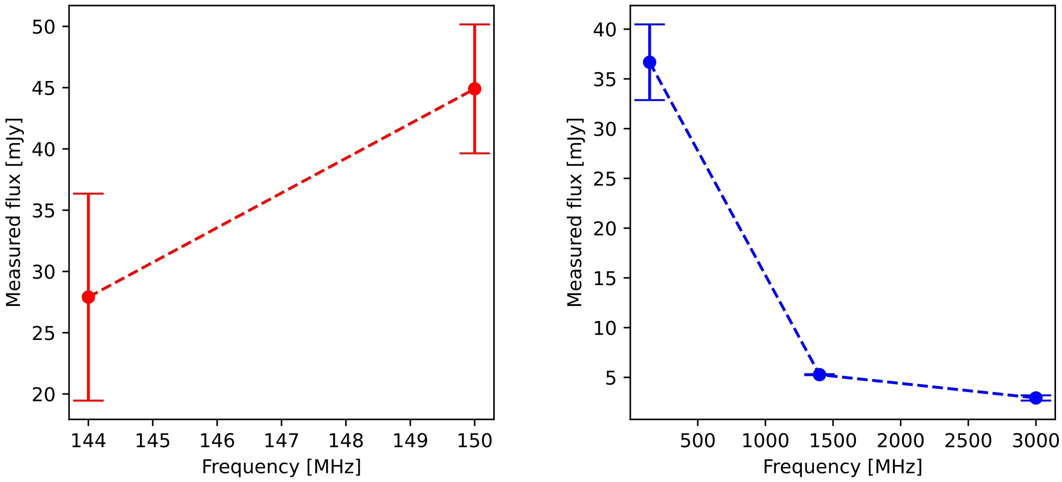

Figure 5.7: Measured flux as a function of frequency, with BD+49 1932 (G0) to the left, and HD 125858 (F5) to the right.

of BD+49 1932 in LoTSS and TGSS are surprisingly comparable, almost being within each others' error bars, which is as expected seeing as only 6 MHz separate the two surveys. However, in Section 5.6 we find that the fluxes we measure in TGSS are generally much higher than those we measure in LoTSS, almost being exactly two orders of magnitude higher. This difference is not observed for BD+49 1932 which is in itself surprising. The measured flux of HD 125858 is found to decrease drastically as a function of frequency, dropping from 36.67504 mJy at 144 MHz to 5.27345 mJy and 2.93350 mJy at 1.4 and 3 GHz respectively. Determining if this relatively large drop in flux between 144 MHz and 1.4 GHz is due to some super-flare phenomena at the time LOFAR was observing HD 125858, or indeed if this flux is consistent, is impossible with our limited sample. Further observations of the radio-bright F star HD 125858 at 144 MHz are needed to answer the question of its high flux. Only then could we for certain attribute the incredible brightness to a flare, or say that this F star has this consistent brightness at 144 MHz.

5.5 On the versatility of our method

Even though we set out with a goal of searching for stellar emission in sub-THz frequencies associated with single main sequence stars, bi-products of our method are similar catalogues of detected non-main sequence stars in each of the five surveys. These catalogues can be expanded upon and utilised in future studies, be it on the radio emission from white dwarfs or binaries.

Hajduk et al. (2022) performed a targeted search of known chemically peculiar stars with LOFAR, where they searched both Stokes V and Stokes I maps from the second data release of the LOFAR Two-metre Sky Survey (LoTSS). In their search for chemically peculiar stars they were able to detect two stars in Stokes I, namely the single star BP Boo (A0VpSiCr) and the binary star α^2 CVn (A0VpSiEu). Both of these stars we also detect using our method of cross-matching the positions of stars in Gaia DR3 with LoTSS-DR2 Stokes I maps. BP Boo is a part of our main sample of single main sequence stars, while α^2 CVn is in our sample of binary systems. The fact that we are

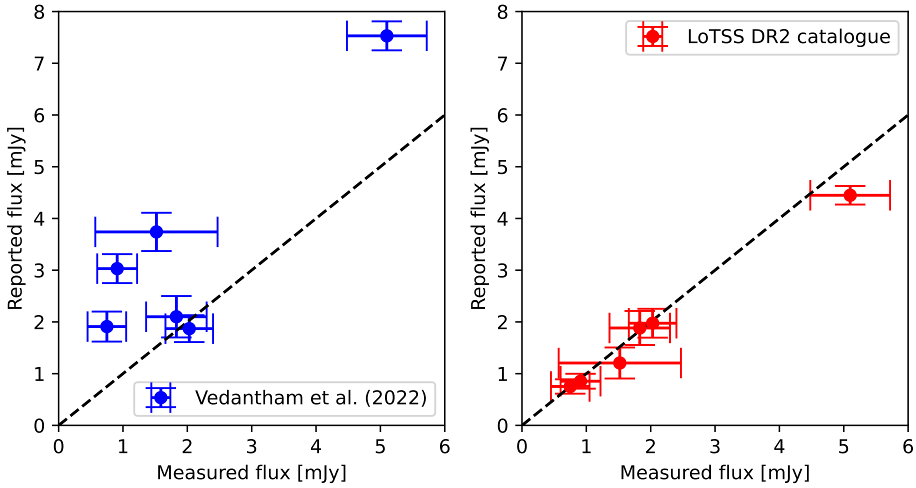

Figure 5.8: Left: A comparison between the reported fluxes in Vedantham et al. (2022) and those we measure for the six sources in their sample we also detect. The dashed black line is the line where the reported fluxes would equal the measured fluxes.
Right: A comparison between the measured fluxes of the same six sources and the their reported fluxes in the official LoTSS DR2 catalogue (Shimwell et al. 2022).

able to reproduce the same results using our method shows that our routine is versatile, and that it can be used in studies of non-main sequence stars as well. To better show the strengths of our non-main sequence catalogues of detected stars we perform a thorough comparison between our sample of RS Canum Venaticorum variables, to those reported in Vedantham et al. (2022).

5.5.1 RS Canum Venaticorum variables

Vedantham et al. (2022) present a sample of 21 radio-detected chromospherically active stars in LOFAR Two-metre Sky Survey (LoTSS), most of which are RS Canum Venaticorum (RS CVn) variables. As a sanity check we cross-check their reported sample with our own sample of RS CVn variables as part of our binary sample. However, this is not a one-to-one comparison as our samples are not built on the same premises. We have used the GAIA DR3 catalogue as our initial catalogue, but this catalogue is complete, as certain stars are not included. This is the case for four of the stars in the Vedantham et al. (2022) sample, which because of them not existing in GAIA DR3 we have no way of detecting. Furthermore, we initially chose to limit ourselves to sources within 100 pc of the Sun to make the tables of manageable size, which Vedantham et al. (2022) did not, their farthest reported star being over 300 pc from the Sun. There are no reasons why our scripts would not work up to this distance, but because of the limited time we were not able to extend the search for stellar emission up to a radius of > 300 pc. Actually, only six stars in their sample of 21 stars lie within 100 pc, all of which we detect and designate to be P1C1. Table 5.3 shows the comparison between the sample reported in Vedantham et al. (2022) and our binary sample, the first column showing the SIMBAD main ids, the second if the source is a part of our sample, the third if the source is part of the Gaia DR3 catalogue and the fourth and final column shows if the star is within 100 pc of the Sun. Rows are coloured green in the cases where we also detect the star and white if the star is undetectable using our method, either because it is not a part of Gaia DR3 or because it is not within 100 pc of the

Sun. As we detect every reported star within 100 pc the confidence in the quality of our sample is heightened.

Even if we are now confident in the stars within our sample, it is not a certainty that we measure the correct integrated fluxes at each of the sources. We therefore perform a last comparison between our sample and that of Vedantham et al. (2022), namely a comparison between their reported integrated fluxes and our measured integrated fluxes. This is done for the six sources they report that we also detect, and a table showing the reported integrated flux versus the value we measure is found in Table 5.4. It is here found that the fluxes reported in Vedantham et al. (2022) are generally higher than what we measure, which could be an immediate reason for concern. A plot showing the reported fluxes in Vedantham et al. (2022) versus our measured fluxes is shown in the left-most subplot of Figure 5.8, as already seen in Table 5.4 showing that the reported fluxes are generally much greater than those we measure. The dashed line here indicates where the measured fluxes would equal the reported ones. For an immediate attempt to some peace of mind we also compare our measured fluxes to those reported in the official LoTSS DR2 catalogue (Shimwell et al. 2022) to see if they also are greater than what we measure, which could be a sign of there being something wrong with the codes. The comparison between the fluxes reported in LoTSS DR2 and those we measure is found in the right-most subplot of Figure 5.8, here showing a much nicer correlation between the fluxes we measure and those reported in the table. The fluxes of each of the six stars are now found to lie within one error-bar of the line where the reported flux would equal the measured flux, making up for the loss of confidence in our scripts from the discrepancies between our measured flux and those of Vedantham et al. (2022).

MAIN ID (Vedantham et al. 2022)	In our sample?	In Gaia DR3?	Within 100 pc?
V* EV Dra	Yes	Yes	Yes
FG UMa	No	Yes	No
DM UMa	No	Yes	No
II Peg	Yes	Yes	Yes
OU And	No	Yes	No
WW Dra	No	Yes	No
BD+42 2437	No	Yes	No
YY Gem	Yes	Yes	Yes
BF Lyn	Yes	Yes	Yes
FG Cam	No	Yes	No
EZ Peg	No	Yes	No
FF UMa	No	Yes	No
BQ CVn	No	No	No
DQ CVn	No	No	No
44 Boo	No	No	Yes
BD+33 4462	No	Yes	No
Sig CrB	Yes	Yes	Yes
FI Cnc	No	Yes	No
FK Com	No	Yes	No
ksi UMa	No	No	Yes
BH CVn	Yes	Yes	Yes

Table 5.3: The comparison between our binary sample and the population of mostly RS CVn variables from Vedantham et al. (2022). Green rows indicate sources which Vedantham et al. (2022) report that we also detect and designate a P1C1 label. The remaining white rows are undetectable using our method, either because the source is not in Gaia DR3 or not within 100 pc of the Sun.

5.6 On the dissimilarity between our LoTSS and TGSS results

The LoTSS and TGSS surveys are, as covered in more detail in Section 3.1, two surveys at very similar frequencies. LoTSS has the mean frequency of 144 MHz, while TGSS has a frequency of 150 MHz. One would therefore expect the results from these surveys to be very similar to each other, both in trends and in values, but this has not been found to be the case. Although only 6 Mhz separates the frequencies of the two surveys, a seemingly consistent difference of two orders of magnitude is found in our plots, be it plots of brightness temperature or radio luminosity fractions. To investigate this deviation we firstly check our measured fluxes against those found in the official catalogues for LoTSS and TGSS in Vizier. Note that these catalogues do not specify which source is being observed, only its position, so in the LoTSS' case we compare

MAIN ID	Reported flux [mJy]	Measured flux [mJy]
V* EV Dra	3.03 ± 0.28	0.91 ± 0.31
II Peg	3.74 ± 0.37	1.52 ± 0.95
YY Gem	1.87 ± 0.26	2.03 ± 0.37
BF Lyn	1.91 ± 0.29	0.75 ± 0.30
Sig CrB	7.53 ± 0.28	5.10 ± 0.62
BH CVn	2.10 ± 0.40	1.83 ± 0.47

Table 5.4: A comparison between the reported fluxes in Vedantham et al. (2022) and the fluxes we measure for the six stars in their sample that we detect.

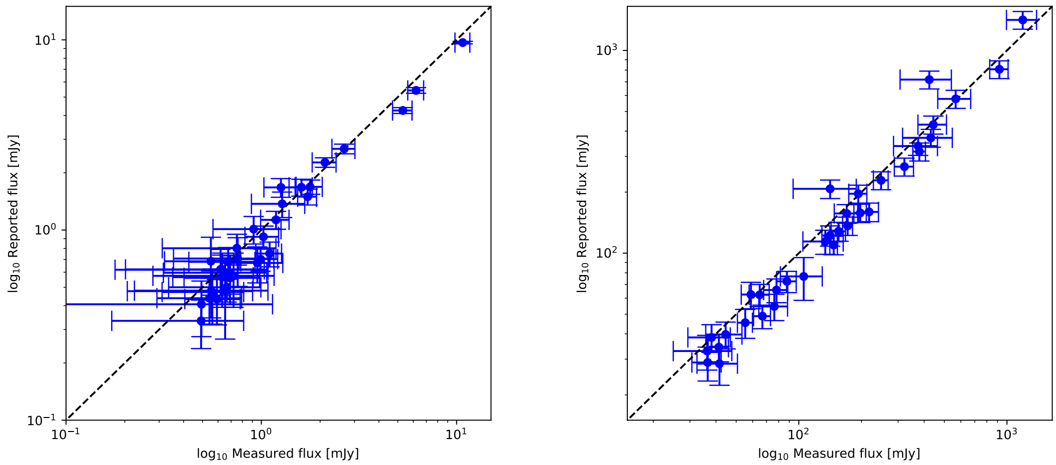

Figure 5.9: The left figure shows a plot of the measured fluxes of all detected M dwarfs in LoTSS versus the reported fluxes of the closest source within 30" in the official LoTSS catalogue in Vizier (Shimwell et al. 2022). The right figure shows a plot of the measured fluxes of all detected M dwarfs in TGSS versus the reported fluxes of the closest source within 60" in the official TGSS catalogue in Vizier (Intema et al. 2017). We here allow a slightly larger radius to account for the much larger beam of TGSS compared to LoTSS. The dashed line indicates the line where the reported fluxes equal the measured fluxes.

the flux with the closest source within 30", while in TGSS' we compare with the flux of the closest source within 60" to account for TGSS' much larger beam compared to LoTSS. Figure 5.9 shows comparisons between the measured and reported fluxes of all detected M dwarfs in LoTSS and TGSS. Note that these M dwarfs are not necessarily the same stars, but should still show similar fluxes in the two surveys. It is here found that our measured fluxes lie close to the reported fluxes in most cases, almost within the error bars for every detected source. We can therefore be more confident that our measured fluxes are actually correct, and that the large difference in flux between the two surveys is not due to an error in flux measurement on our end.
Interestingly Tiwari et al. (2019) have studied the effects of flux calibration systematics on the galaxy power spectrum using data from TGSS, and concluded that some of the survey regions showed signs of both high and low flux at their moderate and large scales. As we have used TGSS data for very small scales compared to Tiwari et al. (2019), we have not found indications of these low flux regions, however all our fluxes seem to be inexplicably high.

Chapter 6

Conclusions

Astronomical observations at radio and millimetre wavelengths enable the detection of emission stemming from highly energetic phenomena in stellar chromospheres and coronae. Sub-THz surveys are usually insufficient for quiescent flux detection due to too low sensitivities, but they are able to detect flaring fluxes from nearby stars, as these fluxes have been found to be 2-6 orders of magnitude higher than the quiescent flux. These surveys are therefore suitable for blind and unbiased searches for flaring stars, as opposed to the more common targeted studies which are often biased towards X-ray and UV bright and known flare stars. The blind search for stellar emission also prevents the common bias towards M dwarfs in targeted studies, as we should also be able to detect flaring emission from larger and hotter stars.

We have constructed five comprehensive catalogues of detected main sequence stars in the five surveys; LoTSS, TGSS, RACS, VLA FIRST and VLASS. These surveys span the frequency range from 144 MHz to 3 GHz, a range which should contain emission from several different emission mechanisms in stellar coronae. We found evidence of stellar emission from every type of main sequence star from M dwarfs to A type stars, emphasising the need to also study the activity of hotter, larger and more massive stars, and the need to remove the common bias towards M dwarfs. These catalogues of detected stars in the considered surveys can be useful tools in future studies of stellar radio activity, but also for future observation time proposals.

The detected stars were also used in a comprehensive analysis, where we studied how the measured brightness temperatures and ratios of radio- to bolometric luminosity depend on stellar parameters and activity indicators. It was here found that the cooler and smaller stars are generally brighter in the entire 144 MHz to 3 GHz regime, having both higher brightness temperatures and greater radio- to bolometric luminosity fractions. We found that the slopes of first-order fits in the log-log regime on each of these relations are very similar and within the 3σ uncertainties of each other across the different frequencies, suggesting that the proportionality between the fitted values is consistent between the considered surveys. In contrast, the offset constants of the fitted relations were found to change as a function of frequency. The decrease of the offsets as a function of frequency in the range 144 MHz to 3 GHz implies that the numerical values of T_B or L_R/L_{bol} should decrease towards higher frequencies in the same range. We also presented some obvious outlying stars, mainly stars that had brightness temperatures much higher than expected in comparison to similar stars. We here focused on the stars BD+39 1932 and HD 125858, with spectral types G0 and F5, respectively. Especially interesting is here BD+49 1932 as it is found to be a rapidly rotating Sun-like star, which has a reported near-infrared emission in SIMBAD. This star could therefore be host to a protoplanetary disk, which could be observed and studied further in the future.

These two stars were not the only anomalous stars in the sample, even though they were focused on in our discussion. Our vast catalogues of detected stars in the considered surveys contain many interesting targets for future research. One could further study the radio emission from the A type stars we detect to better constrain the temperature at which A types no longer form chromospheres and coronae, or apply for longer exposure observations of slowly rotating and quiescent M dwarfs to look for signs of periodic radio emission associated with an orbiting and interacting satellite. The possibilities are many, and with the advent of new and more powerful radio interferometers such as the Square Kilometer Array (SKA) the future is bright for the field of radio astronomy.

Bibliography

Airy, G. B. 1835, Transactions of the Cambridge Philosophical Society, 5, 283

Aschwanden, M. J. 2005, Physics of the Solar Corona. An Introduction with Problems and Solutions (2nd edition)

Aschwanden, M. J., Tarbell, T. D., Nightingale, R. W., et al. 2000, , 535, 1047, doi: 10.1086/308867

Bashi, D., et al. 2020, , 643, A106, doi: 10.1051/0004-6361/202038881

Callingham, J. R., Vedantham, H. K., Shimwell, T. W., et al. 2021, Nature Astronomy, 5, 1233, doi: 10.1038/s41550-021-01483-0

Cannon, A. J., & Pickering, E. C. 1912, Annals of Harvard College Observatory, 56, 65

Childs, A. C., Martin, R. G., & Livio, M. 2022, The Astrophysical Journal Letters, 937, L41, doi: 10.3847/2041-8213/ac9052

Dulk, G. A., & Marsh, K. A. 1982, , 259, 350, doi: 10.1086/160171

Dwivedi, R. S. 2017, An Introduction to Remote Sensing (Berlin, Heidelberg: Springer Berlin Heidelberg), 1–47, doi: 10.1007/978-3-662-53740-4_1

Gaia Collaboration. 2022, VizieR Online Data Catalog, I/355

Gaia Collaboration, Prusti, T., de Bruijne, J. H. J., et al. 2016, , 595, A1, doi: 10.1051/0004-6361/201629272

Ginzburg, V. L., & Zhelezniakov, V. V. 1958, , 2, 653

Goldstein, J., Gallagher, D., Sandel, B., et al. 2022, in Understanding the Space Environment through Global Measurements, ed. Y. Colado-Vega, D. Gallagher, H. Frey, & S. Wing (Elsevier), 231–286, doi: https://doi.org/10.1016/B978-0-12-820630-0.00010-6

Guedel, M., & Benz, A. O. 1993, , 405, L63, doi: 10.1086/186766

Hajduk, M., Leto, P., Vedantham, H., et al. 2022, , 665, A152, doi: 10.1051/0004-6361/202243784

Hale, C. L., McConnell, D., Thomson, A. J. M., et al. 2021, , 38, e058, doi: 10.1017/pasa.2021.47

Intema, H. T., Jagannathan, P., Mooley, K. P., & Frail, D. A. 2017, , 598, A78, doi: 10.1051/0004-6361/201628536

Lacy, M., Baum, S. A., Chandler, C. J., et al. 2020, , 132, 035001, doi: 10.1088/1538-3873/ab63eb

Lammer, H., Lichtenegger, H. I. M., Kulikov, Y. N., et al. 2007, Astrobiology, 7, 185, doi: 10.1089/ast.2006.0128

Léna, P., Rouan, D., Lebrun, F., Mignard, F., & Pelat, D. 2012, Telescopes and Images (Berlin, Heidelberg: Springer Berlin Heidelberg), 175–207, doi: 10.1007/978-3-642-21815-6_5

Lonsdale, C. 1998, in Astrophysics and Algorithms, 4

Mason, E., Barceló-Llull, B., Sánchez-Román, A., et al. 2023, in Oceanography of the Mediterranean Sea, ed. K. Schroeder & J. Chiggiato (Elsevier), 263–287, doi: https://doi.org/10.1016/B978-0-12-823692-5.00003-0

McConnell, D., Hale, C. L., Lenc, E., et al. 2020, , 37, e048, doi: 10.1017/pasa.2020.41

Melis, C., Zuckerman, B., Rhee, J. H., et al. 2012, , 487, 74, doi: 10.1038/nature11210

Melrose, D. B. 2009, in Universal Heliophysical Processes, ed. N. Gopalswamy & D. F. Webb, Vol. 257, 305–315, doi: 10.1017/S1743921309029470

Melrose, D. B., & Dulk, G. A. 1982, , 259, 844, doi: 10.1086/160219

Mohan, A., Wedemeyer, S., Hauschildt, P. H., Pandit, S., & Saberi, M. 2022, , 664, L9, doi: 10.1051/0004-6361/202244385

Mohan, A., Wedemeyer, S., Pandit, S., Saberi, M., & Hauschildt, P. H. 2021, , 655, A113, doi: 10.1051/0004-6361/202142095

Nan, R., Li, D., Jin, C., et al. 2011, International Journal of Modern Physics D, 20, 989, doi: 10.1142/S0218271811019335

Noraz, Q., Breton, S. N., Brun, A. S., et al. 2022, , 667, A50, doi: 10.1051/0004-6361/202243890

Pagano, I. 2013, Stellar Activity, ed. T. D. Oswalt & M. A. Barstow (Dordrecht: Springer Netherlands), 485–557, doi: 10.1007/978-94-007-5615-1_10

Parker, E. N. 1977, , 15, 45, doi: 10.1146/annurev.aa.15.090177.000401

PECSELI, H. L. 2021, Waves and oscillations in plasmas (ROUTLEDGE)

Pedersen, M. G., Antoci, V., Korhonen, H., et al. 2016, Monthly Notices of the Royal Astronomical Society, 466, 3060, doi: 10.1093/mnras/stw3226

Perryman, M. A. C., Lindegren, L., Kovalevsky, J., et al. 1997, , 323, L49

Ptolemy, & Toomer, G. J. 1984, Ptolemy's Almagest / translated and annotated by G.J. Toomer (Duckworth London), ix, 693 p. :

Rucinski, S. M., & Vandenberg, D. A. 1986, , 98, 669, doi: 10.1086/131812

Rybicki, G. B., & Lightman, A. P. 1985, FUNDAMENTALS OF RADIATIVE TRANSFER (John Wiley Sons, Ltd), 1–50, doi: https://doi.org/10.1002/9783527618170.ch1

—. 1986, Radiative Processes in Astrophysics

Shimwell, T. W., Röttgering, H. J. A., Best, P. N., et al. 2017, , 598, A104, doi: 10.1051/0004-6361/201629313

Shimwell, T. W., Hardcastle, M. J., Tasse, C., et al. 2022, , 659, A1, doi: 10.1051/0004-6361/202142484

Simon, T., Ayres, T. R., Redfield, S., & Linsky, J. L. 2002, , 579, 800, doi: 10.1086/342941

Thompson, A. R., Clark, B. G., Wade, C. M., & Napier, P. J. 1980, , 44, 151, doi: 10.1086/190688

Tiwari, P., Ghosh, S., & Jain, P. 2019, , 887, 175, doi: 10.3847/1538-4357/ab54c8

Trigilio, C., Biswas, A., Leto, P., et al. 2023, arXiv e-prints, arXiv:2305.00809, doi: 10.48550/arXiv.2305.00809

Urone, P., & Hinrichs, R. 2012, College Physics (Houston, Texas: OpenStax). https://openstax.org/books/college-physics/pages/1-introduction-to-science-and-the-realm-of-physics-physical-quantities-and-units

Vaiana, G. S., Cassinelli, J. P., Fabbiano, G., et al. 1981, , 245, 163, doi: 10.1086/158797

van Haarlem, M. P., Wise, M. W., Gunst, A. W., et al. 2013, , 556, A2, doi: 10.1051/0004-6361/201220873

Vedantham, H. K., Callingham, J. R., Shimwell, T. W., et al. 2022, , 926, L30, doi: 10.3847/2041-8213/ac5115

—. 2020, Nature Astronomy, 4, 577, doi: 10.1038/s41550-020-1011-9

Vernazza, J. E., Avrett, E. H., & Loeser, R. 1981, , 45, 635, doi: 10.1086/190731

Vidotto, A. A., et al. 2013, , 557, A67, doi: 10.1051/0004-6361/201321504

Wayth, R. B., Lenc, E., Bell, M. E., et al. 2015, , 32, e025, doi: 10.1017/pasa.2015.26

Wedemeyer-Böhm, S., Lagg, A., & Nordlund, Å. 2009, , 144, 317, doi: 10.1007/s11214-008-9447-8

White, S. 2007, Asian J. Phys, 16, 189

Wild, J. P., Smerd, S. F., & Weiss, A. A. 1963, , 1, 291, doi: 10.1146/annurev.aa.01.090163.001451

Wilson, T. L., Rohlfs, K., & Hüttemeister, S. 2009, Radio Astronomical Fundamentals (Berlin, Heidelberg: Springer Berlin Heidelberg), 1–18, doi: 10.1007/978-3-540-85122-6_1

Zendejas, J., Segura, A., & Raga, A. C. 2010, , 210, 539, doi: 10.1016/j.icarus.2010.07.013

Švanda, M., & Karlický, M. 2016, The Astrophysical Journal, 831, 9, doi: 10.3847/0004-637X/831/1/9